

BUNDESANSTALT FÜR GEOWISSENSCHAFTEN UND ROHSTOFFE (BGR),
HANNOVER
FEDERAL INSTITUTE FOR GEOSCIENCES AND NATURAL RESOURCES

FAHRTBERICHT
Sonne-Fahrt SO-201 Leg 1a

CRUISE REPORT
Sonne Cruise SO-201 Leg 1a

KALMAR
**KURILE-KAMCHATKA AND ALEUTIAN MARGINAL SEA-
ISLAND ARC SYSTEMS: GEODYNAMIC AND CLIMATE
INTERACTION**

Yokohama, 16 May 2009 – Yokohama, 10 June 2009



-
1. Sachbearbeiter: Chr. Gaedicke (Wiss. Fahrtleiter)
J. Adam, U. Barckhausen, H.-O. Bargeloh, T. Behrens, Ü. Demir,
D. Franke, R. Freitag, F. Goldmann, I. Heyde, G. Kallaus, S. Ladage,
R. Lutz, N. Tsukanov, T. Pletsch, U. Schrader, A. Sievers,
E. Sukhoveev, H. Thöle, M. Zeibig, T. Ziehlke
2. Auftraggeber: Bundesministerium für Bildung und Forschung (BMBF)
Förderkennzeichen **03G0201B**
3. Datum: Juni 2009
4. Archiv-Nr.

TABLE OF CONTENTS

1	SUMMARY	7
2	INTRODUCTION	9
2.1	Scientific aims of the KALMAR project	9
2.2	Objectives of cruise SO201-Leg 1a	10
2.3	Origin of the Emperor Seamount Chain	11
3	PARTICIPATING INSTITUTIONS	13
4	CRUISE NARRATIVE	14
4.1	Profile list and map	16
5	PARTICIPANTS	19
5.1	German Participants	19
5.2	Guest Scientists	19
5.3	Crew of RV Sonne	19
6	GEOPHYSICAL EQUIPMENT/OPERATIONS	21
6.1	Shipboard equipment	21
6.1.1	Navigation and positioning	21
6.1.2	Simrad EM120 multibeam bathymetry system	21
6.1.3	PARASOUND sediment echosounder	24
6.2	Computer facilities/network and data acquisition system	30
6.3	Multi-channel seismics	32
6.3.1	Airgun arrays	33
6.3.2	Seismic data acquisition system	34
6.3.3	Streamer Depth	40
6.3.4	Onboard processing of seismic reflection data	43
6.3.5	Multichannel seismic interpretation	52
6.4	Magnetic data acquisition and processing	54
6.4.1	Marine Magnetics SeaSpy™ Gradiometer	55
6.4.2	Magson™ Fluxgate Magnetometer	56
6.4.3	Fluxgate Calibration	57
6.4.4	Magnetic data processing	57
6.5	Gravity	60
6.5.1	The sea gravimeter system KSS31M	60
6.5.2	Gravity ties to land stations	62
6.5.3	Gravity data processing	65
7	PRELIMINARY SCIENTIFIC RESULTS	67

7.1	Bathymetry and morphotectonics of the Emperor Seamount Chain.....	67
7.2	Multi-channel seismic interpretation	73
7.3	PARASOUND recordings.....	80
7.4	Magnetic and seafloor spreading anomalies	83
7.4.1	Transit profiles.....	83
7.4.2	Magnetic anomalies of the Emperor Seamount Chain area.....	85
7.5	Gravity data: description and preliminary interpretation	90
7.5.1	Gravity database	90
7.5.2	Comparison with gravity anomalies derived from satellite altimetry	91
7.5.3	Gravity anomaly maps	95
7.5.4	Interpretation by forward modeling.....	98
8	ACKNOWLEDGEMENTS	102
9	REFERENCES.....	103
10	APPENDIX	105
10.1	PARASOUND settings during cruise SO201-1a	105

ANNEX

A.I Composite displays of MCS, gravity, magnetic and bathymetric data

LIST OF FIGURES

Fig. 2.3.1:	Age progression of the Hawaii-Emperor seamount chain. Note the sharp bend in the chain around 43 Ma.	11
Fig. 4.1.1:	Map of geophysical profiles produced during cruise SO201.....	18
Fig. 6.1.1:	Annual mean sound velocity profiles from the Levitus database along the transit from Japan to the Emperor Seamount Chain and measured SVP of station SO201-CTD01.....	23
Fig. 6.1.2:	PARASOUND processing, step 2, data import.	27
Fig. 6.1.3:	PARASOUND processing, step 3, UTM conversion.....	27
Fig. 6.1.4:	PARASOUND processing, step 4, definition of start and end traces of profile	28
Fig. 6.1.5:	PARASOUND processing, step 5, extraction of selected traces.....	28
Fig. 6.1.6:	PARASOUND processing, step 7, make equidistant traces.	29
Fig. 6.1.7:	PARASOUND processing, step 8, data export.	29
Fig. 6.2.1:	Setup for data collection and storage installed during SO201.	31
Fig. 6.3.1:	Configuration of BGR's airgun system during cruise BGR08 SO197.....	34
Fig. 6.3.2:	Streamer configuration used.....	36

Fig. 6.3.3: Signal flow diagram for BGR's reflection seismic data acquisition system.	39
Fig. 6.3.4: Principal configuration of the DigiCOURSE 3 System	40
Fig. 6.3.5: Frequency spectra with different streamer depths: 6 metres.	41
Fig. 6.3.6: Frequency spectra with different streamer depths: 8 metres.	41
Fig. 6.3.7: Frequency spectra with different streamer depths: 12 metres.	42
Fig. 6.3.8: Frequency spectra with different streamer depths: 15 metres.	42
Fig. 6.3.9: Onboard processing system.	43
Fig. 6.3.10: Example shot gather after bandpass filtering. Note the low frequency noise burst in the centre of the streamer and at the end of the streamer.	46
Fig. 6.3.11: Example shot gather after noise burst editing (threshold = 2).....	47
Fig. 6.3.12: Example shot gather after SWNR (1500 m/s).....	47
Fig. 6.3.13: Example shot gather after dip scan stack. This process is very time-consuming and thus was rarely applied.....	48
Fig. 6.3.14: Example shot gather after prestack processing (full spectrum preserved).	48
Fig. 6.3.15: Example of post-stack Kirchhoff-migrated section	50
Fig. 6.3.16: Example of post-stack Stolt-migrated section.....	50
Fig. 6.3.17: Example of a post-stack phase shift migrated section	51
Fig. 6.3.18: Summary of the acquisition geometry.....	52
Fig. 6.3.19: Computer equipment for seismic data interpretation.	53
Fig. 6.3.20: Loading definition for MCS data into IESX.....	53
Fig. 6.3.21: Loading definition for Parasound data into IESX.	54
Fig. 6.4.1: Schematic sketch of the setup used during cruise SO 201, Leg 1a, consisting of a towed gradiometer system (front and rear Overhauser sensor) and one fluxgate towfish in-between.	55
Fig. 6.4.2: Components inside the fluxgate magnetometer towfish.	56
Fig. 6.4.3: Positions of magnetometer winch, outrigger port, GPS antenna, and Gravimeter on R/V Sonne.....	60
Fig. 6.5.1: Principle sketch of the gravity sensor GSS30 of the gravimeter system KSS31M	61
Fig. 6.5.2: Location of the mooring site of R/V SONNE at Yamashita pier no. 3 of Yokohama harbour (from the Japan Coast Guard chart JP66).....	64
Fig. 6.5.3: Comparison of BEARB and KSS31M free-air gravity anomalies along a part of profile BGR09-M02 measured during medium to rough sea state conditions and a ship velocity of 12-13 knots.	66
Fig. 7.1.1: 3D-view of the NW Pacific with the Emperor Seamount Chain, the Kurile, and the Kamchatka trench. The survey tracks are overlain onto the SRTM30plus V5.0 data set.	68

Fig. 7.1.2: Depth profile along line BGR09-103	68
Fig. 7.1.3: 3D-view of the eastern slope of a seamount along line BGR09-103 (view to west). Slump debris is observed at the base of the seamount, as well as gullies and several slump scars at the slope.	69
Fig. 7.1.4: Top: 3D-view of the western slope of a seamount (view to east). Bottom: Cross-section along line BGR09-107. Note the scarp along the upper part of the slope and the V-shaped trough parallel to the slope. Note also the steep offset of ~ 200 m at the foot of the slope.	70
Fig. 7.1.5: 3D-view (top) and cross-section (bottom) of Jimmu Seamount (view to the south)	71
Fig. 7.1.6: 3D-view of a caldera mapped along profile BGR09-103.....	72
Fig. 7.1.7: 3D-view of the West Emperor Fault and morphotectonic setting.	73
Fig. 7.1.8: Detailed 3D-view 3D-(top) and cross section (bottom) of the West Emperor Fault along line BGR09-107. Note the relay ramp	73
Fig. 7.2.1: Part of multi-channel seismic profile BGR09-101 imaging the typical oceanic crust west of the Emperor Seamount Chain. (colours: red = Moho reflection, light green = intraoceanic crust reflection, dark green = top-oceanic crust, light green = 'base of sediments', cyan = normal fault).....	74
Fig. 7.2.2: Part of multi-channel seismic profile BGR09-103 crossing the Jimmu Seamount. For colours refer to Fig. 7.2.1	76
Fig. 7.2.3: Part of multi-channel seismic profile BGR09-110 crossing the Wayne seamount. For colours refer to Fig. 7.2.1.....	76
Fig. 7.2.4: Part of multi-channel seismic profile BGR09-101 crossing a fracture zone east of the Emperor Seamount Chain. For colours refer to Fig. 7.2.1	77
Fig. 7.2.5: Part of multi-channel seismic profile BGR09-103 crossing fracture zone east of the Emperor Seamount Chain. For colours refer to Fig. 7.2.1	78
Fig. 7.2.6: Part of multi-channel seismic profile BGR09-105 crossing fracture zone east of the Emperor Seamount Chain. For colours refer to Fig. 7.2.1	78
Fig. 7.2.7: Part of multi-channel seismic profile BGR09-101 crossing the flexural basin west of the Jimmu Seamount. For colours refer to Fig. 7.2.1.....	80
Fig. 7.3.1: Part of Parasound profile BGR09-107 showing perfectly stratified sediments, which are typical for the depositional environment of the abyssal plains.81	
Fig. 7.3.2: Part of Parasound profile BGR09-105 showing two lenses of acoustically transparent masses on the western flank of the Emperor Seamounts.	81
Fig. 7.3.3: Part of Parasound profile BGR09-107 showing acoustically transparent layers within the depressions.....	82
Fig. 7.3.4: Part of Parasound profile BGR09-103 showing an example of an individual package of stratified sediments on top of a seamount.....	83
Fig. 7.4.1: Magnetic anomalies (red lines) of the northwestern Pacific after Cande et al. (1989). Numbers indicate magnetic chrons. Wiggles show magnetic anomalies along shiptracks of cruise SO-201.....	84

- Fig. 7.4.2: Magnetic anomalies along ship tracks of cruise SO-201 over the Emperor seamounts shown as wiggles. Red lines are magnetic lineations after Cande et al. (1989). Numbers indicate magnetic chrons. Background shows the color coded bathymetry derived from satellite data..... 86
- Fig. 7.4.3: Magnetic anomalies along ship tracks of cruise SO-201 over the Emperor seamounts shown as wiggles. Green lines are magnetic lineations after Cande et al. (1989). Numbers indicate magnetic chrons. Background shows magnetic anomalies of the 2-minute Earth Magnetic Anomaly Grid (EMAG2) (Maus et al., 2008); red: positive anomalies, blue: negative anomalies..... 88
- Fig. 7.4.4: Profiles BGR09-102 and BGR09-106 (red) correlated with a synthetic profile and age scale. The synthetic profile was calculated using the magnetic reversal time scale of Cande and Kent, 1995. 89
- Fig. 7.4.5: Magnetic anomalies along ship tracks of cruise SO-201 over the Emperor seamounts shown as wiggles. Green lines are magnetic lineations after Cande et al. (1989). Numbers indicate magnetic chrons. Red dotted lines show seafloor spreading lineations according to Fig. 7.4.4, red dashed lines tentatively indicate possible correlations of magnetic anomalies in the oceanic crust underlying the seamount chain. These cannot be age dated as seafloor spreading anomalies. 90
- Fig. 7.5.1: Map of the free-air gravity anomalies in the survey area of cruise SO-201. The map is drawn up to a distance of 25 kilometres from the tracks. The map is based on a 1 x 1 (arc-)minutes grid and it is underlain by the bathymetry of Andersen et al. (2008). 91
- Fig. 7.5.2: Differences of the shipboard free-air gravity data and the gravity datasets derived from satellite altimetry (A: Sandwell and Smith (1997), version 16.1; B: Andersen et al. (2008), DNSC08)..... 93
- Fig. 7.5.3: Histogram of differences between shipboard KSS31M free-air gravity anomalies and the corresponding gravity datasets derived from satellite altimetry. . 94
- Fig. 7.5.4: Comparison of the ship-based KSS31M and satellite (DBSC08 and SDW16.1) free-air gravity anomalies along profile BGR09-112..... 95
- Fig. 7.5.5: Free-air gravity anomaly map. The underlying grid of gravity was compiled by merging SO-201 gravity observations and DNSC08 gravity data derived from satellite altimetry. Fault zones of Cande et al. (1989) are marked black, the ship track blue. The map is based on a 1 x 1 (arc-)minutes grid and is underlain by the bathymetry from Andersen et al. (2008) 97
- Fig. 7.5.6: Map of Bouguer gravity anomalies. The reduction density was 1.64 g/cm³. The map is underlain by the bathymetry from Smith and Sandwell (1997), version 9.1. 98
- Fig. 7.5.7: 2D density model explaining the free-air gravity anomalies along BGR09-101. Dotted lines: observed anomalies; Continuous line: calculated anomalies. Density values are given in kg/m³, susceptibilities in SI units. 100
- Fig. 7.5.8: 2D density model explaining the free-air gravity anomalies along BGR09-107. Dotted lines: observed anomalies; Continuous line: calculated anomalies. Density values are given in kg/m³..... 101
- Fig. 10.1.1: Magnetic and gravimetric data, top. MSC profile BGR09-101, CDP spacing 12.5 m, time section, middle. Interpretation of seismic data, bottom..... 110

Fig. 10.1.2: Magnetic and gravimetric data, top. MSC profile BGR09-102, CDP spacing 12.5 m, time section, middle. Interpretation of seismic data, bottom.....	111
Fig. 10.1.3: Magnetic and gravimetric data, top. MSC profile BGR09-103, CDP spacing 12.5 m, time section, middle. Interpretation of seismic data, bottom.....	112
Fig. 10.1.4: Magnetic and gravimetric data, top. MSC profile BGR09-104, CDP spacing 12.5 m, time section, middle. Interpretation of seismic data, bottom.....	113
Fig. 10.1.5: Magnetic and gravimetric data, top. MSC profile BGR09-105, CDP spacing 12.5 m, time section, middle. Interpretation of seismic data, bottom.....	114
Fig. 10.1.6: Magnetic and gravimetric data, top. MSC profile BGR09-106, CDP spacing 12.5 m, time section, middle. Interpretation of seismic data, bottom.....	115
Fig. 10.1.7: Magnetic and gravimetric data, top. MSC profile BGR09-107, CDP spacing 12.5 m, time section, middle. Interpretation of seismic data, bottom.....	116
Fig. 10.1.8: Magnetic and gravimetric data, top. MSC profile BGR09-108, CDP spacing 12.5 m, time section, middle. Interpretation of seismic data, bottom.....	117
Fig. 10.1.9: Magnetic and gravimetric data, top. MSC profile BGR09-109, CDP spacing 12.5 m, time section, middle. Interpretation of seismic data, bottom.....	118
Fig. 10.1.10: Magnetic and gravimetric data, top. MSC profile BGR09-110 + 110a, CDP spacing 12.5 m, time section, middle. Interpretation of seismic data, bottom.	119
Fig. 10.1.11: Magnetic and gravimetric data, top. MSC profile BGR09-111, CDP spacing 12.5 m, time section, middle. Interpretation of seismic data, bottom.....	120
Fig. 10.1.12: Magnetic and gravimetric data, top. MSC profile BGR09-112, CDP spacing 12.5 m, time section, middle. Interpretation of seismic data, bottom.....	121
Fig. 10.1.13: Transit Yokohama – Emperor Seamount Chain Map Set 1	122
Fig. 10.1.14: Transit Yokohama – Emperor Seamount Chain Map Set 2	123
Fig. 10.1.15: Transit Yokohama – Emperor Seamount Chain Map Set 3	124
Fig. 10.1.16: Transit Emperor Seamount Chain – Yokohama Map Set 1	125
Fig. 10.1.17: Transit Emperor Seamount Chain – Yokohama Map Set 2	126
Fig. 10.1.18: Transit Emperor Seamount Chain – Yokohama Map Set 3	127

LIST OF TABLES

Tab. 4.1.1: List of geophysical profiles	18
Tab. 6.3.1:	44
Tab. 6.3.2: Onboard processing overview.	51
Tab. 6.4.1: Magnetometer sensor and cable configurations applied during all cruise profiles and calibration loops.	60
Tab. 6.5.1: Observation report of the gravity tie measurements in Yokohama. Fehler! Textmarke nicht definiert.	

SUMMARY

Research cruise SO-201 Leg 1a was carried out on board R/V Sonne in the framework of the KALMAR project which is funded by the German Ministry of Education and Research. The cruise started on May 16th and ended on June 9th 2009 in Yokohama, Japan. During the cruise, marine-geophysical data were acquired including multi-channel seismics (MCS), magnetics (M) and gravimetry (G). In addition, the shipboard systems swath echosounder (SIMRAD) and sediment echosounder (PARASOUND) were used.

During the cruise, 2714 km of multi-channel seismic data, magnetic data, gravimetry data and SIMRAD and PARASOUND data were collected. An additional 3180 km were acquired without multi-channel seismic during transits. The scientific focus lies on the northernmost part of the Emperor Seamount Chain where 11 profiles were acquired. The structure and architecture of the seamounts as well as of the surrounding sediments was studied. Fracture zones of the oceanic crust which are trending in an acute angle to the seamount chain were imaged and analysed at high resolution. OPD Site 882 was crossed to correlate the sedimentary record. A 431 km long profile parallel to the Kamchatka trench was acquired to analyse the sedimentary cover of the oceanic crust and to map two fracture zones which most probably influence the deformation of the Kamchatka fore-arc.

On the basis of the data from this Leg, 36 sample sites were suggested where crystalline rocks of the oceanic crust or the submarine volcanoes reaches the surface. Sampling of these sites during SO-201 Leg 1b with a dredge might be promising.

ZUSAMMENFASSUNG

Im Rahmen des BMBF-Verbundvorhabens KALMAR wurde vom 16. Mai bis 09. Juni 2009 die Forschungsfahrt SO-201 Leg 1a mit FS Sonne durchgeführt. Die Fahrt startete und endete in Yokohama, Japan. Während der Fahrt wurden marin-geophysikalische Messungen mit Mehrkanal-Reflexionsseismik (MCS), Magnetik (M) und Gravimetrie (G) durchgeführt. Parallel dazu wurden die bordeigenen Systeme Simrad (Fächerecholot) sowie Parasound (Sediment-Echolot) eingesetzt.

Während der Expedition wurden insgesamt 2714 km mit Mehrkanalseismik, Magnetik, Gravimetrie, Sedimentecholot und Fächerecholot gemessen. Zusätzlich wurden weitere 3180 km ohne MCS aufgezeichnet. Mit 11 Profilen lag der Schwerpunkt der Untersuchungen auf dem nördlichen Teilstück der Emperor-Seamount-Kette. Hier wurde die Struktur und Architektur der Seamounts und der sie umlagernden Sedimente erfasst. Auf der ozeanischen Kruste wurden Bruchzonen vermessen, die im spitzen Winkel zur Kette der erloschen Vulkanen streichen. Zur Korrelation des Sedimente wurde das ODP-Site 882 auf dem Wayne-Seamount überfahren. Ein 431 km langes Profil parallel zur Kamtschatka-Tiefseerinne diente der Bestimmung der sedimentären Auflage der ozeanischen Kruste und der Rekonstruktion zweier Bruchzonen, die wahrscheinlich die Deformation im Fore-Arc von Kamtschatka beeinflussen.

Auf Grundlage der seismischen Profile und der aufgezeichneten Bathymetrie wurden 36 Beprobungspunkte definiert, an denen kristalline Gesteine der ozeanischen Kruste und der submarinen Vulkane am Meeresboden ausstreichen und deren Morphologie den Einsatz einer Dredge während SO-201 Leg 1b zulässt.

INTRODUCTION

C. Gaedicke, R. Freitag, N. Tsukanov

1.1 Scientific aims of the KALMAR project

The **KALMAR** (**K**uril-Kamchatka and **A**leutian **M**ARginal Sea-Island Arc Systems: Geodynamic and Climate Interaction) project is based on the excellent results obtained during previous German-Russian research in the Okhotsk Sea and on the Kamchatka peninsula (e.g. KOMEX). In contrast to its predecessors, the regional focus of the KALMAR project is on the adjacent Kuril-Kamchatka-Aleutian arc, the NW Pacific ocean and on the Bering Sea. This complex geosystem is a unique research area for the modern marine geosciences, where the interaction of asthenosphere, lithosphere, hydrosphere and atmosphere can be studied in detail.

The continental margin of Kamchatka and the Kuril island arc forms a 2.500 km long subduction system and hosts some of the most active volcanoes of the world. Catastrophic eruptions will not only seriously harm adjacent areas, but will also have a significant impact on global environment and climate. The system is mainly controlled by the change from ocean-island arc subduction to ocean-continent subduction, by geodynamic processes in the Aleutian-Kamchatka triple junction and by the subduction of the Emperor Seamount Chain. The results of the former KOMEX project shows that the extreme volcanic activity on Kamchatka might be related to the flux of enriched mantle material from the Pacific region. The underlying processes are not yet understood and are a matter of recent scientific discussion. The formation of the Aleutian Island Arc has an enormous impact on the exchange of water masses between the Bering Sea and the North Pacific and on climate. The continental slope of eastern Kamchatka and the lake sediments on Kamchatka bear a currently unexplored archive of climate development that may reveal the land-ocean coupling within the northern hemisphere. The dynamics of the western boundary current system exerts a major control on climate history, both on long and on very short time scales. The change of circulation in time and space influenced the fluxes of energy and materials between continent and ocean as well as the hydrography of the adjacent waters.

The primary target of the joint German-Russian research project KALMAR is to understand the processes that govern and modulate this complex climatic system and to analyse the ongoing geodynamic, oceanographic and physical processes of mass distribution, mass cycles, water mass circulation, climate and natural hazards. The Kuril-Kamchatka-Aleutian arc and the surrounding marine environment are envisioned as a complex geosystem and therefore help to understand the system Earth. This target can be reached only in a multi-disciplinary attempt, which is essential for the success of the KALMAR project. The idea is to bring together German and Russian scientists with different specialisation and different expertise and excellent junior scientists from both countries to benefit from the intensive exchange of ideas, experience and data. The German-Russian working groups consist of geologists, volcanologists, geophysicists, paleo-oceanographers, oceanographers and geochemists. Their research focuses on two targets: on the geodynamic-volcanic-magmatic history and on the oceanographic-climate evolution of the Kuril-Kamchatka-Aleutian System. They will concentrate on the following topics:

- Tectonic and geodynamic evolution of the active Kamchatka margin and balancing of the subduction zone
- Volcanic, magmatic and geodynamic evolution of the Kamchatka-Aleutian triple-junction in space and time
- Reconstruction of Pleistocene and Holocene climatic history and oceanography in the subarctic northwest Pacific and its adjacent seas on time scales from years to millennia
- Pleistocene and Holocene continent-ocean coupling in the subarctic Pacific and its relation to global environmental processes

1.2 Objectives of cruise SO201-Leg 1a

According to the aims of the project our investigations were initially planned to be carried out in Russian waters. Due to the rejection of our application by Russian authorities we were forced to work in international waters only. To pursue the idea of understanding the geodynamic system of the north-western Pacific we shifted our study area to the north-western part of the Emperor Seamount chain. This string of extinct submarine volcanoes originate from the Hawaiian Archipelago. The (palaeo-) motion of the Pacific Plate displaces the volcanoes on top of the oceanic crust from their place of origin towards the active margin of Kamchatka. The chain of inactive volcanoes trends west-northwestward from Hawaii and bends to a north-northwest direction from about 30°N until the Kamchatka Peninsula which forms the western edge of the Eurasian Plate. There, the Emperor Seamount Chain collides with continental crust and subducts under the Kronotsky Peninsula in eastern Kamchatka. Subduction of the seamounts likely exerts a major control on the location, periodicity and on the enormous volumes of volcanism on Kamchatka. With our investigation we want to determine the architecture, mass and evolution of the seamounts as well as the mechanical properties of the incoming Pacific Plate. The geophysical investigations are used to determine the locations for subsequent sampling of outcropping magmatic rocks to investigate their geochemical signatures (SO201-Leg 1b, conducted by IFM-Geomar, chief scientist: Dr. R. Werner). One profile parallel to the outer part of the Kamchatka trench provides data which help to quantify the sedimentary input into the subduction zone.

A second major goal of SO201-Leg 1a is the investigation of fracture zones and shear zones cutting through the oceanic crust. These shear zones most probably have a significant impact on the deformation and segmentation of the Kamchatka fore arc (Freitag et al. 2001 Gaedicke et al. 2000). Tectonic lineaments onshore (in the area of Petropavlovsk-Kamchatsky) and in the accretionary wedge display the same trend as the oceanic fracture zones. Multichannel seismic profiles across fracture zones provide sufficient information to determine the geodynamic history along these fracture zones.

Drift deposits are documents of deepwater circulation processes. Our mapping of contourites with geophysical methods (MCS, sediment echosounder and swath bathymetry) will support paleo-oceanographic models of the north-western Pacific.

1.3 Origin of the Emperor Seamount Chain

Hauke Thöle, Ralf Freitag

The Hawaiian-Emperor Seamount Chain stretches for more than 6000 km across the north-west Pacific ocean from the vicinity of the Kamchatka peninsula to the volcanic islands of Hawaii. A kink in the middle of the seamount chain separates the ENE-WSW trending Hawaiian chain from the NNW-SSE striking Emperor Seamounts. It is an alignment of more than 100 submarine volcanoes. The estimated total volume of the magmatic rocks is about 106 km^3 (BARGAR & JACKSON 1974). Meiji Guyot, the northernmost seamount, is located directly off the Kronotsky peninsula in eastern-central Kamtchatka. Dating of the Meiji Guyot revealed an age greater than 85 Ma (WORSLEY 1973; TARDUNO ET AL. 2003, DUNCAN & KELLER, 2004). Following the chain to the south, Detroit and Jimmu Seamounts are among the prominent subsea elevations in our study area.

The Hawaiian-Emperor Seamount Chain shows a clear age progression. The ages of individual seamounts increases from very young or recent volcanism on the Islands Hawaii and Loihi to about 43 Ma in the area of Diakakuji seamount, where the sharp bend in the chain is located. Following the Emperor Seamounts to the North, ages increase up to 81 Ma at Detroit seamount (ODP Site 883, Keller et al. 1995). Most authors accept, that the progression in ages is the result of the motion of the Pacific plate over a stationary Hawaii hotspot. As all seamounts are located on the Pacific plate, the plate motion must have changed at 43 Ma if the hotspot was stationary. The reason for the sharp bend and for the change in plate motion in the Hawaii Emperor seamount chain at 43 Ma is still matter of scientific discussion. Candidates for the bend might be subduction initiation, ridge subduction or the collision of India with Asia, which occurred at the same time.

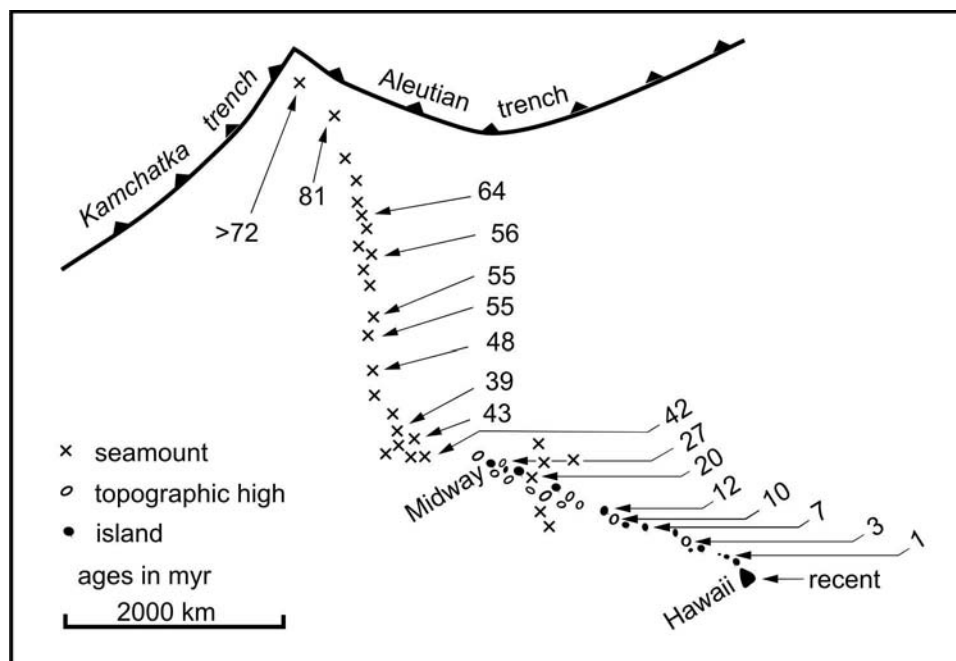


Fig. 1.3.1: Age progression of the Hawaii-Emperor seamount chain. Note the sharp bend in the chain around 43 Ma.

PARTICIPATING INSTITUTIONS

- BGR:** Bundesanstalt für Geowissenschaften und Rohstoffe
Dienstgebäude Alfred-Bentz-Haus
Stilleweg 2
30655 Hannover
Germany
Tel.: +49 – 0511 – 643 – 0 / Fax: +49 – 0511 – 643 – 2304
Internet: www.bgr.de
- Univ. Jena:** Friedrich Schiller-University Jena
Institut für Geowissenschaften – Strukturgeologie
Burgweg 11
Germany
07749 Jena
Tel.: +49 – 3641 – 948626
E-Mail: ralf.freitag@uni-jena.de
Internet: www.igw.uni-jena.de
- IO RAS:** P.P. Shirshov Institute of Oceanology
Russian Academy of Science
Nachimovsky Avenue 36
117851 Moscow
Russian Federation
Tel.: +7 – 495 – 1246563
E-mail: nvts_ov@rambler.ru, paleogeo@ocean.ru
Internet: www.ras.ru
- POI FEB RAS:** V.I. Illichev's Pacific Oceanological Institute,
Far Eastern Branch of the Russian Academy of Science
Baltiyskaya Street 43
690041 Vladivostok
Russian Federation
Tel.: +7 – 4232 – 312150 / Fax: +7 – 4232 – 312573
E-mail: sukhoveev@poi.dvo.ru
Internet: www.poi.dvo.ru

CRUISE NARRATIVE

C. Gaedicke

Date	Time	All times are local or ship's time = UTC + 9h For position of profiles see Table Tab. 1.4.1
May, 15 th , 2009	12:00	Chr. Gaedicke and N. Tsukanov are visiting RV SONNE at Yokohama Yamashita Pier, Yokohama, discuss container handling and logistics.
May, 16 th 2009	08:15	Scientific crew onboard; the scientific equipment containers including the streamer winch are moved onboard. Start of installation of BGR's scientific equipment by the whole BGR crew.
May, 17 th 2009	08:30	Embarkation of scientific crew, Installation of scientific equipment continued. The onshore connection measurements for the gravity measurements were carried out by I. Heyde at Aburatsubo gravity station (see for details Chapter: 1.12)
	15:30	Security introduction to scientific crew by 2 nd Officer J. Göbel.
May, 18 th 2009	09:00	Pilot on board and RV SONNE leaves Yokohama for cruise SO201 Leg1a. Mobilisation of equipment continued during the transit into the investigation area.
May, 19 th 2009	11:20	Start profile BGR09-M01, speed over Ground: 12 kn with Magnetometer, Gravity, Hydro-acoustic systems (SIMRAD, Parasound).
	13:47	Start profile BGR09-M02. Magnetometer, Gravity, Hydro-acoustic systems.
May, 20 th 2009	09:00	Onboard test of air gun system under high pressure at reduced speed (6kn). Profile BGR09-M02 continued
	12:00	around 12:00 wind speed up to 18.5 m/s, decreasing wind speed to 8 m/s
May, 23 rd , 2009	11:59	End profile BGR09-M02; magnetic sensor onboard
	13:05	Sound velocity profile at 45°01,81 N, 165°46 ,71 E, depth 2000 m
	14:00	Streamer into water, air guns system into water, magnetometer into water
	17:38	Start profile BGR09-101 with MCS, Magnetometer, Gravity, Hydro-acoustic systems, all seismic lines: speed over ground 5.4 kn
May, 26 th , 2009	02:13	End profile BGR09-101 Turn over port side
	02:30	Start profile BGR09-102 with MCS, Magnetometer, Gravity, Hydro-acoustic systems
	08:17	End profile BGR09-102
	08:20	Start profile BGR09-102a with MCS, Magnetometer, Gravity, Hydro-acoustic systems

	14:00	Maintenance of air gun system (starboard array)
	15:34	End profile BGR09-102a Turn over port side
	15:46	Start profile BGR09-103 with MCS, Magnetometer, Gravity, Hydro-acoustic systems
May 27 th , 2009	22:59	End profile BGR09-103 Turn over starboard
	23:30	Start profile BGR09-104 with MCS, Magnetometer, Gravity, Hydro-acoustic systems
May 28 th , 2009	05:03	End profile BGR09-104 Turn over starboard
	05:31	Start profile BGR09-105 with MCS, Magnetometer, Gravity, Hydro-acoustic systems
	15:30	Maintenance of air gun array (starboard)
May 29 th , 2009	16:45	End profile BGR09-105 Turn over port side
	17:20	Start profile BGR09-106 with MCS, Magnetometer, Gravity, Hydro-acoustic systems
	08:29	End profile BGR09-106 Turn over port side
May 30 th , 2009	08:45	Start profile BGR09-107 with MCS, Magnetometer, Gravity, Hydro-acoustic systems
May 31 st , 2009	12:14	End profile BGR09-107 Turn over starboard
	12:41	Start profile BGR09-108 with MCS, Magnetometer, Gravity, Hydro-acoustic systems
	17:40	End profile BGR09-108 Turn over starboard
	18:10	Start profile BGR09-109 with MCS, Magnetometer, Gravity, Hydro-acoustic systems
June 1 st , 2009	09:19	End profile BGR09-109 Turn over port side
	09:55	Start profile BGR09-110 with MCS, Magnetometer, Gravity, Hydro-acoustic systems
	09:55	Start profile BGR09-110 with MCS, Magnetometer, Gravity, Hydro-acoustic systems
	17:36	End profile BGR09-110
	17:43	Start profile BGR09-110a with MCS, Magnetometer, Gravity, Hydro-acoustic systems
	17:36	End profile BGR09-110

		Turn over port side
	15:00	Maintenance of air gun array (starboard)
	19:30	Start profile BGR09-111 with MCS, Magnetometer, Gravity, Hydro-acoustic systems
June 2 nd , 2009	10:29	End profile BGR09-111 Turn over port side
	10:50	Start profile BGR09-112 with MCS, Magnetometer, Gravity, Hydro-acoustic systems
June 4 th , 2009	05:59	End profile BGR09-112
	06:20	Air gun array port side on deck
	06:30	Magnetometer on deck
	06:50	Air gun array starboard on deck
	11:15	Streamer on deck, weights changed for survey in Red Sea
	11:35	Magnetometer in water
		Magnetometer calibration circle (1km radius, 8 kn)
		Start profile BGR09-M03 (Magnetometer, Gravity, Hydro-acoustic systems)

1.4 Profile list and map

line number	SP	date	time	latitude	longitude	course	methods	Profile km
BGR09-M01		19.05.09	02:20:20	35°21.325 N	145°06. 881 E		M,G,B	
		19.05.09	04:46:40	35°37.808 N	145°24.931 E	42°		40.89 km
BGR09-M02		19.05.09	04:47:00	35°37.847 N	145°24. 986 E		M,G,B	
		23.05.09	02:59:00	45°01.130 N	165°45.608 E	52°		2005.72 km
BGR09-101	1	23.05.09	08:38:09	45°07.084 N	166°05 .155 E		S,M,G,B	
	11316	25.05.09	17:13:07	47°07.118 N	172°51.045 E	64°		566.15 km
BGR09-102	1	25.05.09	17:30:27	47°08.464 N	172°50 .060 E		S,M,G,B	
	955	25.05.09	22:16:44	47°27.539 N	172°24.265 E	318°		47.92 km
BGR09-102A	1	25.05.09	22:20:52	47°27.790 N	172°2 3.935 E		S,M,G,B	
	1648	26.05.09	06:34:59	48°00.350 N	171°39.256 E	318°		82.04 km
BGR09-103	1	26.05.09	06:46:55	48°00.431 N	171°37 .757 E		S,M,G,B	

	6243	27.05.09	13:59:48	47°51.033 N	167°27.060 E	268°		311.49 km
BGR09-104	1	27.05.09	14:30:00	47°52.510 N	167°23 .898 E		S,M,G,B	
	1111	27.05.09	20:03:03	48°15.592 N	166°54.642 E	320°		56.01 km
BGR09-105	1	27.05.09	20:31:07	48°17.032 N	166°57 .421 E		S,M,G,B	
	7050	29.05.09	07:45:52	48°55.971 N	171°38.074 E	76°		351.03 km
BGR09-106	1	29.05.09	08:20:14	48°58.216 N	171°37 .574 E		S,M,G,B	
	3033	29.05.09	23:29:42	49°44.006 N	169°54.059 E	305°		150.92 km
BGR09-107	1	29.05.09	23:45:00	49°44.078 N	169°52 .004 E		S,M,G,B	
	5500	31.05.09	03:14:56	49°07.985 N	166°09.912 E	257°		275.63 km
BGR09-108	1	31.05.09	03:41:02	49°09.198 N	166°07 .082 E		S,M,G,B	
	1000	31.05.09	08:40:41	49°31.213 N	165°44.931 E	325°		49.98 km
BGR09-109	1	31.05.09	09:10:06	49°33.121 N	165°43 .931 E		S,M,G,B	
	3030	01.06.09	00:19:01	50°07.724 N	167°39.717 E	64°		151.30 km
BGR09-110	1	01.06.09	00:55:00	50°10.801 N	167°40 .654 E		S,M,G,B	
	1524	01.06.09	08:32:00	50°49.973 N	167°21.799 E	343°		75.86 km
BGR09-110A	1	01.06.09	08:43:13	50°50.890 N	167°2 1.322 E		S,M,G,B	
	300	01.06.09	10:12:53	50°58.684 N	167°17.393 E	342°		15.14 km
BGR09-111	1	01.06.09	10:30:00	50°59.423 N	167°15 .309 E		S,M,G,B	
	2999	02.06.09	01:29:24	51°16.031 N	165°09.750 E	283°		149.11 km
BGR09-112	1	02.06.09	01:50:00	51°15.198 N	165°07 .482 E		S,M,G,B	
	8633	03.06.09	20:59:54	48°29.673 N	160°52.358 E	226°		431.87 km
BGR09-M03		04.06.09	03:52:00	48°15.688 N	160°29. 159 E		M,G,B	
		06.06.09	07:10:00	40°49.694 N	150°39.084 E	227°		1133.28 km

Tab. 1.4.1: List of geophysical profiles

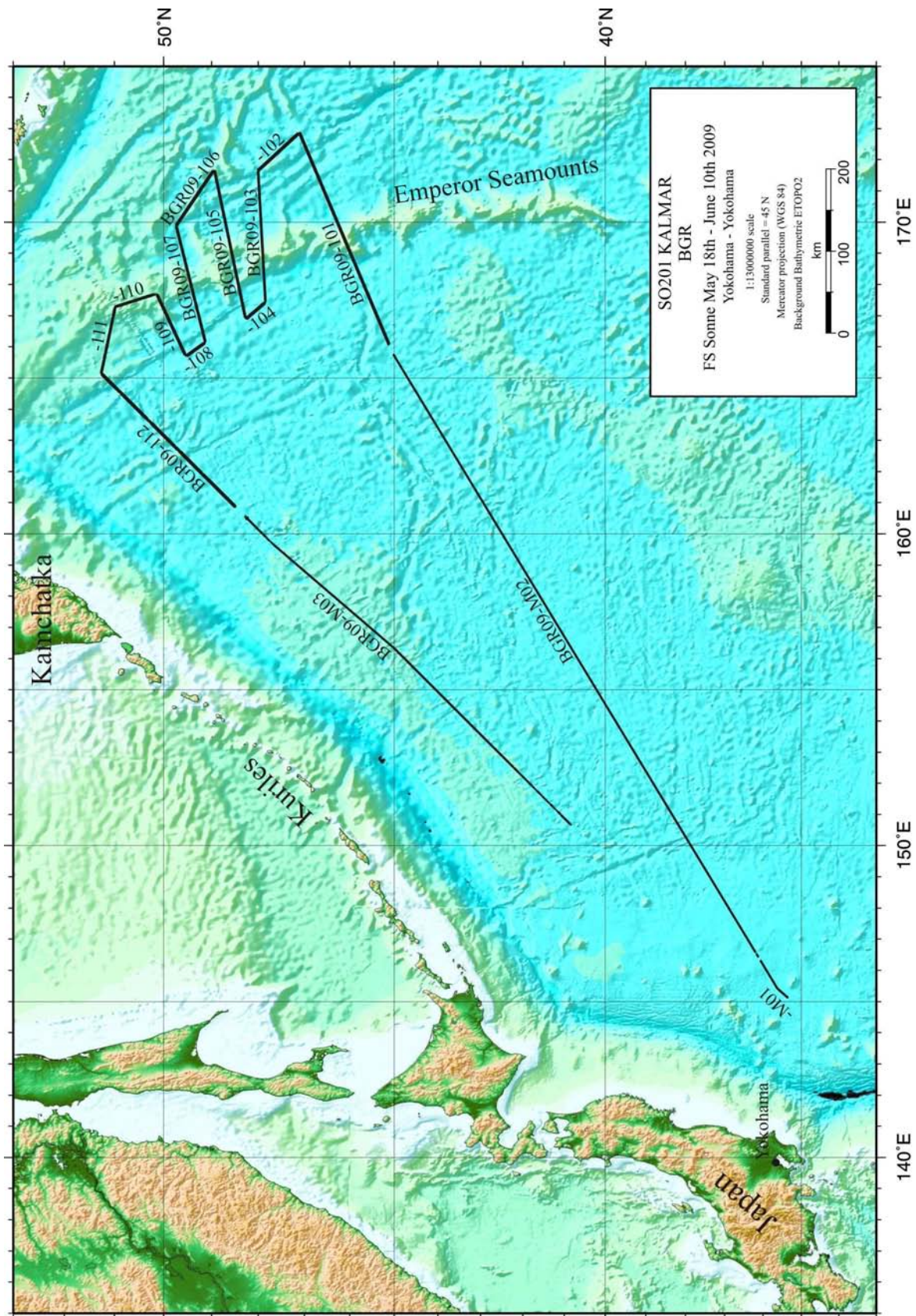


Fig. 1.4.1: Map of geophysical profiles produced during cruise SO201.

PARTICIPANTS

1.5 German Participants

Adam, Jürgen	BGR
Barckhausen, Dr. Udo	BGR
Bargeloh, Hans-Otto	BGR
Behrens, Thomas	BGR
Demir, Ümit	BGR
Franke, Dr. Dieter	BGR
Freitag, Dr. Ralf	Univ. Jena
Gaedicke, Dr. Christoph	BGR, Chief Scientist
Goldmann, Felix	BGR
Heyde, Dr. Ingo	BGR
Kallaus, Günter	BGR
Ladage, Stefan	BGR
Lutz, Dr. Rüdiger	BGR
Pletsch, Dr. Thomas	BGR
Schrader, Uwe	BGR
Sievers, Joachim	BGR
Thöle, Hauke	BGR
Zeibig, Michael	BGR
Ziehlke, Thorben	BGR

1.6 Guest Scientists

Sukhoveev, Dr. Evgeny	POI, FEB RAS
Tsukanov, Dr. Nikolay	IO RAS

1.7 Crew of RV Sonne

Mallon, Lutz	Master
Aden, Nils	Chief Mate
Schmitz, Olaf	2 nd Mate
Göbel, Jens	2 nd Mate
Walther, Anke	Physician
Guzmán-Navarrete, Werner	Chief Engineer

Thomsen, Sascha	2 nd Engineer
Hermesmeyer, Dieter	2 nd Engineer
Leppin, Jörg	Chief Electronic Engineer
Zebrowski, Dariusz	Electrician
Ehmer, Andreas	System Manager
Rosemeyer, Rainer	Fitter
Krawczak, Richard	Motorman
Zeitz, Holger	Motorman
Wieden, Wilhelm	Chief Cook
Ganagaraj, Antony	Cook
Grübe, Gerlinde	1 st Steward
Steep, Maik	2 nd Steward
Schrapel, Andreas	Bosun
Dolief, Joachim	A.B.
Bierstedt, Torsten	A.B.
Dehne, Dirk	A.B.
Kraft, Jürgen	A.B.
Stängl, Günther	A.B.
Eibel, Markus	A.B.
Eidam, Oliver	Apprentice
Globke, Valerie	Apprentice
Peplow, Michael	Apprentice

GEOPHYSICAL EQUIPMENT/OPERATIONS

1.8 Shipboard equipment

1.8.1 Navigation and positioning

H.-O. Bargeloh

Differential positioning (DGPS) with a Trimble 4000 DS receiver was used during cruise SO201 to provide the highest possible positioning accuracy for the reflection seismic profiling. Since May 2000 the GPS signals are available without the intentional degradation called 'selected availability' and since then positioning is possible with an accuracy in the order of 5 meters with DGPS as opposed to 20 - 50 meters with standard GPS. GPS signals were received from May 23 until June 8 throughout cruise SO201 without notable interruptions and in good quality.

A Fugro MultiFix system was used for DGPS which received the signals of four reference stations in Asia and in the USA via Inmarsat POR and via Spotbeam:

Reference Stations for Spotbeam (APSat):	Reference Stations for Inmarsat:
Asahikawa (Japan)	Anchorage /USA)
Okinawa (Japan)	Asahikawa (Japan)
Seoul (Süd Korea)	Okinawa (Japan)
	Seoul (Süd Korea)

The reference signals are provided by a Fugro-operated station in Perth (Australia). Since the costs for the DGPS service are ~200 € per day, it was used only on those days when reflection seismic profiling was carried out.

1.8.2 Simrad EM120 multibeam bathymetry system

S. Ladage

Features of the SIMRAD EM120

Seafloor bathymetric mapping has been conducted continuously during the cruise using the SIMRAD EM120 multibeam echo sounder. The system features and design are documented in the SIMRAD EM120 manual. A general description of system operation has been given in previous cruise reports (SO186, SO189 and SO197) and is repeated in the following.

The SIMRAD EM120 system is a multibeam swath sonar designed for all ocean depth ranges. The angular coverage sector of the echo system may reach 150° in shallow water or a swath width up to 25 km in depths greater than 5000 m. 191 beams as narrow as 2° are generated for each ping. The angular coverage, beam pointing angles and ping rate adapt to varying depth ranges. The ping rate depends merely on the overall round trip travel- and processing time. In shallow waters the ping rate may reach 3 Hz, whereas in 5000 m water depth a ping is generated about every 12 sec. The beam spacing has been set to equidistant beam footprint, thus allowing for uniform sampling of the seafloor across the track.

The seafloor is detected using amplitude and phase information for each beam sounding. Phase detection allows for high accuracy bottom determination even with high incidence angles of the soundings on the seafloor. Depth and position calculation is then performed per beam taking account of the beam angles and refraction in the water column using the corresponding sound velocity profile, the vessel's attitude and movement (MRU) and the vessel's position via the FS SONNE system-position sensor. Additionally, backscatter and amplitude data of the seafloor are recorded. All data and system operating parameters are stored on disc.

The transmit and receive transducer arrays of the EM 120 are mounted amidships in the keel of the vessel in the form of a Mills cross. The transmit transducer array contains 48 modules with 18 elements arranged in rows of 6. A transmitter unit, each with a unique amplitude and phase, drives each element individually. This allows for each transmitter unit to be individually steered according to the vessel's roll, pitch and yaw. The sectors are frequency-coded (11.25 to 12.60 kHz), and are transmitted sequentially at each ping. The soundings are placed on a best-fit line perpendicular to the survey line, thus maintaining a uniform sampling rate of the seafloor with 100% across-track coverage. Pulse length and range sampling rate are variable with depth. The receive transducer contains 16 modules with 8 hydrophone arrays each. A preamplifier unit individually amplifies the sounding echoes. Each hydrophone array can thus be given unique amplitude and phase weighting to allow forming of the required receive beams (SIMRAD EM120 Operator Manual).

Operation of the EM120 is monitored and controlled by a workstation on which all depth and position calculations are performed. Several online displays allow real-time quality control and access to the system sensors. Data are stored on hard disc on the workstation and are regularly copied to remote workstations. Data storage is organized in survey directories by the operating software. In each survey a new file is generated every hour. In general a new survey is created every day. Watch-keepers were responsible for monitoring and maintaining an error-free operation during the cruise.

Sound velocities

Water depths are calculated from beam travel times using a sound velocity model of the water column. Accurate depth calculations in a given survey area require the knowledge of the sound velocity profile of the water column for that specific region at the time of measurement. Sound velocities, especially of the upper water masses, are subject to considerable annual and local variation, for instance due to currents.

During SO201 Leg1 there has been only one possibility to measure a sound velocity, prior to deployment of the reflection seismic gear. The position chosen was in open and deep waters of the abyssal plain west of the Emperor Seamount Chain. A SeaBird CTD probe maintained and operated by FS SONNE was used for this station. The water column was sampled to a depth of 2000 m. Sound velocities for greater depths are calculated by the operator workstation according to the (UNESCO) Inter. Eq. of the State of Seawater (del Grosso formula). This sound velocity profile has been used for data acquisition with the SIMRAD EM120 system.

However, since hydroacoustic data was acquired after leaving the 200 nm sector off Japan during transit a large part of NW Pacific has been crossed. For these areas the measured sound velocity profile of CTD01 is not representative. In Fig. 1.8.1

annual mean sound velocity profiles of the NW-Pacific from the Levitus database, coming with the MB-system software that is used to edit the multibeam data (see below), are compared to the CTD01 data. A systematic decrease of near-surface and mid-water sound velocities can be observed from south to north. Sound velocities applied to the transit bathymetric data were therefore derived from the Levitus database. It is recommended that further CTD stations which provide the necessary sound velocity profiles in this area of highly variable water mass sound velocities be conducted during the upcoming legs.

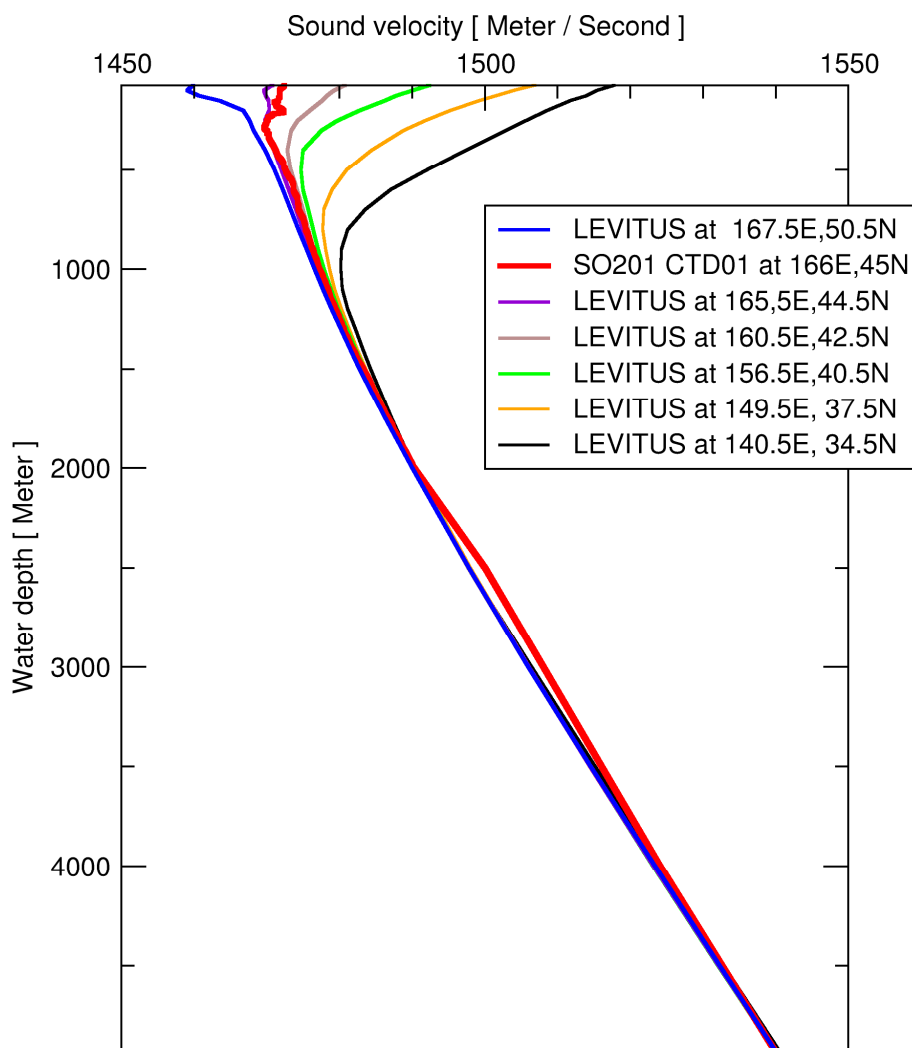


Fig. 1.8.1: Annual mean sound velocity profiles from the Levitus database along the transit from Japan to the Emperor Seamount Chain and measured SVP of station SO201-CTD01.

Operational notes

The SIMRAD EM120 operated throughout the cruise without interruption and with good data quality. A ship speed of 12 kn combined with a rougher sea state led to some tracks with considerable noise during transit. However, the reduced ship speed of 5.4 kn during seismic data acquisition provided optimal data acquisition conditions.

The common operational parameters used during the cruise leg have been set as following: no tide correction, equidistant beam coverage, automatic sounding mode and fan coverage, sound velocity at ship's keel from ship's sensor. Beam angles and across-track distance were fixed to $\pm 65^\circ$ and 15000 m, respectively.

Bathymetry data processing and editing

We used the open-source software MB-System (Caress and Chayes, 1996) (Version-5.1.1) and GMT (Version 4.3.1) (Wessel and Smith, 1995) for bathymetric data processing, editing and map generation on board.

A scripted processing sequence was used which has been established during previous BGR research cruises. The scripts perform automatic downloads of the survey data from the operator workstation to a Linux workstation. The next steps involve copying of the original data to separate working directories and converting them into an editable data format. A set of data lists, referencing the data files in the survey directories, is automatically maintained for each survey, the cruise and all project files. Metadata information is inserted. During this cruise a depth filter of 10 to 7000 m is applied and an automatic check for reasonable navigation is performed.

Following this step the data has to be edited manually using the program 'mbedit'. Large parts of the survey covered essentially flat abyssal plains of the NW Pacific plate. This relief allowed to apply a median spike filter, using a 1-2% waterdepth threshold and median values from eleven along-, and nine across-track beams. Raw and edited data plots have been stored in files together with protocols, documenting the state of data processing achieved. After a general introduction to editing and picking bad soundings with 'mbedit', a team of five participants nearly kept up editing the data as they were acquired.

1.8.3 PARASOUND sediment echosounder

R. Freitag, R. Lutz, T. Pletsch, H. Thöle

The PARASOUND P70 system (Atlas Hydrographic, Bremen) installed on RV Sonne combines a high-frequency deep-sea echosounder (NBS, narrow-beam system) for water depth sounding with a low-frequency sediment echosounder (SBP, sub-bottom profiler). Because the SIMRAD EM120 was used for water depth sounding, only the SBP capabilities and settings of the PARASOUND system are described here.

The PARASOUND sediment echosounder utilises the parametric effect, which produces additional frequencies through non-linear acoustic interactions of finite amplitude waves. For example, if two sound waves of similar frequencies (in our case 16 kHz und 20 kHz) are emitted simultaneously, a signal of the difference frequency (4 kHz) is generated. The new component is travelling within the emission cone of the original high-frequency waves, which are emitted within an angle of only 4° . Therefore, the footprint size of 7% of the water depth is much smaller than that of conventional single frequency systems and both vertical and lateral resolution are significantly improved. A disadvantage of this small footprint is the loss of a return signal over areas of greater water depths and over slopes steeper than 2° , where the reflected signal is not captured by the ship's detectors.

PARASOUND settings during cruise SO201-1a

A new software package for controlling the echo sounder (Atlas Hydromap Control) and for acquisition, visualisation, processing and storage of the data (Atlas Parastore) was recently implemented onboard RV Sonne. During SO201-1a cruise we recorded the full profile including reflections from the water column, the seafloor and subsurface echoes down to approx. 200 m (266 ms) both for the Primary High Frequency beam (PHF, 20 kHz) and for the Secondary Low Frequency beam (SLF, 4 kHz). For the signal transmission we used the quasi-equidistant transmission mode with a desired time interval of 500 ms. The acquired data were stored using the ASD, SEG-Y and PS3 formats. The ASD (Atlas Sounding Data) is a raw data file format for the storage of the complete sounding profiles. In contrast, the SEG-Y and PS3 files provided by Atlas Parastore only save the data within the PARASOUND reception window. A detailed description of the settings is provided in Appendix 1.18.

The Parastore manual indicates that there is an automatic mode but during our tests, the automatic mode did not work properly. It was necessary to position the seafloor reflection in the display window by manually moving the depth frame up and down using the large arrow buttons. Thus, even with the recently installed Atlas Parastore the first attention of the echo sounding operators remained system control and the adjustment of the the reception window because only a small depth window close to the sea floor is recorded (normally set to 200 m). The PARASOUND sediment echosounder system was routinely operated on a 24 hour watch schedule. Except for short-term failures the PARASOUND system worked during the entire cruise. The online printing capability was not functional on SO201-1a.

PARASOUND Processing

Processing of Parasound data, comparison between differently processed data and discussion of pros and cons are described in detail in the cruise report of cruise SO197 (RISE BGR08). Therefore only the important steps of data preparation are shown here.

PARASOUND profiles were generated along the magnetic profiles, according to the start and end time of the respective profiles, but no trace interpolation was performed (not necessary). The new Parasound display/processing software ParaStore (Version 3.2.8) offers the possibility to store the SLF (secondary low frequency) data in PS3 format and/or SEG-Y format (81 μ s). PS3 files were used as input for REFLEXW and SEG-Y files were used for processing with Seismic Unix.

Creation of the Parasound profiles along magnetic lines can be done with the software REFLEXW or by using a combination of Unix and Seismic Unix (CWP) commands e.g.:

```
FILES=`ls *sgy` ; for i in $FILES; do segyread tape=$i \ endian=0 conv=0 over=1 >$i.su ; done
```

```
FILES=`ls *su` ; cat $FILES | sushw key=tracl a=1 |segymhdrs\
```

```
segymwrite tape=Whole_profile.segy verbose=1 endian=0
```

(this assumes all files of one profile are in one directory)

PARASOUND data along MCS profiles were processed with the software REFLEXW in such a way, that the resulting Parasound profile can be loaded as an additional class to the existing MCS data. The single processing steps are as follows:

Selection of ps3 files according to their date and time (see profile list)

Import of selected files

Conversion of coordinates in degrees to UTM coordinates (Zone 59 north).

File->Edit TraceHeaders->TraceHeaderMenu->UTM-conversion

Definition of start and end trace of the Parasound profile according to start and end coordinates of the MCS profile.

File->Edit TraceHeaders->TraceHeaderTabella

Extraction of selected trace range:

Processing->Edit traces/traceranges->Extract

Update of distances in new profile (see step 4, update distances button)

Interpolation of traces according to the number of traces in MCS profile (trace incr.=length of profile/CDP-1)

Processing->Trace Interpolation/Resorting->Make equidist. traces

Export of processed data.

File->Export (segy)

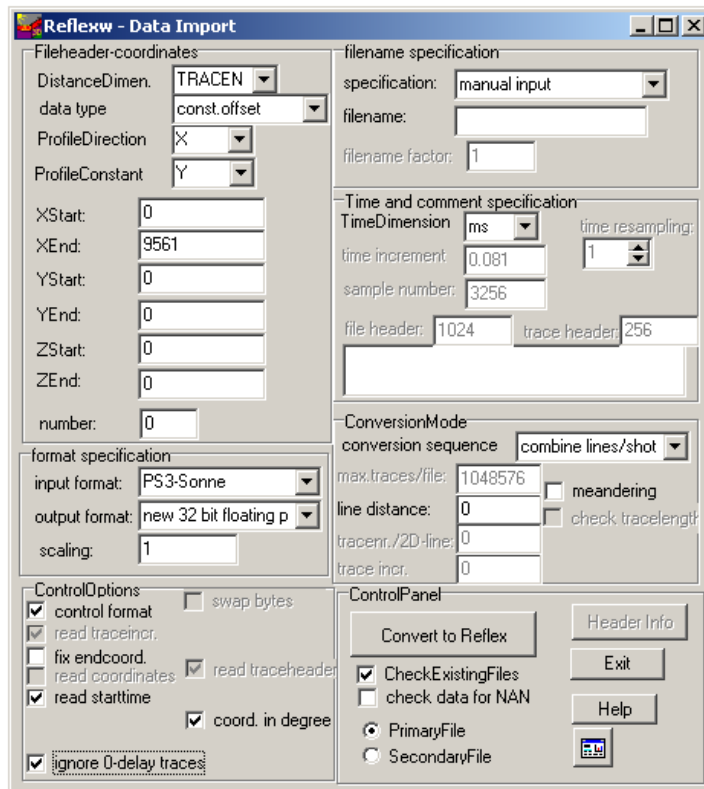


Fig. 1.8.2: PARASOUND processing, step 2, data import.

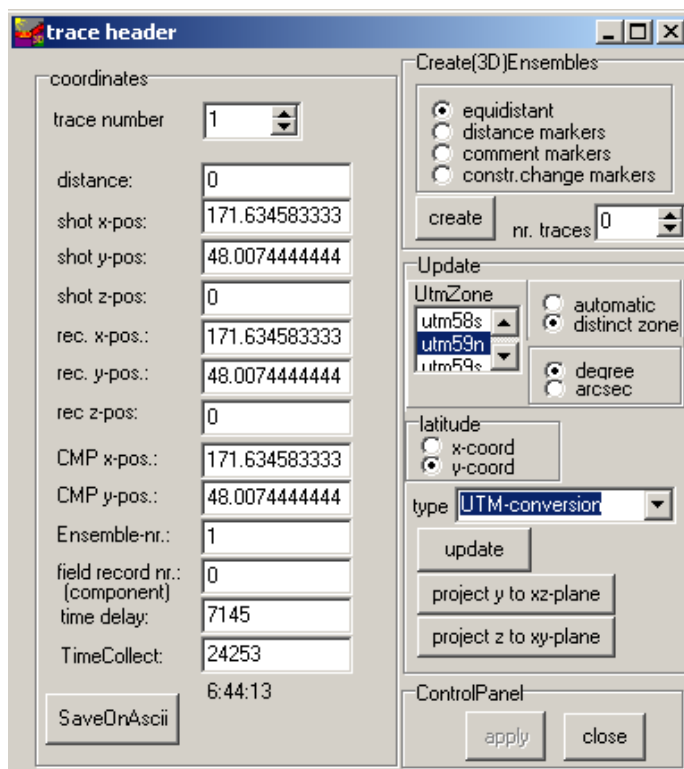


Fig. 1.8.3: PARASOUND processing, step 3, UTM conversion.

edit trace header coordinates

trace-nr.	distance	shot-x	shot-y	shot-z	rec.-x	rec.-y	rec.-z	time delay	gain	time collect
1	0	547330.152	5317322.45	0	547330.152	5317322.45	0	7145	1	24253
2	0	547301.172	5317319.12	0	547301.172	5317319.12	0	7145	1	24264
3	0	547270.121	5317315.78	0	547270.121	5317315.78	0	7145	1	24274
4	0	547241.116	5317315.54	0	547241.116	5317315.54	0	7145	1	24285
5	0	547210.064	5317312.20	0	547210.064	5317312.20	0	7185	1	24296
6	0	547181.085	5317308.87	0	547181.085	5317308.87	0	7200	1	24307
7	0	547147.961	5317305.51	0	547147.961	5317305.51	0	7292	1	24319
8	0	547114.838	5317302.15	0	547114.838	5317302.15	0	7292	1	24330
9	0	547085.833	5317301.92	0	547085.833	5317301.92	0	7292	1	24341
10	0	547054.781	5317298.57	0	547054.781	5317298.57	0	7292	1	24352
11	0	547025.801	5317295.25	0	547025.801	5317295.25	0	7292	1	24362
12	0	546996.796	5317295.01	0	546996.796	5317295.01	0	7292	1	24373

topography (x,z values) source <-> rec. check rec.coordinates
 update shot z-pos. x <-> y factor f.check: 10
 update receiver z-pos. project on x
 use x-traceheadercoord.

Fig. 1.8.4: PARASOUND processing, step 4, definition of start and end traces of profile

Edit traces/traceranges

EditTraces EditTraceRanges

	1.trace nr.	2.trace nr.
1	1	10934
2		0
3		0
4		0
5		0
6		0
7		0

Remove Insert Change

 3178.8 HZ
 original spectrum -7.38989

nr. 1

start x-coord. 0 end x-coord. 0
 start y-coord. 0 end y-coord. 0

apply on example trace change(%)
 apply on original data 20

SequenceProc.

Fig. 1.8.5: PARASOUND processing, step 5, extraction of selected traces.

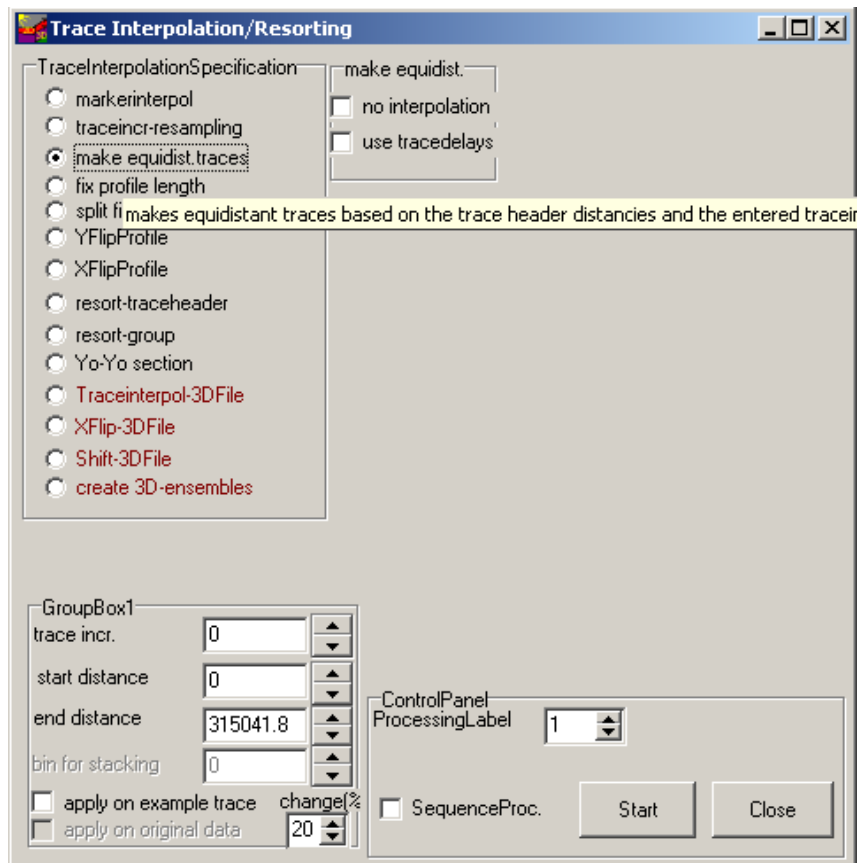


Fig. 1.8.6: PARASOUND processing, step 7, make equidistant traces.

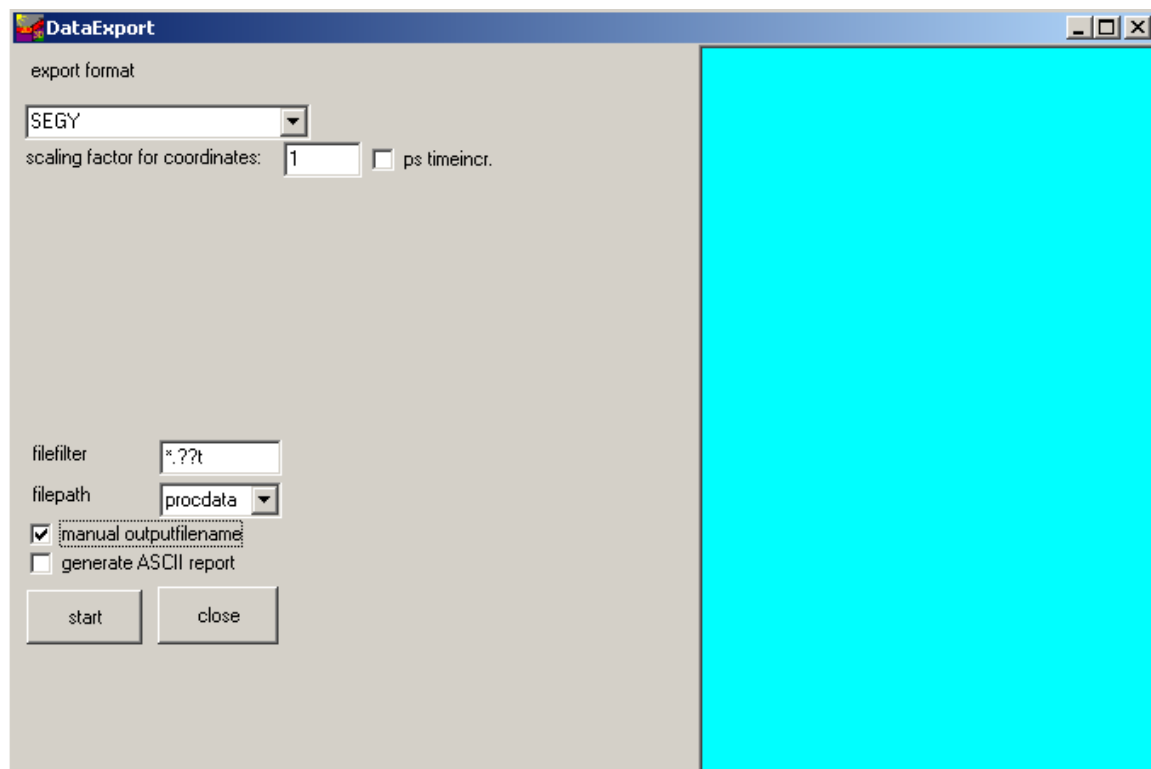


Fig. 1.8.7: PARASOUND processing, step 8, data export.

1.9 Computer facilities/network and data acquisition system

H.-O. Bargeloh

In addition to the shipboard computers, BGR provided several desktop and laptop computers to carry out the acquisition and storage of the collected data (Fig. 6.2.1). Computers were installed in the geology laboratory (acquisition of seismic data) and in the magnetic laboratory (collection of magnetic and gravity data, shipboard database). All PCs used operating system Windows XP. Some were alternatively run under Linux 9.1.

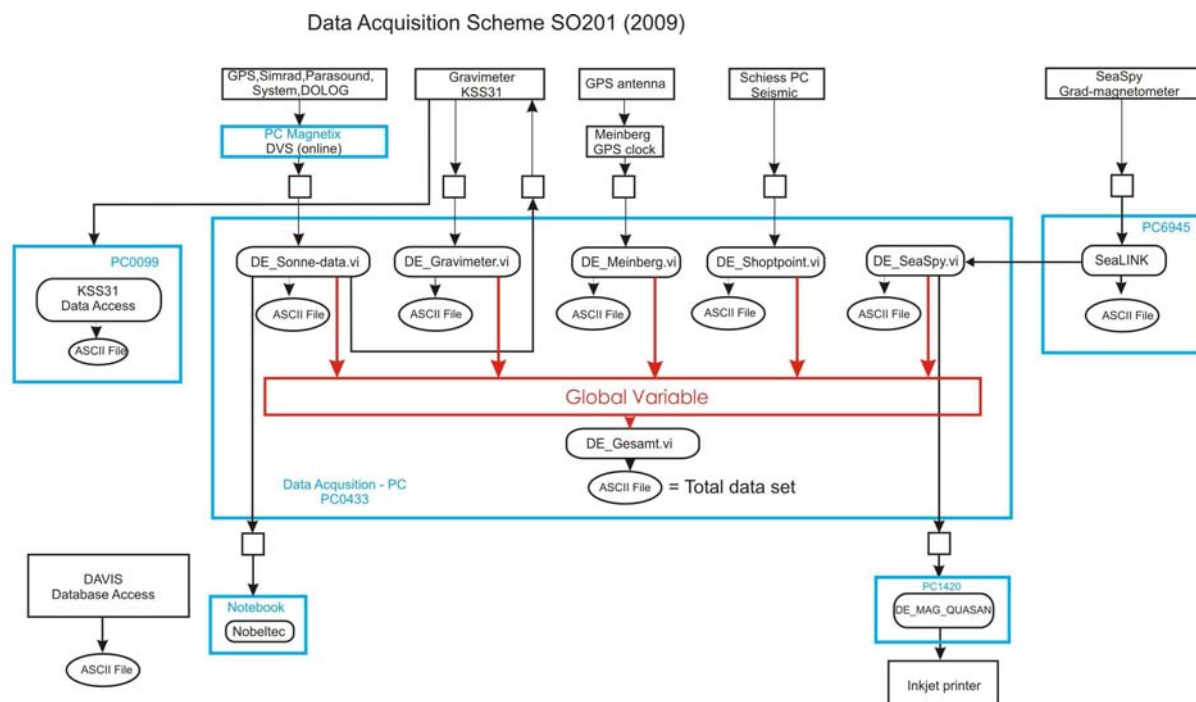


Fig. 1.9.1: Setup for data collection and storage installed during SO201.

A shipboard computer (PC Magnetix) provided the following data from the ship's navigation system once per second:

- position, speed and course from GPS
- heading from the gyro compass
- speed from the Doppler-sonar (DO-Log)
- water depth values from the SIMRAD EM120 multibeam echosounder (center beam only) and from PARASOUND
- Kongsberg MRU5: Roll, Pitch, Yaw
- weather data

The BGR computer PC0099 controls the functions of the marine gravimeter. Measured gravity values are sent to the data acquisition PC (see below).

A notebook computer was installed in the magnetic lab to provide a visual display of the position of the ship in relation to the profile network by a navigation software package (Fugawi Global Navigator). This software permanently displayed the ship's position on a nautical map along with the positions of planned and measured profiles. The software package Fugawi Marine ENC for planning of the survey lines was installed on a PC in the chief scientist's cabin.

PC6945 was used to control the operation of the SeaSpy marine gradiometer and to display the collected magnetic data. The Magson magnetometers (which were also used for experimental purposes) have no real-time data transmission to the ship. Their data were stored on flash cards within the instrument.

The seismic instruments (G-Guns and streamer) were controlled using BGR-developed and industrial software installed on PCs which were set up in the geology laboratory. All seismic data were stored intermittently on harddisk and sequentially transferred onto tape. Shotpoint data were transferred to the data acquisition system as discussed below.

The PC used for the acquisition of navigation data, shotpoint data, gravity data, magnetic gradiometer data, time in UTC, depth, and water sound velocity (PC0433) was equipped with a large number of serial and other ports. Each of the data strings was written into the memory of the data acquisition PC by real-time programs developed using LabView software. The PC was connected to a BGR-provided Meinberg GPS-clock that provided a uniform time reference to all collected data. Analog recordings were produced for the total magnetic intensity, the gradient, and the raw gravity data.

The data were pre-processed on various computers. All data which are part of BGR's standard operations were transformed into an special data format (PC1420) within a procedure that checks, reformats, and collects the data items to one data set every 20 seconds.

The multibeam bathymetry data were processed on various PCs. One PC with Windows XP and Caris 6.0 installed was used for editing raw bathymetry data with the HIPS+SIPS software package. The bathymetry data were edited using the mbedit software package on PCs provided by RF and BGR.

1.10 Multi-channel seismics

D. Franke

Summary

Source

Source Depth: 6 m
Av. Shot Interval: 50 m

Navigation

Navigation: antenna position is recorded
Distance Antenna - Stern: X = 59.4 m
Y = 2.2 m (to port side)
Distance Stern – Center Source X = 49.5 m
Distance Stern – Center 1st Channel X = 202 m
Distance Center Source – Center 1st Channel X = 152.5

Streamer

Streamer Depth: 15 m
Receiver Interval: 12.5 m

SOD	136 ms
Seismic Channels	1 – 276 (1 is closed to vessel)
No. AUX Channels	5
Sample Rate	4 ms
Samples/Trace	3501
Record Length	14000 ms

Tape

Tape Format	SEGD 8085
Instrument	SERCEL 408XL

1.10.1 Airgun arrays

D. Franke

During the cruise the BGR's G-Gun airgun array was used as seismic source. The G-Gun array is subdivided into two sub-arrays with eight guns each (Fig. 1.10.1). Each sub-array consists of four two-gun clusters. The volumes of the individual guns of the port array range between 380 in³, 250 in³, 180 in³ and 100 in³ whereas in the starboard array volumes between from 250 in³, 200 in³ 120 in³ and 70 in³ are used. Each sub-array is equipped with two near-field hydrophones. The maximum total volume used was 3,100 in³ (50.8 l) and the towing depth was 6 m throughout the survey. Each sub-array has a total length of 15.56 m.

The pressure delivered from the compressors was 2,100 psi (145 bar). Triggering and synchronisation was controlled by a SYNTRON GSC-90 system. It is capable to control up to 32 airguns.

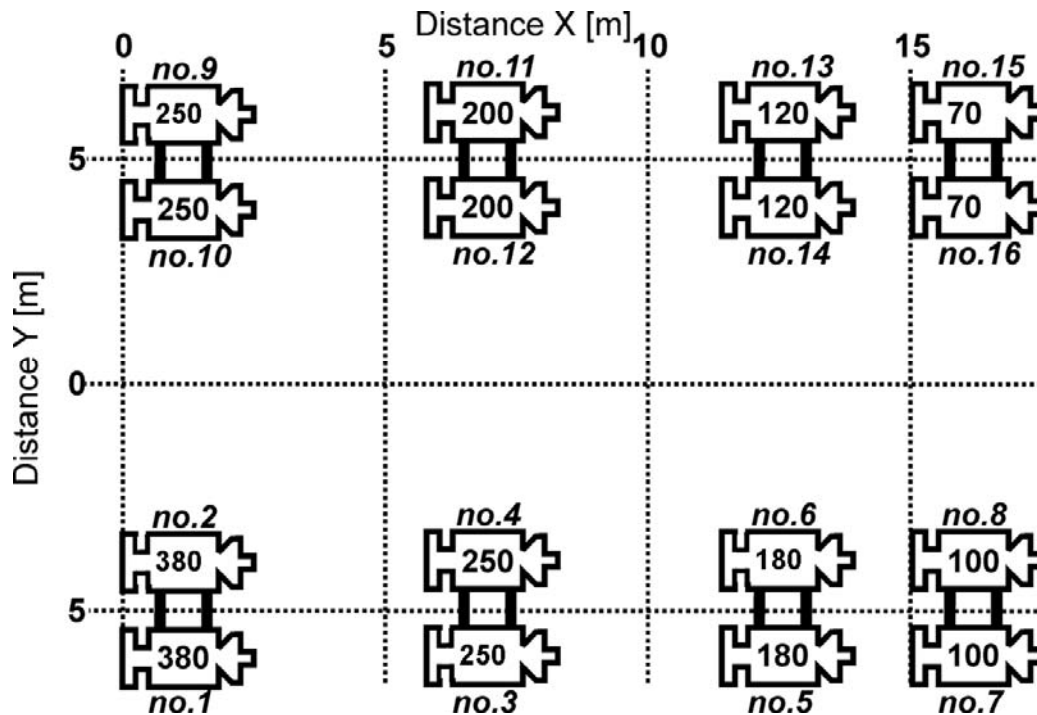


Fig. 1.10.1: Configuration of BGR's airgun system during cruise BGR08 SO197

Shots were triggered time-dependent every $18 \text{ s} \pm 0.3 \text{ s}$. At an average ship speed of 5.4 kn the resulting shooting distance is 50 m. A detailed description of shot triggering is given below. The far-field signatures of the G-Gun array and the frequency spectrum are shown in Neben et al. (2003; Cruise report of the BGR03 survey).

The G-Guns proved to be very reliable during the measurements. Maintenance of the guns was minor and was done during turns or during acquisition.

1.10.2 Seismic data acquisition system

D. Franke

BGR's SEAL System and a digital cable with an active length of 3.450 m were used to record the seismic data. The recording system (DigiCOURSE System 3, Fig. 1.10.3) and the streamer control system are interfaced with the Master PC. The system start trigger is generated by the Master PC. Here, the data for the external header, e.g. from the DigiCOURSE System 3, navigation system, GPS-clock, pressure, etc., are received and the external header is generated, stored and sent via an interface to the SEAL system and to the navigation system (Fig. 1.10.4).

One OYO GEOSPACE GS642 thermal plotters for paper printouts of single trace plots was in use for quality control. The plotting parameters were 10 s record length and 25 traces per inch (TPI) for the single trace. An AGC with a 1000 ms window length was applied to the data.

Streamer system

BGR's SEAL streamer consists of 23 seismic sections (ALS) with 276 channels (Fig. 1.10.2) . It has a flexible architecture with redundant data transmission modes, i.e. data transmission may be reconfigured on line failure. Each channel has an individual 24 bit, Sigma Delta A/D converter. The active streamer sections have a diameter of 50 mm.

The SEAL recording system is capable to handle a maximum recording capacity of 960 channels (@ 12.5 m; 2 ms) per streamer, a maximum record length of 99 s, and a maximum number of 20.000 seismic channels and 60 AUX channels. The sampling rate may vary from 1/4 ms, 1/2 ms, 1 ms, 2 ms to 4 ms. During the cruise we sampled the data at 4 ms.

Up to 6 tape drives may be operated either simultaneously or in alternating modes. Supported drives include 3490E, 3590, 3590E, DLT, LTO, IBM 3580. We operated one DLT 7000 during the cruise. Data format is 4byte - SEG-D revision 2, demultiplexed 32 bit IEEE, Code 8058.

The DigiCOURSE System 3 system was used to control the vertical streamer position (depth) and to measure the heading. DigiCOURSE System 3 is a hardware and software package that controls and collects data from a network of acoustic sensors and streamer positioning devices. DigiCOURSE System 3 has online command, diagnostic, and performance-monitoring capabilities (Fig. 1.10.4). System 3 employs a modular architecture which provides for a variety of configurations and levels of functionality. The minimum system equipment configuration includes two real-time processors: an Operator Interface (OI) and a Data Management Unit (DMU), a Line Interface Unit (LIU), and cable-mounted measuring devices, birds, and compasses. We had the cable at a depth of 15 m \pm 1 m.

Tail buoy system

The radar tail buoy with beacon, flashlight and Inmarsat GPS receiver is powered via the streamer.

In-water equipment

The seismic data are amplified, filtered, and analogue-digital converted within the SEAL streamer by using the following main modules installed in the streamer: 1 LCI, 1 DCXU, 3 LAUM, 1 TAPU, 1 AXCU and 1 HAU.

Fahrt SONNE 201 -KALMAR-
Blatt Fahrtbericht
Profil BGR09 -alle Profile-



Lead In (190m)	SHS 6m	HAU	HESE 50m	HESE 50m	HESA 10m
	1461	193	1431	2692	1653

RUK3		RU4/R1		RUK5/R2			RU6				RUK7/R3			
ALS 1 1 - 12	ALS 2 13 - 24	ALS 3 25 - 36	ALS 4 37 - 48	ALS 5 49 - 60	LAUM 1	ALS 6 61 - 72	ALS 7 73 - 84	ALS 8 85 - 96	ALS 9 97 - 108	ALS 10 109 - 120	LAUM 2	ALS 11 121 - 132	ALS 12 133 - 144	ALS 13 145 - 156
7030	7029	8640	7027	8630	451	8629	7023	7024	7021	8633	557	7020	8628	8637
RU8		RUK9/R4			RU10			RUK11/R5						
ALS 14 157 - 168	ALS 15 169 - 180	LAUM 3	ALS 16 181 - 192	ALS 17 193 - 204	ALS 18 205 - 216	ALS 19 217 - 228	ALS 20 229 - 240	LAUM 4	ALS 21 241 - 252	ALS 22 253 - 264	ALS 23 265 - 276	TAPU	TES 50m	STIC 25m
8617	8634	480	8636	7016	7012	7015	8638	1710	8635	8631	8627	186	1474	1438

Gesamtlänge: 3720m

TS	
4092	

	S/N	
130m RU1 :	36707	
180m RUK2 :	42778	
340m RUK3 :	36273	
490m RU4 :	36993	Recovery
940m RUK5 :	42461	Recovery
1390m RU6 :	36521	
1840m RUK7 :	36194	Recovery
2290m RU8 :	36274	
2740m RUK9 :	36056	Recovery
3190m RU10 :	37699	
3640m RUK11 :	42487	Recovery



Kompassbird: schwarzes Endteil

Fig. 1.10.2: Streamer configuration used.

ALS Acquisition Line Section

With a length of 150 m, an ALS acquires data from 12 channels with an equal spacing of 12.5 m.

Each channel receives data from a group of 16 hydrophones, with a capacity of 256 nF (@ 20°C), a sensitivity of 20 V/bar open circuit, and 17.4 V/bar, with electronics included.

An analogue to digital converter (*FDU*, Field Digitizer Unit for 2 channels) with a test signal generator is implemented in each Acquisition Line Section (ALS).

HAU Head Auxiliary Unit

The HAU assures power supply for the TLFOI and measures the tensile strength value between the cable and the vessel. During cruise BGR09 the stress was about 1.1 t.

HESE Head Elastic Section Extension

2 HESE and one HESA (Head Elastic Section Adapter) were in use between the HAU and the active sections (ALS) to connect the streamer and the head section. The HESA hosts the waterbreak hydrophone. One SHS, a 6m non-elastic section, was placed between the Lead-In and the HAU.

LAUM Line Acquisition Unit, Marine

Manages data compression, data routing and power supply for the ALSs.

As 1 LAUM is for 60 channels 3 LAUM were in use during the cruise.

TAPU Tail Acquisition and Power Unit

Situated at the end of the active streamer the TAPU is made up of a LAUM with common duties and may manage the power supply for the tail buoy. The latter function was not used for the BGR streamer. The end of the streamer is made up by a Tail elastic section (TES) and the Tail buoy (TB). The tail buoy (constructed by Prakla-Seismos) used was equipped with radar reflector, radio beacon, and flash light.

Onboard equipment

AXCU Auxiliary Channel Unit

The AXCU box contains FCU2M (Field Digitizer Unit 2 Marine). It is used to convert analogue data coming from the airgun array and the waterbreak-section.

5 auxiliary channels (AUX) are recorded (max. 6): Aux1= WB (waterbreak), Aux2=STB1 (hydrophone 1 at starboard gun array), Aux3= STB2, Aux4=BB1 and Aux5 = BB2 (hydrophone 2 at port gun array)

CM408XL Control Module eXtra Large

Designed with a modular configuration, the CMXL controls the 276 acquisition channels (max. 10000). It manages the flow of the acquired data between the streamer and the recording system (PRM- managed) and peripheral equipment(tape drives, plotters, navigation and positioning, QC system) via SCSI and ethernet links. Two CMXL may be used in parallel to increase the maximum channel capacity to 20.000.

Within the CM408LX module a Line Controller Interface board (LCI) Board is situated. This interfaces with the master pc shooting system and formats the data to IEEE format

DCXU & Deck Cable Cross Unit & Line Acquisition Unit, Cross line, Marine

LAUXM The Deck Cable Unit, housing a Deck Cable Interface (DCI) and a Line Acquisition Unit - Cross line - Marine (LAUXM), assures the connection between the streamer and the Control Module (CMXL). It also links the streamer to the necessary control modules and triggers the emergency stop with a warning light installed close to the winch, when needed.

PWM PoWer Module & PoWer Module Controller

PWMC The streamer power module, generates a +175/-175 VDC voltage, using two separate rails – called HV1 and HV2 – to supply power to the electronics of the streamer.

Each PWM is linked to a Power Module Controller (PWMC). For a PWM being able to be put ON, either in REMOTE or LOCAL mode, the PWMC must be connected and powered on: an ENABLE signal is sent from the PWMC to the PWM. Leakage, overload HV-alarm, and emergency stop from the winch are managed by the PWMC.

HCI Human Computer Interface

The HCI is the control unit for the operator. Script files can be saved to and/or loaded from another computer and an online help is available. A QC software running on a

'SunBlade 150' workstation enables the control of the following functions and settings via a permanent graphic display:

- Operation and function control of the different units (PWMC, PRM, QC) with automatic central control unit acceptance tests
- Concise display of system activity
- Automatic log of observer report data
- Display of power status
- Acquisition sequence controlled by external shooting system
- On-line real-time signal graphic analyser
- Printout of all parameters

PRM Processing Module

The PRM is a processor software module that is used for transferring the data to and from the cartridge drive, to the plotter and the SeaProQC system. It is installed on a separate 'SunBlade 2500' workstation.

SeaProQC Sea Processing Quality Control

Continuous online seismic data quality control is performed using a SeaProQC workstation 'SunBlade 2500' connected directly to the PRM without slowing down the acquisition. Three main windows are used for quality control:

The History display window with bar graphs shows a summary of errors and source attributes for the successive shots processed by the SeaProQC. It displays the attributes of the data from the previous shots.

The Normal display window shows the latest incoming SEG-D shot record. The traces are displayed in the time/distance range with the noise of each trace on top of the display.

The Single Trace window shows the data of one selected channel from the streamer. With each new shot the display is updated with the new acquired trace added to the window. Four single trace windows may be opened simultaneously.

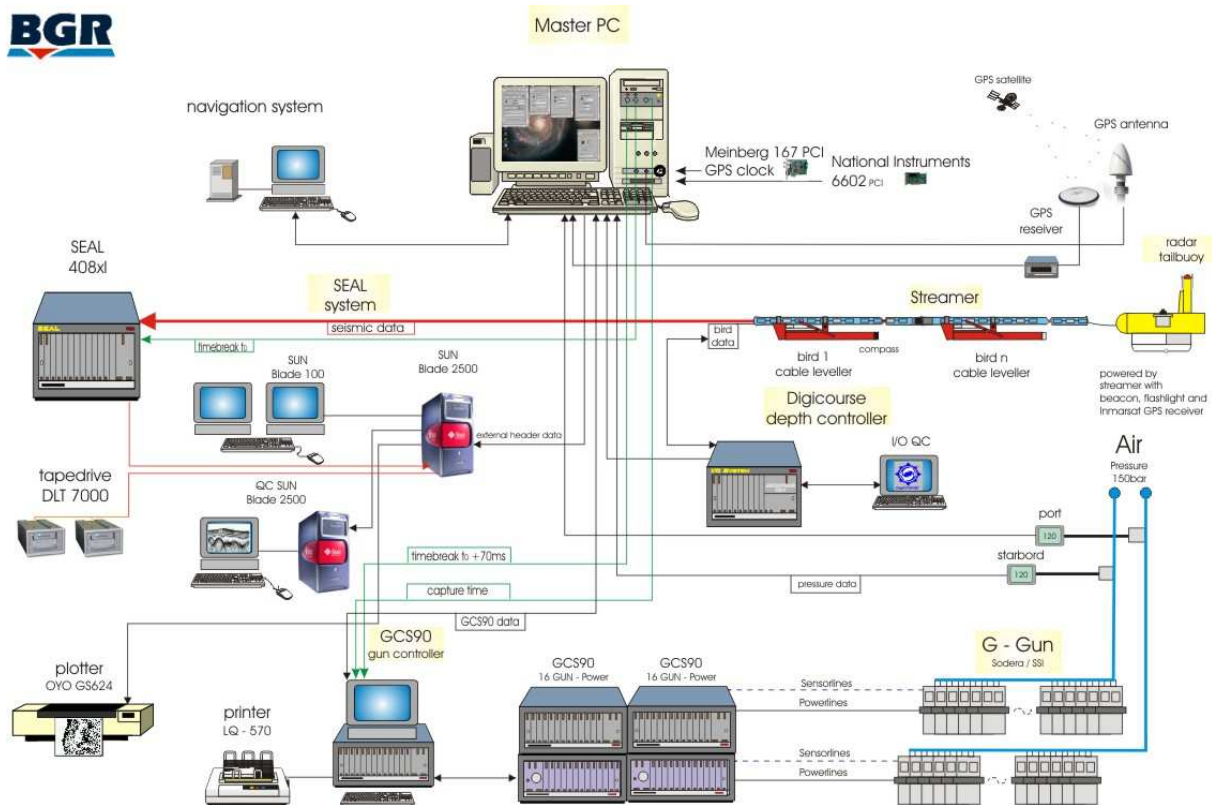


Fig. 1.10.3: Signal flow diagram for BGR's reflection seismic data acquisition system.

Shot Triggering

The shots were triggered in time intervals of 18 seconds. Thus, the intended shot distance of 50 m was achieved at a speed of 5.4 knots. In general, the distances were very constant (normally less than 5 m deviation) due to use of a differential GPS. A constant shot time interval based on time or distance triggering at constant speed causes problems with multiples from previous shots which survive CDP sorting and in most - more severe - cases cannot be attenuated through processing procedures like e.g. predictive deconvolution and dynamic correction and stacking. To avoid this problem the time triggering interval was superposed with a random time function of ± 0.3 s. This ± 0.3 s interval is negligible for the shot distance as a scattering of only about 1 m is generated, but after CDP sorting the multiples from previous shots are not aligned and will be weakened through stacking.

The shot time interval with the random function, representing an even distribution was generated on the Master PC (Fig. 1.10.4) with an interface card for triggering the airgun array via the SEAL408XL system and the Syntron GCS 90 shot trigger device.

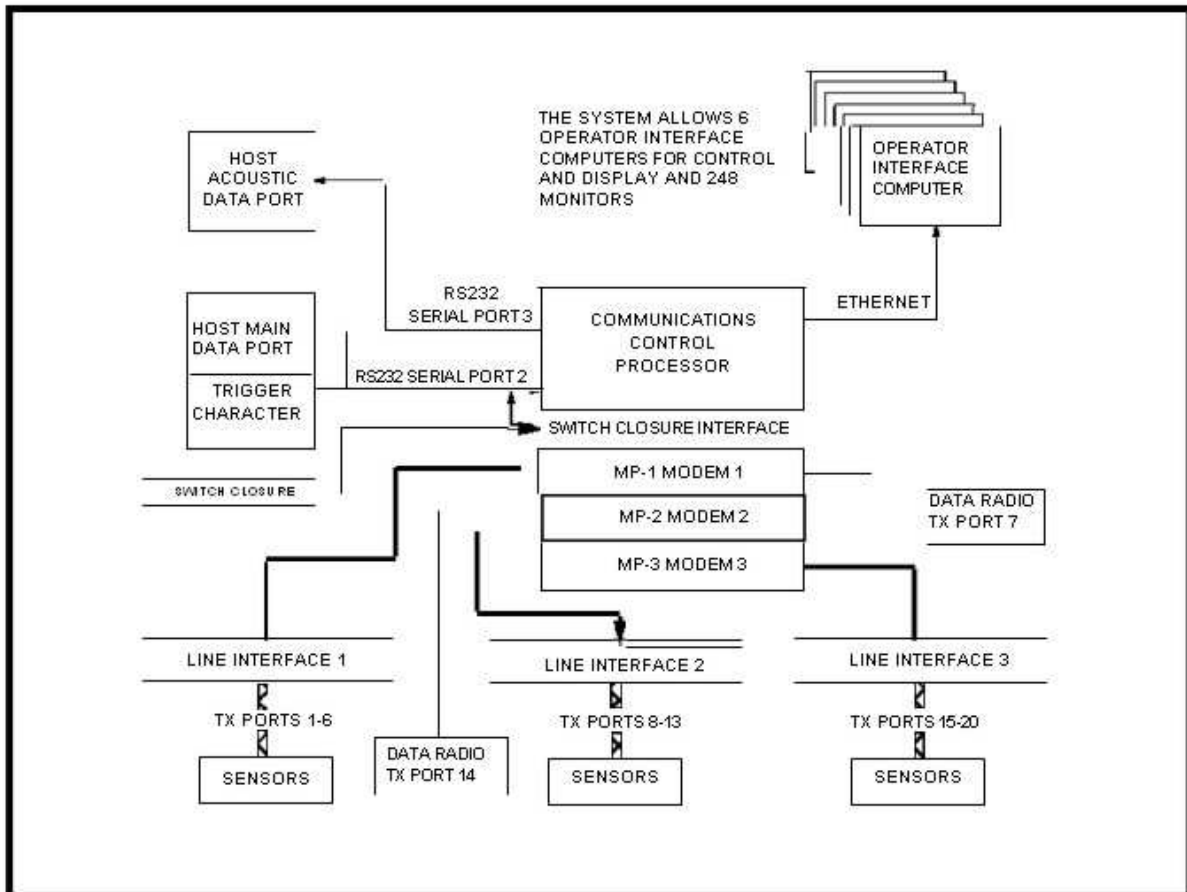


Fig. 1.10.4: Principal configuration of the DigiCOURSE 3 System

Quality Control

Quality control during acquisition comprised:

- Continuous control of the airgun pressure.
- Observation of the hydrophone signals within the arrays and adjustment of the trigger delays for an optimum signal.
- Checking and recording the streamer depth and position (heading) every shot via the control screen of the DigiCOURSE System 3 system. These data are stored in the header and are written on the field tapes.
- Continuous checks whether all sections of the streamer are free of abnormal noise and give about the same signal amplitude. This was done for every shot via the QC Graphics display of the SeaProQC system.

Continuous observation of the single resp. near trace records.

1.10.3 Streamer Depth

At the end of the survey we tested the effect of the streamer depth on the frequency content of the data. For a constant number of 75 shots the streamer was at a depth of 15m, 12 m, 8 m, and 6 m. The following figures show the stacked sections and the corresponding frequency spectra.

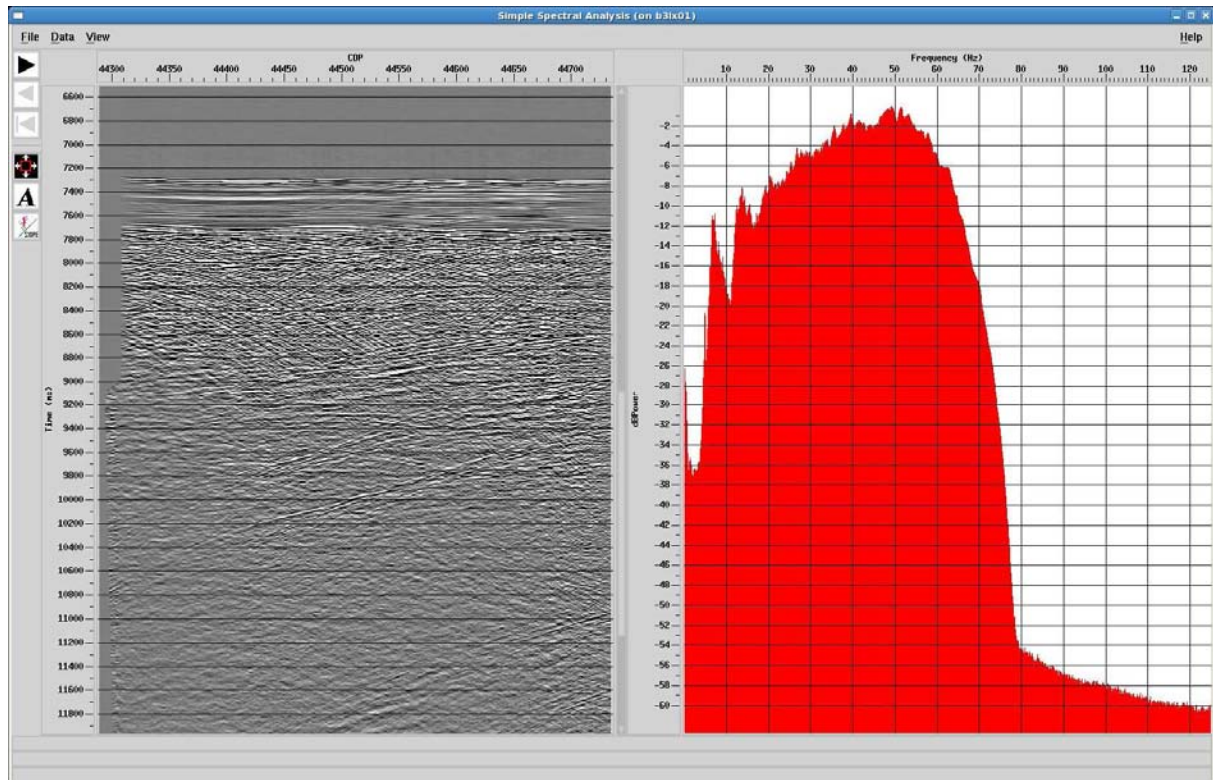


Fig. 1.10.5: Frequency spectra with different streamer depths: 6 metres.

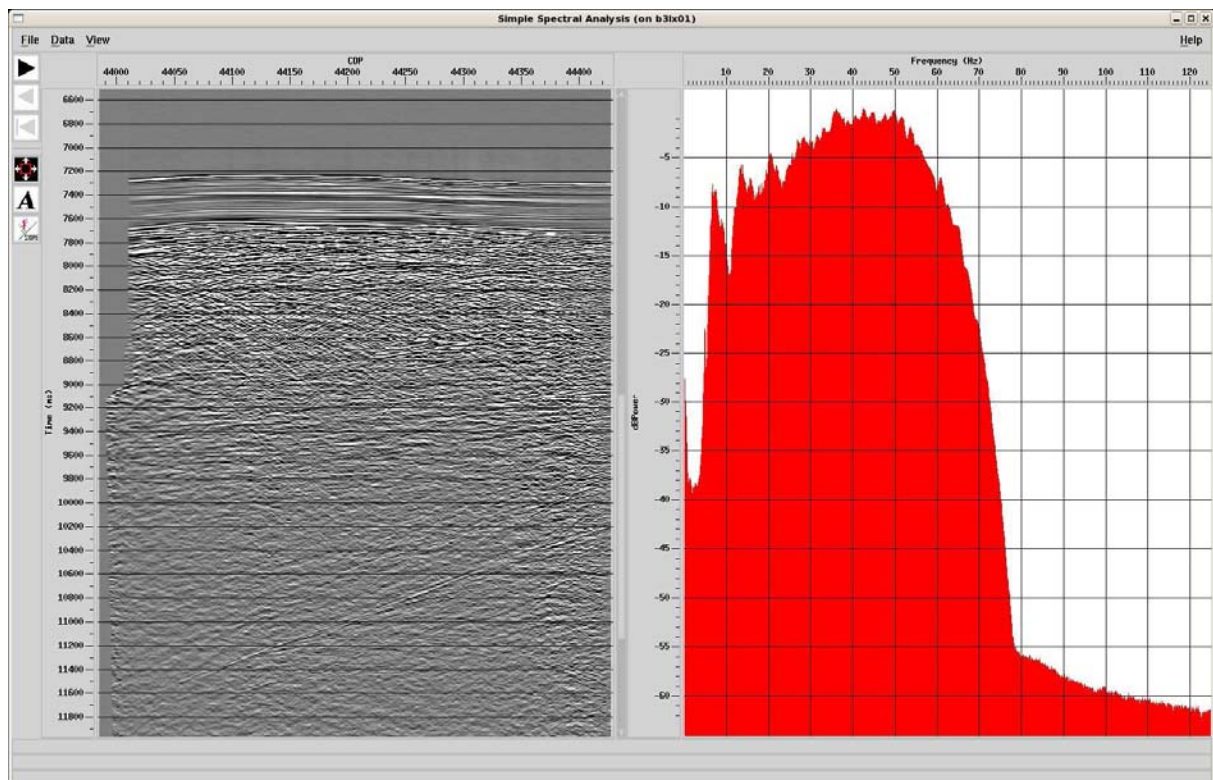


Fig. 1.10.6: Frequency spectra with different streamer depths: 8 metres.

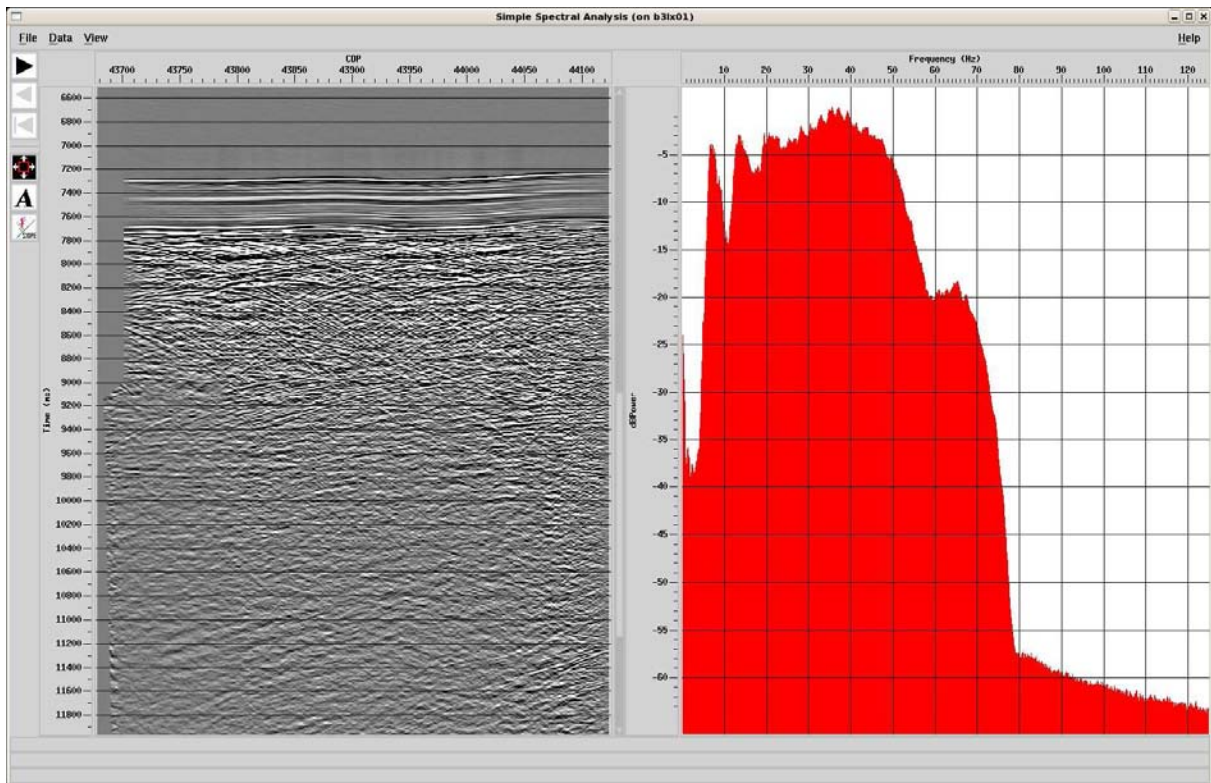


Fig. 1.10.7: Frequency spectra with different streamer depths: 12 metres.

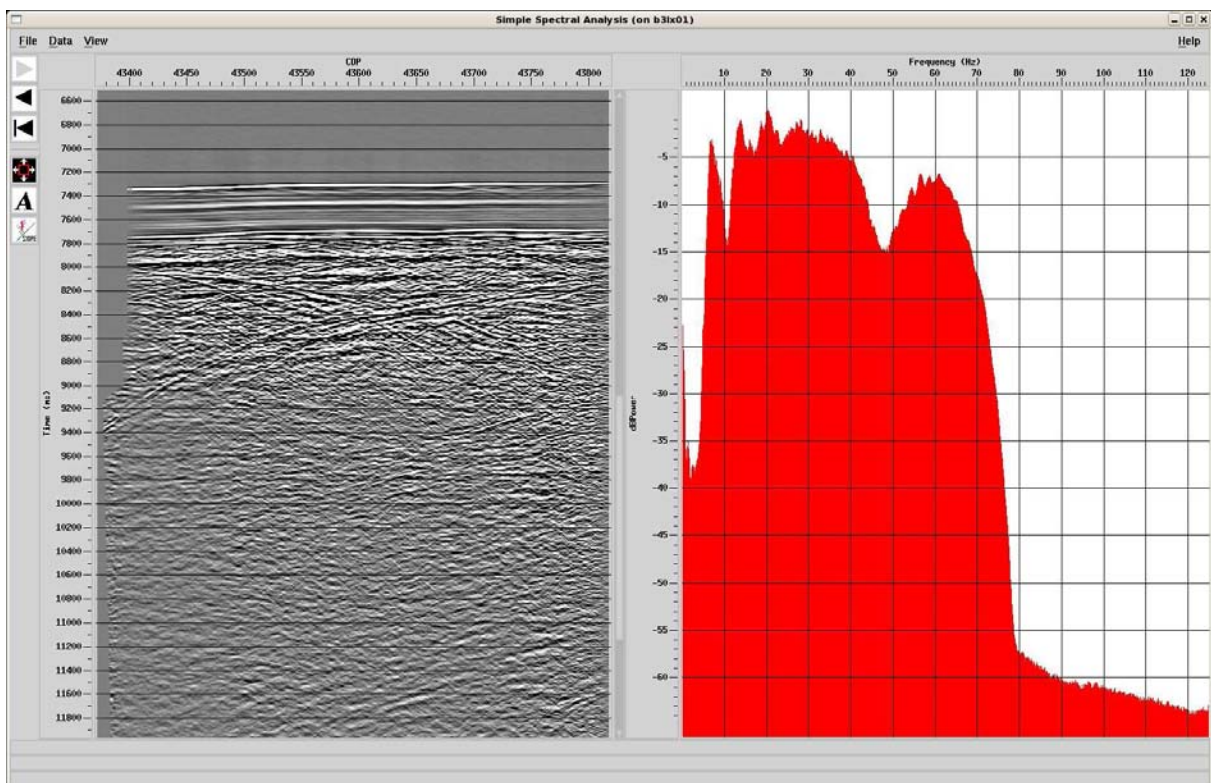


Fig. 1.10.8: Frequency spectra with different streamer depths: 15 metres.

1.10.4 Onboard processing of seismic reflection data

D. Franke

Introduction

Seismic data processing was carried out onboard in order to control the quality of the data and to provide stacked and migrated versions of the profiles for onboard interpretation. All lines were processed (Tab. 1.10.2). Two Linux workstations with ProMAX™ 2D, Version 2003.12.1 licenses were available. Each workstation (Fig. 1.10.9) has two Intel Xeon CPUs (2.8 GHz) with 512 kB cache size, an internal memory of 3.6 GB and a 120 GB internal disk. The operating system is RedHat Linux WS release 3 (Taroon). A raid disk array with 2400 GB disk space is accessible from both workstations. Both workstations make use of the raid system for storage of seismic data, of the database and of job flows. One ½" DLT drive was connected for data loading.



Fig. 1.10.9: Onboard processing system.

SEG-D input from tape

Data were loaded from DLT tapes and reformatted to ProMAX internal format. The shot-ordered data consisted of 276 data channels and 5 auxiliary channels sampled at 4 ms with a recording length of 14000 ms. The auxiliary channels contained data from the waterbreak hydrophone and four near-field hydrophones, two inside the starboard array and two inside the port side array.

SEGD external trace header

In SEG-D 8058 Revision 1.0 the file header block consists of three 32-Byte general header blocks, sixteen 32-Byte channel-set header blocks, and a 1024-Byte extended header block. These 1632 bytes are followed by the external SEG-D header, starting at byte location 1633 with a length of 4096 byte. The SEG-D input process (Segd Input) in ProMAX allows remapping of the SEG-D main header entries. By default, this option is set to accept only the default SEG-D header words. We use this option to read in

		Header word (Format, Byte Location)
Profile Number	->	LINE_NO (3C, 1639)

Shot Number -> SP_PC (5C, 1648)
 Antenna Latitude -> lat_anta (3C, 1769)
 Antenna Latitude Digits -> lat_antb (5C, 1773)
 Antenna Longitude -> lon_anta (3C, 1780)
 Antenna Latitude -> lon_antb (5C, 1784)
 Water Depth (m) -> w_depth (5C, 1808)

Floating point positions (lat_ant, lon_ant) were calculated using Trace Header Math with the formula $lat_ant = lat_anta + (lat_antb/100000.0)$.

As an example the entry in the field "Input/override main header entries" for the Shotpoint is shown:

sh_pc, Shotpoint,5C,,1648/

It is intended to have UTM X-Y values directly written to the trace header in the future.

Geometry setup

The ProMAX 2D Marine Geometry Spreadsheet was used to read in all geometry-relevant parameters. It includes the following steps which have to be carried out in the geometry setup sequence.

File. UKOAA Import. The navigation data were transformed by the navigation group into rectangular UTM coordinates and saved in the format "STANDARD UKOAA 90 Marine 2D". For importing the data into ProMAX, the letter in the first column (Record Id) has to be an "S".

Setup. For this cruise the following parameters were valid: 12.5 m for nominal receiver spacing, 50 m for nominal station interval, 6 m for nominal source depth and 15 m for receiver depth. All units are given in metres.

Sources. The following columns in the spreadsheet have to be filled using the "Edit" option: "Source" and "Station", beginning with 1 and succeeding in increments of 1. The streamer azimuth has to be calculated using "auto azimuth". The algorithm used for this by ProMAX is very crude. It is based only on the first and last source point, the calculated azimuth is assigned to all source positions. The column "Src Pattern" has to be filled with the number of the pattern defined in 4.

Patterns. The streamer and source pattern were defined according to table (Tab. 1.10.1). The channel numbering accounts for the live streamer sections.

Tab. 1.10.1: Streamer source patterns					
Min Chan	Max Chan	Chan Inc	SRC Pattern	X Offset	Y Offset
1	276	1		261.4	-2.2
			1	108.9	-2.2

Bin. The binning consists of three steps:

- a. Assign Midpoint.

- b. Binning. Source station tie to CDP number: 1; CDP Number tie to source station: 10000. This tie fulfils approximately BGR's standard for CDP numbering: The first station with full coverage is tied approximately to CDP 10000. Distance between CDPs: 12.5 m. This implies a nominal CDP coverage of 70 on the reflection seismic lines.
- c. Finalize Database.

TraceQC. Quality control of the binning. Two checks are undertaken here:

- d. Checking the computed offsets with the offsets given in the streamer plan by comparing the values for the last hydrophone group (channel 240) and nearest hydrophone group (channel 1).
- e. Checking if the source and receiver locations (in UTM coordinates) are behind the vessel in relation to the sense of direction?

A further quality control was performed by using the graphical display tools of the database application:

1. CDP fold map (View => Predefined => CDP fold map). X_COORD and Y_COORD – Axes; FOLD: Color coded and as histogram.
2. CDP fold table (Tabular => CDP): List of CMP Number, FOLD, X_COORD and Y_COORD.

SOD time correction

The current Sercel acquisition system starts registration 136 ms before triggering of the airguns occurs. This time delay has been verified on the auxiliary channel containing the signal from the auxiliary hydrophones at AUX CHAN -1 to -5 and on the direct water wave on the groups near to the source. Thus we applied a static shift of -136 ms to the raw data. However, this value should be checked again at a higher sampling rate during the next survey.

Datum correction

The gun and cable depths which were defined during the geometry setup are used to shift the data to sea level. Generally the gun depth was 6 m while the streamer depth was 15 m. Due to the large waterdepth the average water velocity was 1510 m/s. This value is in accordance with measured water velocities by means of sound profiles.

Data quality control (QC)

In addition to the geometry quality control three more control steps were carried out onboard. The water depths in the database, derived from the ship's echo sounder via the UKOOA P190 navigation files, were checked and, if necessary, errors were corrected. The shot gathers were checked for bad traces. If present, these were killed and thus excluded from further processing. The geometry from the database was then loaded to trace headers.

Bandpass filtering and noise suppression

A single Ormsby bandpass filter of about 4-8-60-120 Hz was applied to all traces at all times. These filter values represent the signal spectrum generated by the airgun array and eliminate low-frequency noise which was present in the data because no low-cut filter was applied in the acquisition system. Spike and Noise Burst Edit was applied with the most critical parameter being the Threshold to trip noise edit. Values

around 2 gave the best results. To eliminate transient noise at the streamer's end Surface Wave Noise Attenuation was applied with a velocity of 1500 m/s. In addition Dip Scan Stack was tested (Fig. 1.10.10 to Fig. 1.10.14).

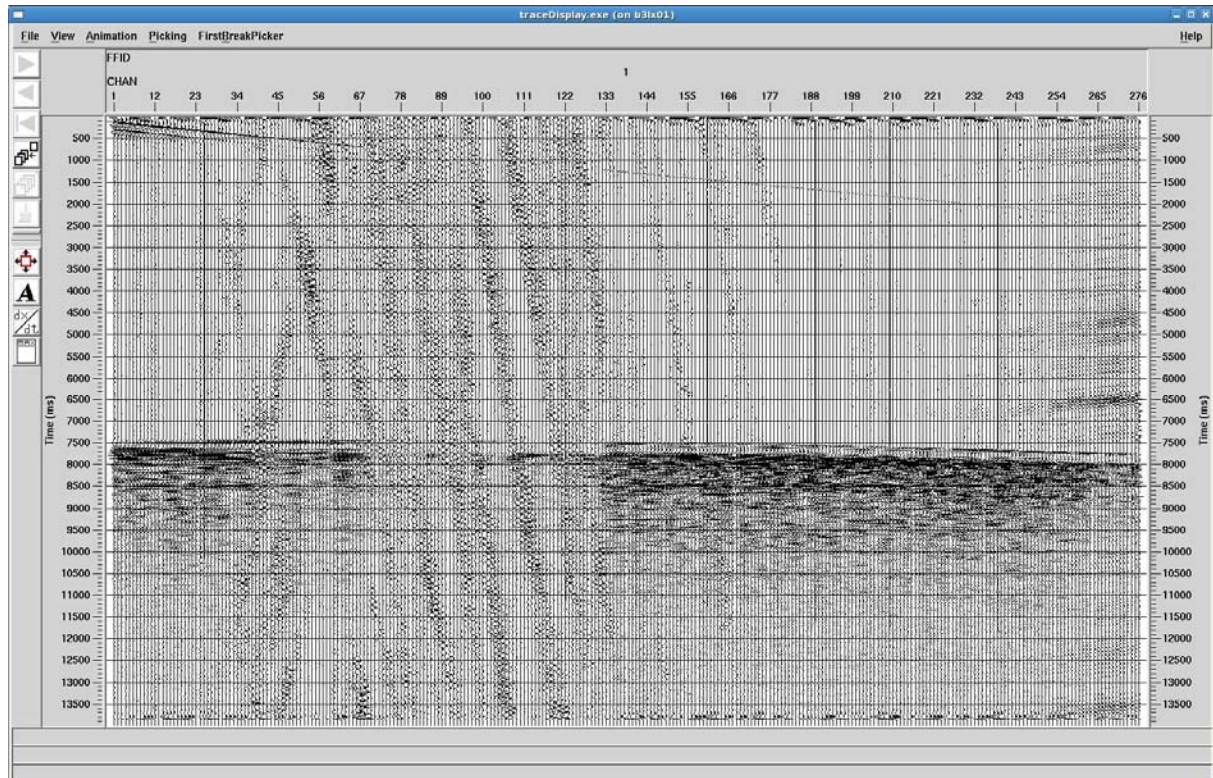


Fig. 1.10.10: Example shot gather after bandpass filtering. Note the low frequency noise burst in the centre of the streamer and at the end of the streamer.

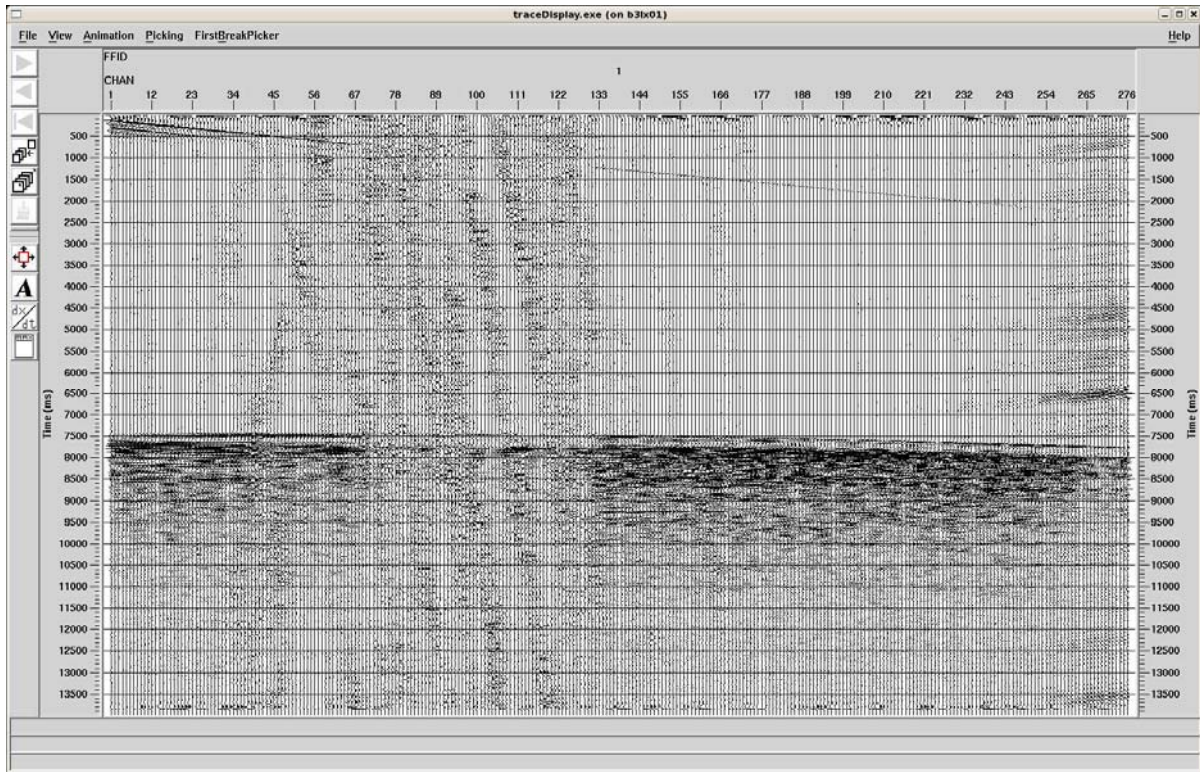


Fig. 1.10.11: Example shot gather after noise burst editing (threshold = 2).

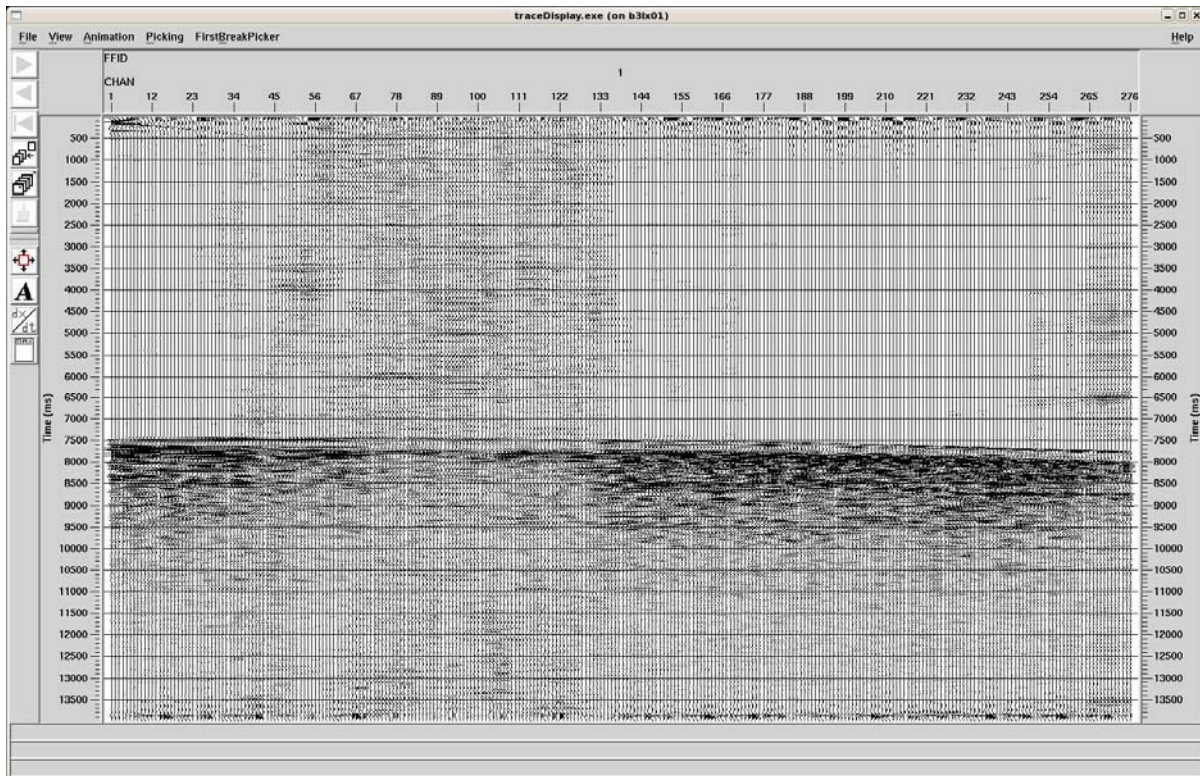


Fig. 1.10.12: Example shot gather after SWNR (1500 m/s).

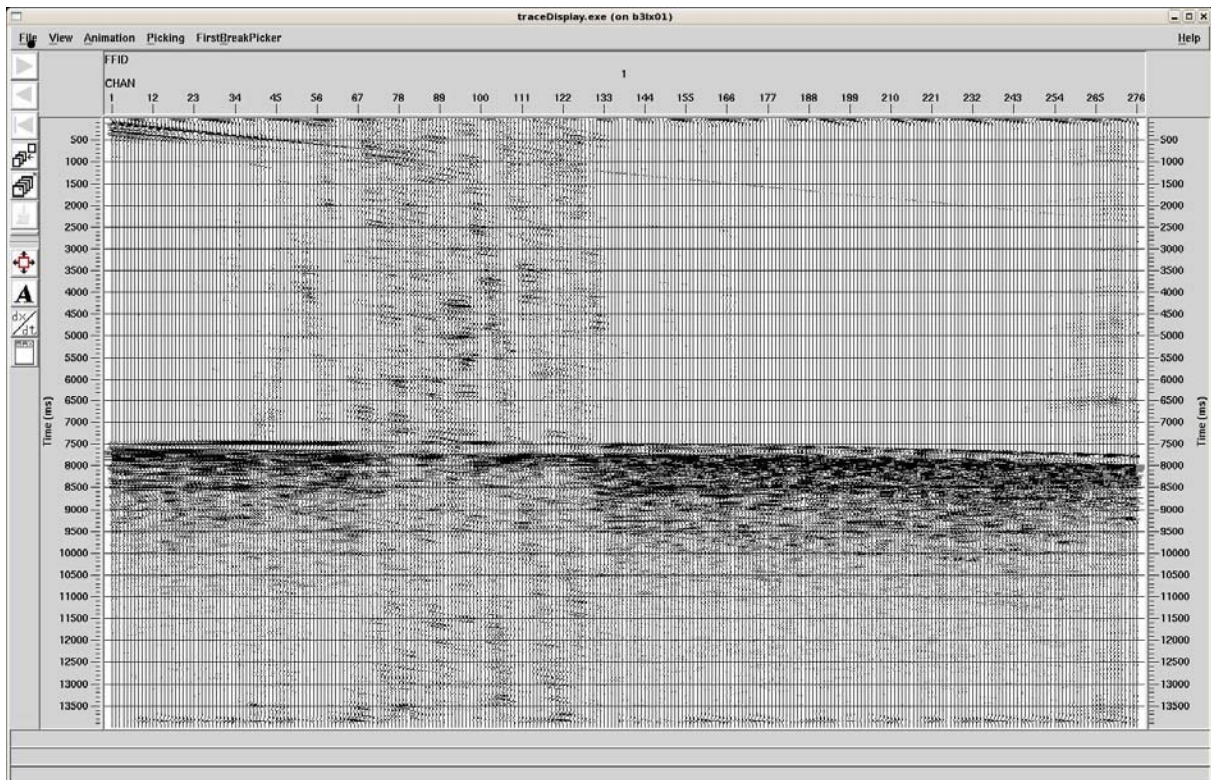


Fig. 1.10.13: Example shot gather after dip scan stack. This process is very time-consuming and thus was rarely applied.

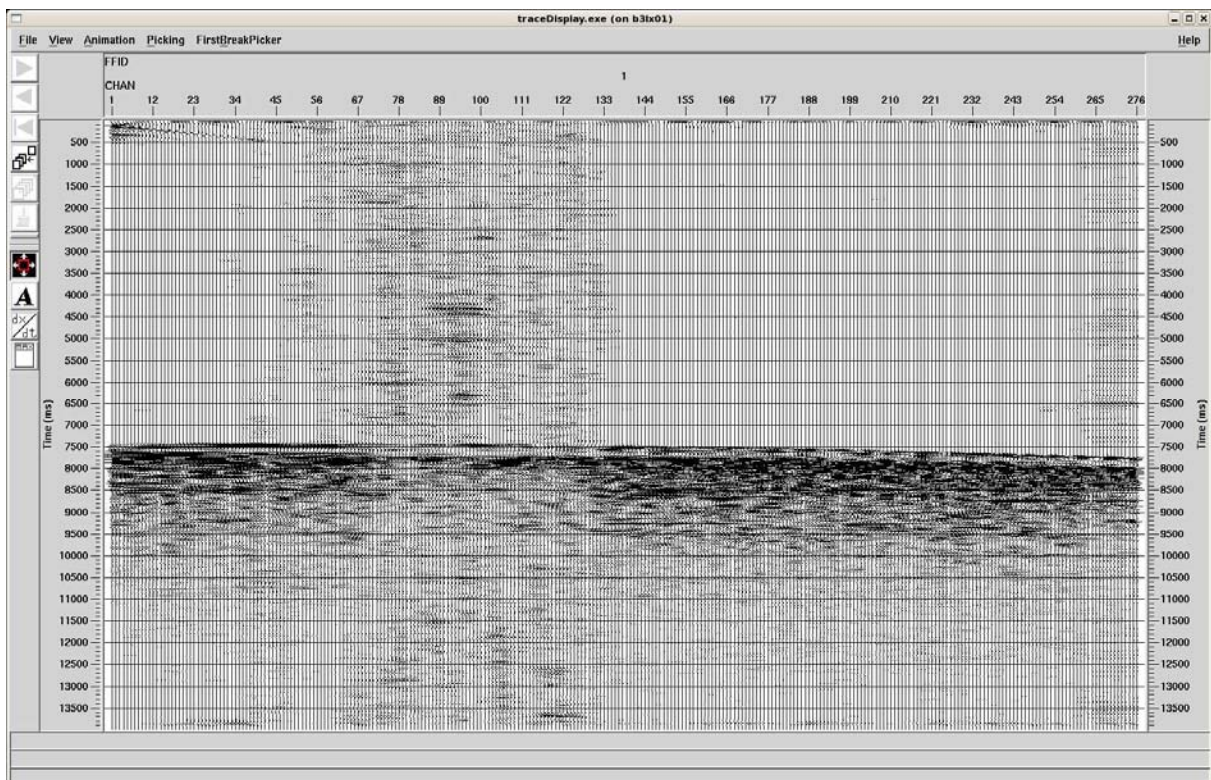


Fig. 1.10.14: Example shot gather after prestack processing (full spectrum preserved).

Velocity analysis

Velocities were picked at regular 6 km or 3 km intervals (480 CDPs / 240 CDPs) along the lines, using one of ProMAX's on-screen interactive velocity picking utilities. The ProMAX velocity picking module included a semblance display with an interval velocity graph, a CDP supergather which could have NMO applied instantly, a series of constant velocity stack panels, and a dynamic stack panel. For improving the signal to noise ratio, supergathers were formed by combining 5 adjacent CDP gathers, and these CDP gathers also made up the stack panels. A Spherical Divergence Correction with synthetic velocities was applied to the supergathers.

To speed up the on-screen velocity picking procedure, the velocity analysis displays were pre-computed. When primary velocities were clearly defined, they were normally picked from the semblance display, and Normal Moveout was applied to the gather to check that the events were lining up well. Velocities were also be picked from the constant velocity stacks whenever the velocities were poorly defined on the Semblance display.

After velocity picking, velocities were viewed and quality-controlled on screen using the ProMAX velocity viewer module. This module was most useful for editing any unreasonable velocity picks and finally to smooth the velocity field for the further processing.

Stack

An amplitude recovery has been applied to compensate for spherical divergence ($1/(\text{time} \cdot \text{vel}^2)$) prior to stacking. The CDP gathers were NMO corrected. After stacking the traces in the CDP gathers, the stacked section was written to disk. A test of different amplitude calculations showed similar results. Only the Exclude Min-Max option was occasionally used to exclude partly noisy traces in a gather.

Post-stack time migration

A rough oceanic basement, characterized by numerous and strong diffraction hyperbolas was prominent in the stacked section. In order to enable sufficient interpretation, a post stack time migration was applied. Tests resolved a Phase Shift migration to be most efficient. A Kirchhoff Migration somehow smeared reflections beneath the top oceanic crust reflector. The Phase Shift Migration incorporated a multiprocessor tool, dips were migrated up to 90%, and the desired frequency range defined (Fig. 1.10.15 to Fig. 1.10.17). To avoid migration artifacts the default tapering was occasionally changed to Bottom Taper 500, Upper edge taper 10, and Lower edge taper 120.

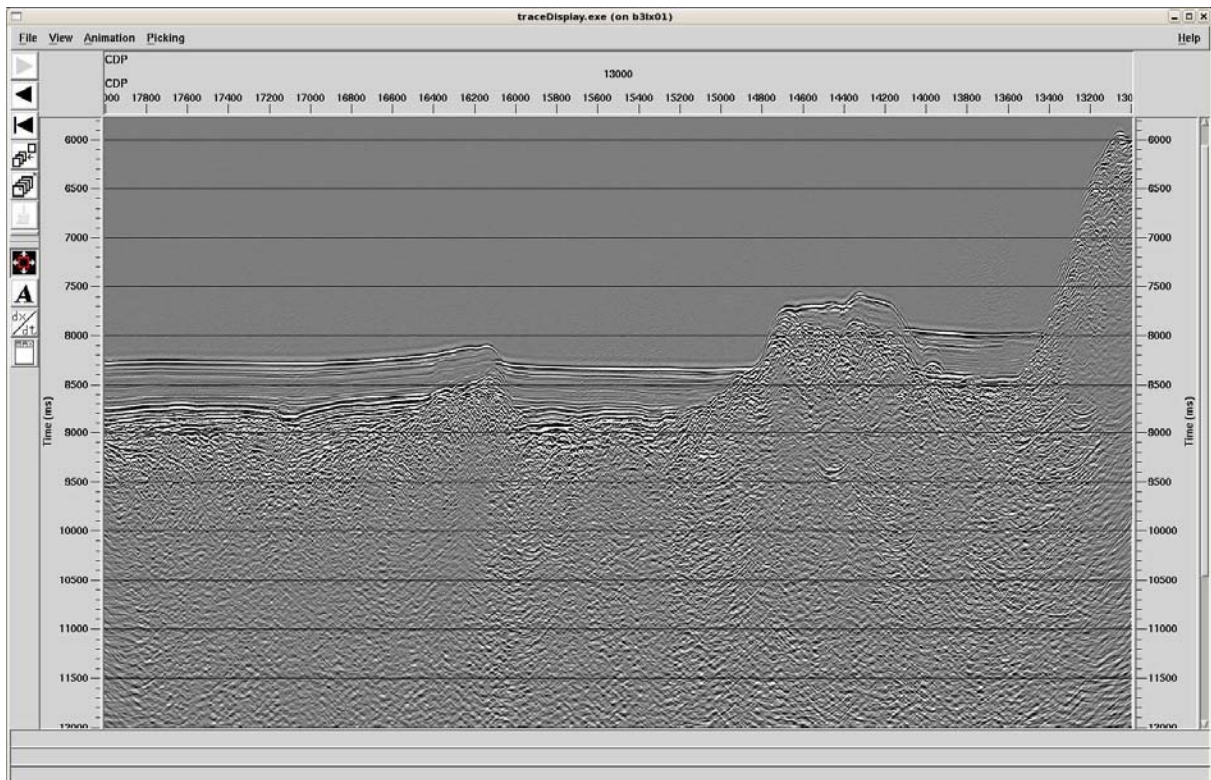


Fig. 1.10.15: Example of post-stack Kirchhoff-migrated section

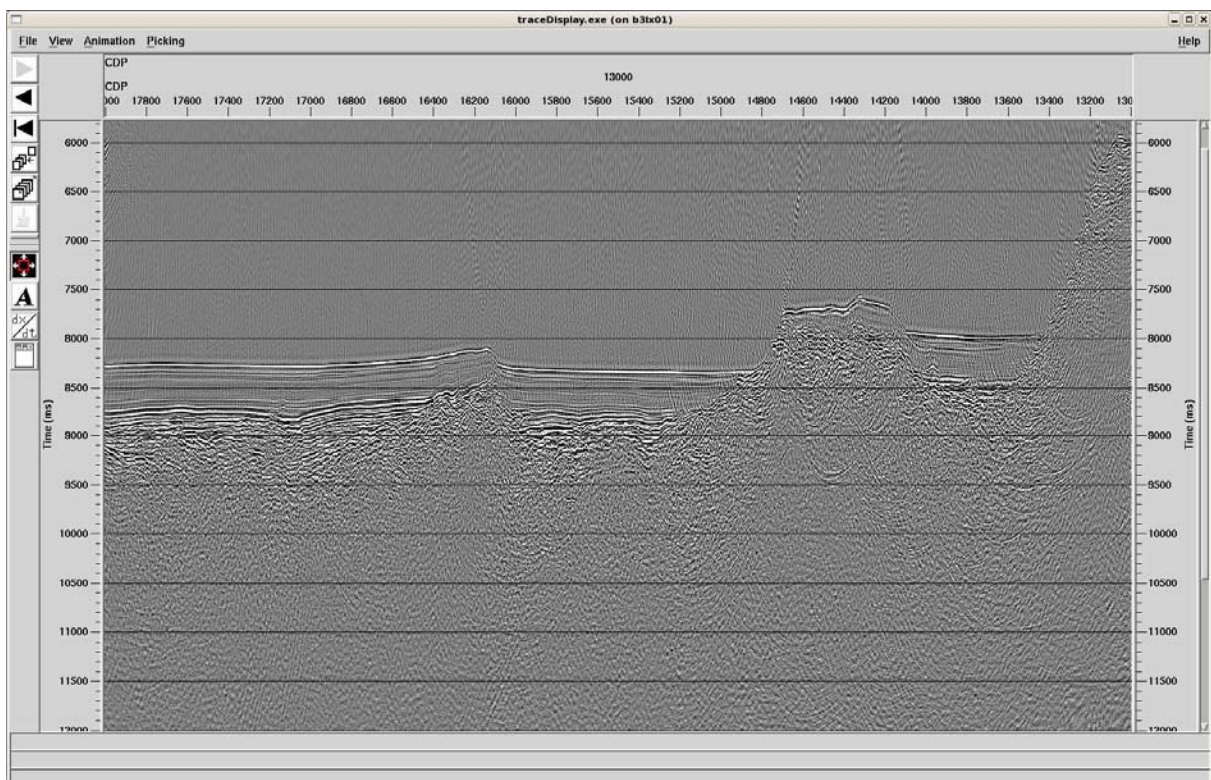


Fig. 1.10.16: Example of post-stack Stolt-migrated section

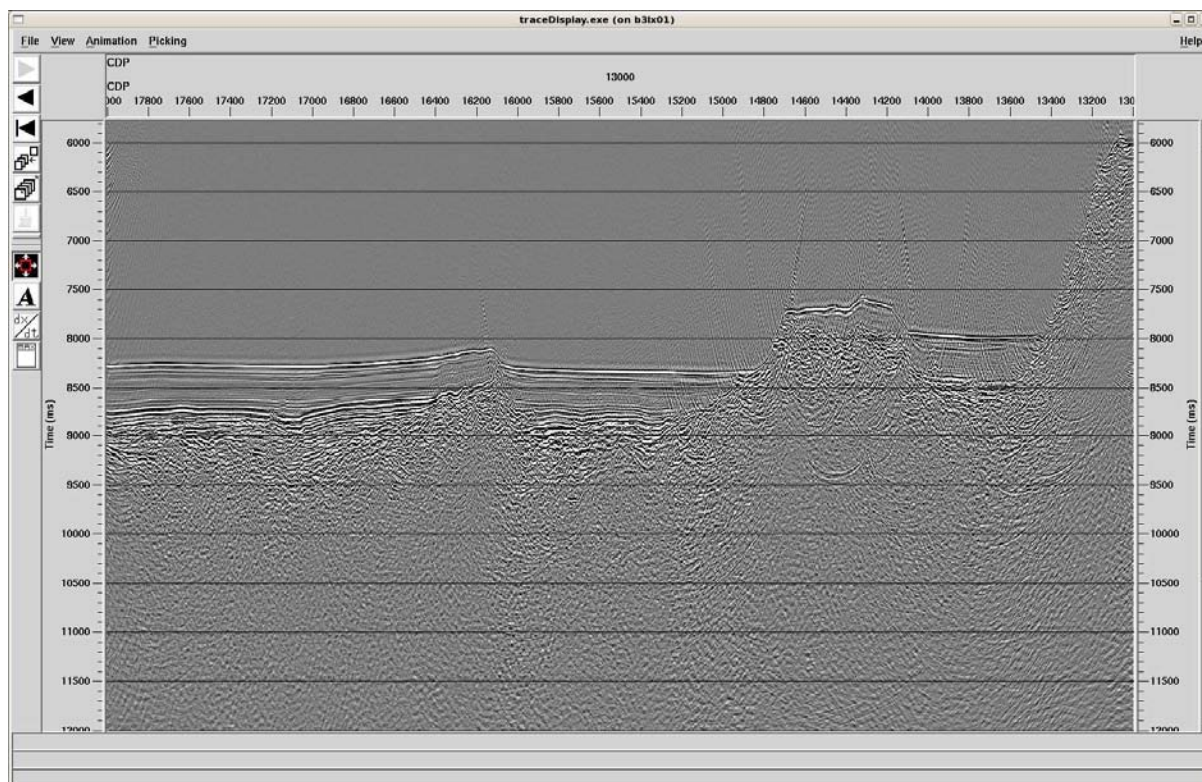


Fig. 1.10.17: Example of a post-stack phase shift migrated section

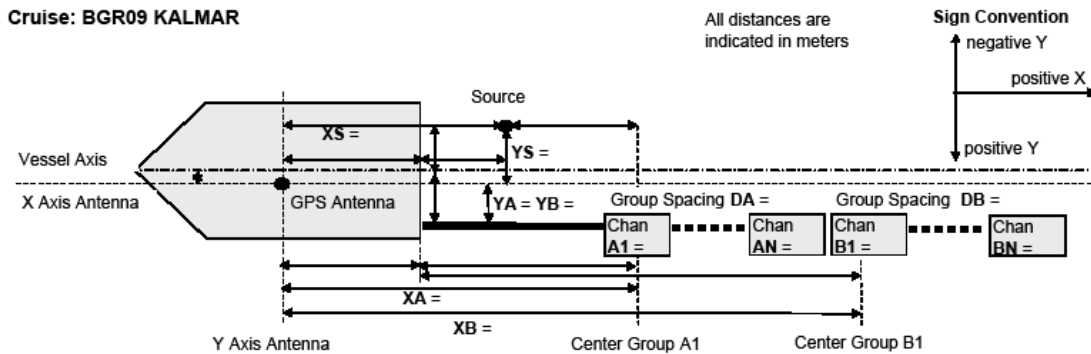
Output to SEG-Y files

For interpretation on the GEOQUEST system, the post-stack sections were written to disk in SEG-Y format. The time-migrated sections have also been exported. The SEG-Y EBCDIC header was generated automatically by ProMAX. The x and y coordinates of the energy source point were written to the standard byte locations 73-80 of the trace header. The x and y coordinates of the CDP positions were written to the standard byte locations 181-188 of the trace header. Surface Wave Noise Attenuation with water velocity was used to clean the data.

Tab. 1.10.2: Onboard processing overview.

Line	SP	CMP	Stack	Migration	Remarks
BGR09-101	1-11316	9856-55433	X	X	
BGR09-102	1-950	9856-13809	X	X	
BGR09-102a	1-1648	9856-16565	X	X	
BGR09-103	1-6243	9856-35003	X	X	
BGR09-104	1-1111	9856-14487	X	X	
BGR09-105	1-7050	9856-38179	X	X	
BGR09-106	4-3033	9856-22085	X	X	FFID 1-3030
BGR09-107	1-5500	9856-32135	X	X	
BGR09-108	1-1000	9856-14004	X	X	
BGR09-109	1-3030	9856-22149	X	X	
BGR09-110	1-1524	9856-16073	X	X	combined processed

BGR09-110a	1-300	9856-11207	X	X	with 110a
BGR09-111	2-2999	9860-21981	X	X	FFID 1-2999
BGR09-112					



Patterns Spreadsheet for 2D Marine Geometry Assignment in ProMAX from line 101 to 112

Mark Block	Min Chan	Max Chan	Chan Inc	Src Pattern	Grp Int	X Offset	Y Offset
1	A1=1	AN = 276	1		DA = 12.5	XA = 261.4	YA = -2.2
2	B1=	BN=			DB =	XB =	YB =
3							
M							
M+1				1 ^{*)}		XS = 108.9	YS = -2.2
...							

^{*)} -1 if A1 > AN, 1 if A1 < AN ^{**)} The Src Pattern numbers has to be indicated in the SIN Ordered Parameter File

↑ Streamer Patterns
 ↓ Source Patterns

Fig. 1.10.18: Summary of the acquisition geometry.

1.10.5 Multichannel seismic interpretation

R. Lutz, H. Thöle

Seismic interpretation was performed on a Dell Precision 670 workstation equipped with 4 GB RAM, two 500 GB hard disks and two 30" TFT monitors (Fig. 1.10.19). An uninterruptable power supply (UPS) was connected between the onboard electric power supply and the workstation to avoid power failures. An external hard disk was used for backups.

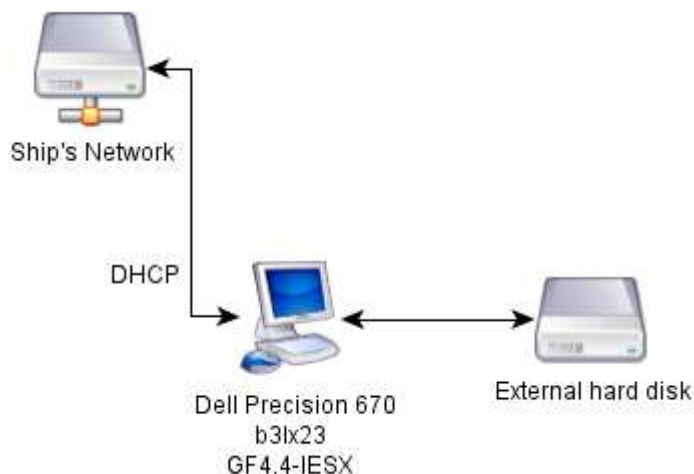


Fig. 1.10.19: Computer equipment for seismic data interpretation.

Geoframe IESX 4.4 (gf4c4_20) was used for interpretation and seismic data were loaded from segy files. Navigation data were provided in the segy trace headers (cdp_x and cdp_y at bytes 181 and 185, respectively). Shot point (SP) numbers were loaded from byte 5 of the segy trace headers as consecutive numbers. Thus, the CDP locations rather than the SPs should be used for positioning. Positions in the segy headers of the MCS data are given in UTM coordinates in zone 59, northern hemisphere (Fig. 1.10.20).

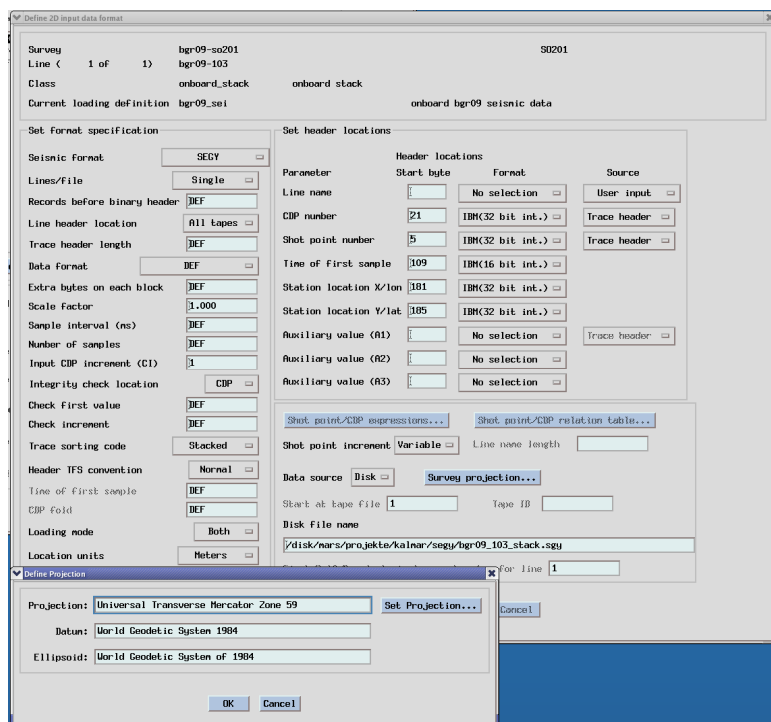


Fig. 1.10.20: Loading definition for MCS data into IESX.

The geoframe project used UTM 58 N, WGS 84 as Display/Storage coordinate system. Two different versions of each MCS profile were provided by the processing team, these are: onboard_stack and onboard_mig. The unprocessed Parasound data were loaded as seismic class parasound_81 for all MCS profiles and all magnetic profiles (BRG09-M01, -M02, BGR09-M10) (Fig. 1.10.21).

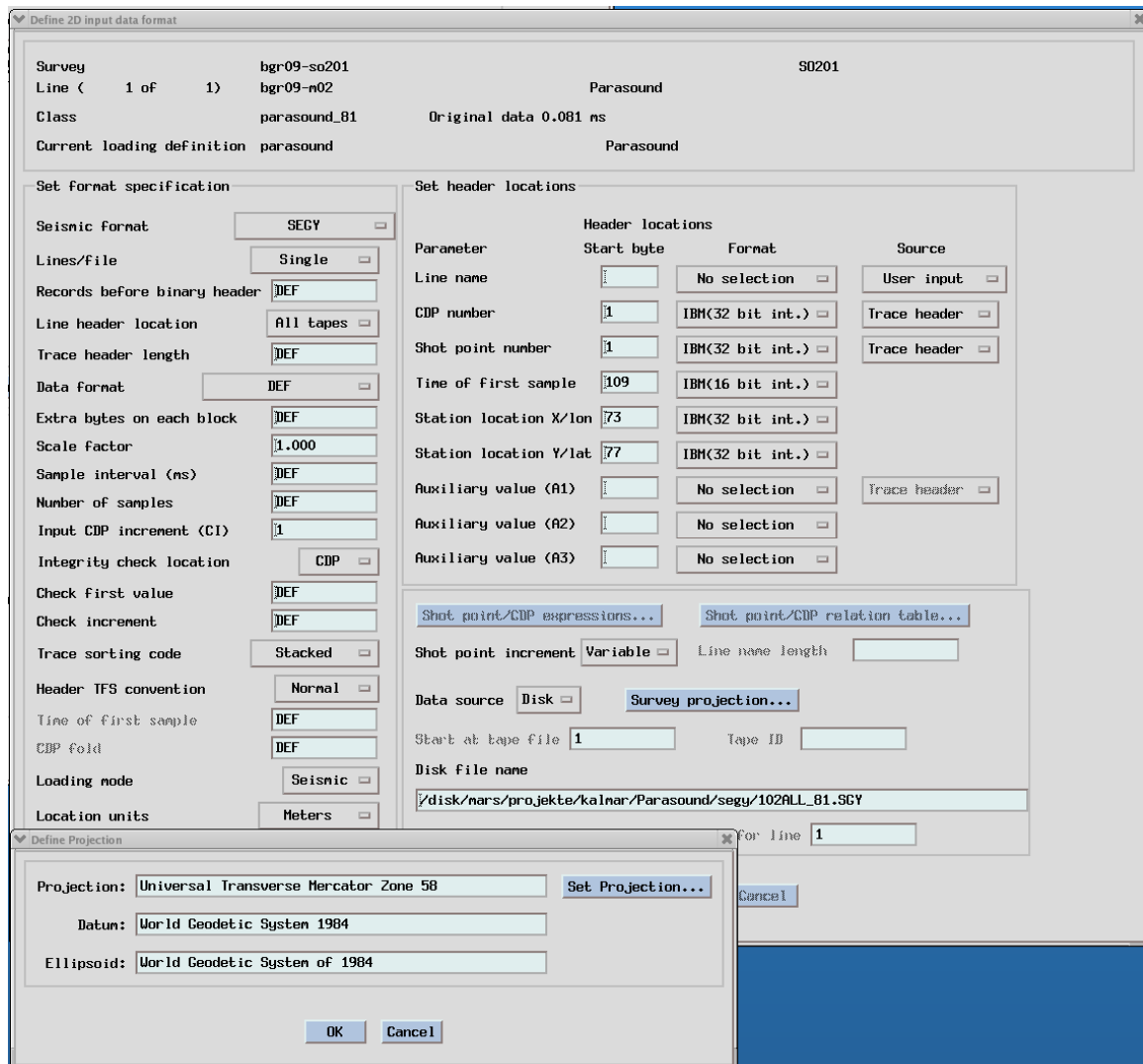


Fig. 1.10.21: Loading definition for Parasound data into IESX.

1.11 Magnetic data acquisition and processing

U. Barckhausen, H.-O. Bargeloh, M. Zeibig

The BGR magnetometer array used during cruise SO-201 KALMAR consisted of two independent magnetometer types which can be operated simultaneously on one cable (Fig. 1.11.1 and Fig. 1.11.3; TTab. 1.11.1):

- (1) the SeaSpy gradiometer system with two Overhauser magnetometer sensors and
- (2) one oriented Magson fluxgate sensor.

Overhauser sensors measure the scalar absolute value of the total magnetic field while fluxgate magnetometers measure the magnetic field vector in its three components.

1.11.1 Marine Magnetism SeaSpy™ Gradiometer

The SeaSpy™ Marine Gradiometer System manufactured by Marine Magnetism Corp. consists of two proton precession magnetometers, enhanced with the Overhauser effect. Two exactly equivalent magnetometers are towed 150 meters apart as a longitudinal array about 700 meters astern of the ship, where the ship's magnetic field is already decayed well below 1 nT. Both sensors measure the total intensity of the magnetic field simultaneously. The difference between the two measurements is an approximation for the longitudinal gradient of the field in the direction of the profile line. Provided that the time variations are spatially constant over the sensor spacing, the differences are free from temporal variations and their integration restores the variation-free total intensity or magnetic anomaly (apart from a constant value).

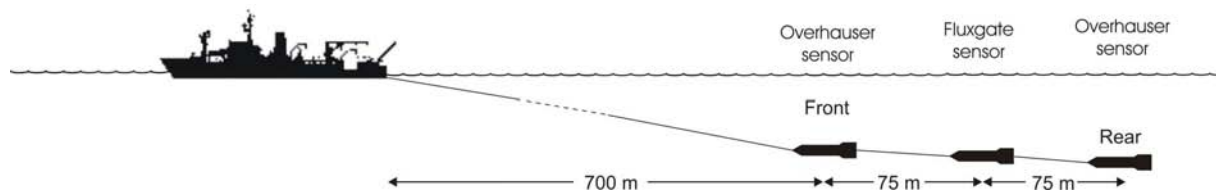


Fig. 1.11.1: Schematic sketch of the setup used during cruise SO 201, Leg 1a, consisting of a towed gradiometer system (front and rear Overhauser sensor) and one fluxgate towfish in-between.

A standard proton precession magnetometer uses a strong DC magnetic field to polarise itself before a reading can be taken. Overhauser sensors work similar to proton magnetometers with the exception that the proton spin excitation (polarisation) is produced by radio waves, which excite the spin of the electrons in an organic fluid within the sensors. Then the electrons transfer their spin to the protons in the fluid via a quantum mechanical process called Overhauser effect. Similar to other proton magnetometers, the relaxation frequency of the protons is a measure for the magnitude of the ambient magnetic field. However, the polarisation power required is much smaller and the AC field may be left active while the sensor is producing a valid output signal. This allows the sensor to cycle much faster and to produce more precise results than a standard sensor. The signal is digitized by the electronics assembly within the tow fishes, which then transmits the digital data strings via a two-conductor tow cable to the vessel. The tow cable is connected to a deck leader, which is in turn connected to the power supply and the logging computer. As configured for this survey, the Overhauser sensors had a cycle time of one second. The sensors are specified with a noise level of $0.01 \text{ nT}/\sqrt{\text{Hz}}$, a resolution of 0.001 nT , and an absolute accuracy of 0.2 nT .

The SeaSpy™ magnetometer system was operated in 'gradient mode' using both sensors during the whole cruise. The instrument was powered by two car-batteries avoiding grounding problems and providing 24 V. The batteries were recharged during operations. The smart transceiver within the electronics unit provided the cable voltage of 70 V and was protected against overheating by a ventilation fan. The current strength was displayed continuously. It allows an online diagnosis of the magnetometer array. Each Overhauser sensor consumes 45 mA and the fluxgate 35 mA and, if the current strength is below the expected sum, this indicates sensor failure or connector problems.

1.11.2 Magson™ Fluxgate Magnetometer

The Magson fluxgate magnetometer was designed at BGR and built by the Magson Company in Berlin. The first sensor was built in 2004 and modified in 2005, a second sensor was built in 2006 as a slightly modified copy of the first sensor.

The system consists of i) a digital 3-axis Magson fluxgate magnetometer yielding excellent precision, ii) a two-axis tilt-meter, type 900H made by Applied Geomechanics Ltd., iii) a two-axis and single axis accelerometer, types ADXL203 and ADXL103 made by Analog Devices, iv) sensors for temperature, pressure, and humidity, and v) a data acquisition microprocessor unit built by Magson. Fluxgate and inclinometers are mounted on a common platform. All components, shown in Fig. 2.2, are placed inside a pressurized glass-fibre tube of the same brand as the sensors of our standard SeaSpy™ gradiometer (Fig. 1.11.2).

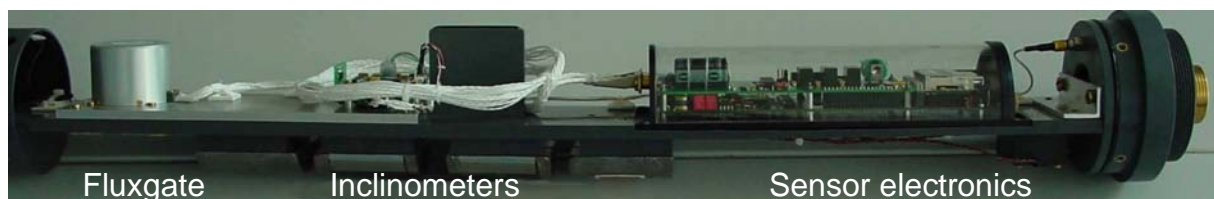


Fig. 1.11.2: Components inside the fluxgate magnetometer towfish.

The Magson fluxgate uses the principle of vector-compensating the three ring-core-sensors by means of three independent Helmholtz coils. The internal feedback circuit, using digitally controlled DC-currents fed into the Helmholtz coils maintains precise nulling of the field inside the ring-core. Thus the amplitude of this current can be used as a signal to measure the vector components of the magnetic field. A scalar fluxgate calibration is required to provide offset, scale factor and non-orthogonality angle for each axis. All electronic components are integrated on the board of the data acquisition microprocessor. Fluxgate magnetometers with digitally compensated ring-core-sensors maintain a considerably higher accuracy over non-compensated instruments. In addition, they yield higher stability over time and temperature. The Magson fluxgate sensor is specified with a noise level of $0.02 \text{ nT}/\sqrt{\text{Hz}}$, a resolution of 0.008 nT and a long term stability $< 10 \text{ nT/year}$.

Inside the towfish, a special platform is used to mount the fluxgate and both tilt-sensors (Fig. 1.11.2). The first tilt-sensor by Applied Geomechanics (900H) measures pitch and roll angles by a conductive liquid in a half-filled glass vial. The tilt angle is derived by the height of liquid covering five electrodes. The angular range covers a span of $\pm 25^\circ \pm 40^\circ$ (first/second Magson towfish) with an accuracy of about 0.01° of arc (noise level 0.005°). The second type of tilt-sensors are dual axis accelerometers by Analog Devices (ADXL203), measuring pitch and roll angles over a span of $\pm 50^\circ \pm 20^\circ$ (first/second Magson towfish) resolving 0.05° of arc (noise level 0.095°). A third accelerometer for the vertical axis (ADXL103) allows detecting unintended towfish positions beyond the inclinometer range. The accuracy of the Applied Geomechanics sensor is significantly higher, but the calibration function is non-linear and temperature-dependent. The Analog Devices sensor has a faster response (cross correlation indicated a 0.1 s difference), the calibration function is linear and almost temperature-independent, but it suffers a higher noise level increased by a factor of two. Both tiltmeters measure not only the static acceleration, which would provide the needed true roll and pitch angles. Instead, they principally

measure dynamic accelerations due to the linear and angular accelerations of the continuously moving towfishes. This source of error can be reduced by filtering.

A high precision of the measured tilt angle is necessary to rotate the field components from the sensor's coordinate system of the moving fluxgate towfish into the geomagnetic coordinate system. By rotation about the Euler angles the vertical and horizontal vector components are obtained. The accuracy of the vector data is limited by the accuracy of the rotation angles. For example, a 0.01° tilt deviation may result in 7 nT component error in the survey area. Without any yaw angle estimation, the orientation of the horizontal field vector (i.e. the north and east components), remains unknown. A crude first approximation is given by the ship's course. Utilising magnetic heading from the fluxgates themselves (compass yaw), removes seafloor anomalies by default; however, a numerical yaw approximation separating seafloor anomalies from towfish movements in water by wavelength filtering has been introduced by Engels et al. (2008).

An embedded microprocessor with a flash disc is used to store all fluxgate and tilt-meter readings. The storage capacity of 1 GB is sufficient to allow 11 days of continuous operation at the selected sampling rate of 10 Hz.

1.11.3 Fluxgate Calibration

A fluxgate magnetometer has to be calibrated regularly against a precisely known reference field in order to estimate the calibration parameters. These parameters are offset, scale factor, and non-orthogonality angle for each axis - thus a total of nine parameters for a three-axis vector magnetometer. During a scalar calibration, the fluxgate sensor is rotated around all axes and the total field reading is adjusted to the reference field. This optimization of calibration parameters is done by a least squares fit of the measurements (here: downhill simplex method; one variant keeping the non-orthogonality angles fixed, which are regarded stable; codes by Jeff Gee, SIO). By this procedure, one combination of calibration parameters is obtained which minimizes deviations from the reference field for all attitudes of the sensor.

Calibration parameters drift slowly with time and changes may also occur after long-distance transportation to different latitudes. Furthermore, calibration parameters are temperature-dependent, which means that laboratory calibrations have to be repeated at different temperatures. In addition to a laboratory calibration, where the sensor is rotated around all axes at different temperatures, a calibration figure cruise is required in the survey area waters. The latter provides a fine adjustment to the local magnetic field conditions and water temperatures. Therefore, calibration parameters should be estimated at the beginning and end of each survey in order to account for a possible drift.

1.11.4 Magnetic data processing

The magnetic raw data recorded by the Overhauser and fluxgate magnetometers were processed during the cruise in time domain in order to obtain high quality magnetic data which are essential for further post-cruise data analyses. Onboard processing of the total magnetic field gradients resulted in reconstructed variation free total field anomalies (F-anomalies). Single sensor fluxgate data additionally

provide anomalies in components (e.g. Z-anomaly) which may contain a variation contribution. Observed anomalies are compared to synthetic seafloor anomalies derived from forward 2D modeling of magnetic reversal time scales that allow crustal age dating.

Onboard processing scheme

The standard processing of the gradiometer data was based on the BGR code PROFILMAG by Eilers et al. (1994). In this processing method, raw data from the gradiometer system enter the anomaly reconstruction algorithm directly. In addition to a basic summing-up option two sophisticated reconstruction algorithms in the frequency and the wave number domain are available.

The task to process magnetic fluxgate component data was taken as an opportunity to set up a new generalized processing scheme which will work for vector component data as well as for the scalar magnetic field. The concept is to pre-process raw data in time domain in a comprehensive straight-forward and transparent way before gradiometer anomaly reconstruction and further component analysis. The key element of this processing scheme is a band pass (BP) filter which reduces the data to wavelengths which can be attributed to anomalies originating from crustal sources. The codes were developed during cruise SO 180 (2004) when the Magson fluxgate magnetometer was operated for the first time and they have been extended in the meantime. In the following the current status of the upgraded processing codes (version 8) is summarized briefly:

1. Code READMAG reads all data formats from the individual sensors and the ship's GPS recordings. Gaps, erroneous data records and unphysical data exceeding certain reliability thresholds are replaced by dummy values. From GPS positions which are smoothed by a running mean, control parameters like waypath kilometer, velocity, and azimuth are derived for each sample and are accepted as having reasonable values. The time delay of each sensor according to its position behind the vessel and the ship's velocity is taken into account. Clock deviations (shift and drift) of the individual instruments are being corrected. Fluxgate raw data are calibrated firstly by the laboratory scalar calibration parameters (including temperature calibration) and secondly by the results from the in water calibration cruise. Tiltmeter angles are calibrated as well. Vector component data are obtained by coordinate transformation into the geographic coordinate system by rotation of the Euler angles. The magnetic heading of the fluxgates is used as a first approximation of the geomagnetic yaw angle. The same output format is also used for the following codes which consist of a common header and an individual instrument dependent data part (one record per sample).
2. Code INTERMAG interpolates all data gaps marked by dummy values either linear or by cubic splines. In order to despise and resample the scattered raw data, a median filter provides a robust mean. All data which were recorded at different sampling rates are decimated to equidistant 50 m samples, the window length of the median filter. For gradiometer data, the median applies to the differences in order to preserve simultaneous measurements of the rear and front sensor.
3. Code IGRFMAG subtracts the ambient main field using IGRF model 2005 (Maus et al., 2005) up to degree and order 13 (195 coefficients) with secular variation prediction (80 coefficients). For vector data, from the dot product projection of the

measured total field into the IGRF direction the absolute value of the IGRF is subtracted. The IGRF subtraction is done for each gradiometer sensor individually in order to remove the main field gradient. From the vector components the IGRF components are subtracted directly. Optionally a band pass filtered numerical yaw angle can be subtracted from the fluxgates' magnetic heading before IGRF subtraction in order to eliminate yaw angles due to water currents and to pass yaw angles due to magnetic anomalies.

4. Code FILTMAG applies a BP filter in the time domain in order to limit purely on wavelengths related to realistic anomalies originating from crustal sources. Reversal time scales and spreading rate estimates relevant for the survey area and the data itself allow an estimation of wavelengths which can be expected to originate from seafloor spreading anomalies. Alternatively, the relevant wavelength range can be derived from spectral analysis. Here, wavelengths shorter 2-4 km are removed by the low pass (LP) filter and eliminate the high frequency scattering due to orientation errors, e.g. misleading tilts by towfish dynamics. For long profiles, the high pass (HP) filter gently cuts wavelengths longer 250 km and removes long period trends, fluxgate and gradiometer baseline instabilities, and even partly external geomagnetic variations. Schmucker's (1978) optimized trapezoidal time domain filter was applied, using a steeper slope (higher filter quality) for the LP cut-off wavelength and a gentle slope for the HP cut-off wavelength. At the beginning and end of each profile profile boundaries are wrapped at both ends to allow all recursive filter coefficients to be defined without a loss of data.

5. Code GRADMAG sums up total field differences between either Overhauser sensors or other arbitrary sensor pairs. The differences are obtained either from the LP-filtered data for short profiles or band pass filtered data for long profiles. For two sensors which are operating simultaneously in gradiometer mode, temporal external variations are constant over a small horizontal spacing. Consequently, taking differences of simultaneous readings approximates the small gradient of crustal anomalies with values often below one nT per 150 m. Summing up these small differences ('integrating the gradient') and correcting for the off-axis gradient reconstructs the stationary internal anomaly – free of external geomagnetic variations. However, the absolute level gets principally lost (unknown integration constant). Any constant offset between both sensors and any linear trend of the anomalous field is removed by subtracting the mean of all gradiometer differences. Consequently, anomaly profiles start and end centered at the baseline. Subtracting the trend obtained by linear regression of the reconstructed anomaly and adding the trend obtained by linear regression of the LP-filtered curve helps to preserve the absolute anomaly level. In case of crosspoints a manual leveling was performed. A detailed crosspoint analysis including other BGR cruise data has to be performed after the cruise.

The whole recording period of a sensor in water is called here a section. Section processing can be performed for all codes before filtering (IGRFMAG for fluxgate data, FILTMAG for gradiometer data). Individual profile processing is required for FILTMAG and GRADMAG, because we observe an azimuth dependence of the Overhauser and fluxgate sensor. Gradiometer differences show different baseline levels in the order of one nT for different profile azimuths, which might be due to small magnetic contaminations in the sensor (e.g. in copper wires). Fluxgate baseline shifts are due to the non-perfect calibration.

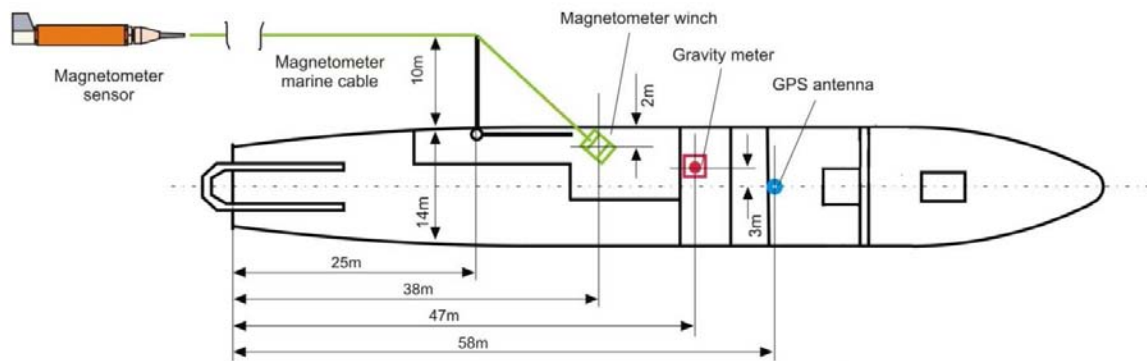


Fig. 1.11.3: Positions of magnetometer winch, outrigger port, GPS antenna, and Gravimeter on R/V Sonne.

Tab. 1.11.1: Magnetometer sensor and cable configurations applied during all cruise profiles and calibration loops.

Profiles	Sensors	Cables
BGR09-M01 through BGR09-112,	Overhauser 13141 (Front) Magson 13142 Overhauser 13139 (Rear)	800-1 75-6 AB 75-7 AB
Calibration-01, BGR09-M03	Overhauser 13140 (Front) Magson 13142 Overhauser 13335 (Rear)	800-1 75-6 AB 75-7 AB

1.12 Gravity

I. Heyde

1.12.1 The sea gravimeter system KSS31M

During cruise SO201-1a the BGR-owned sea gravimeter system KSS31M was installed in the gravimetry laboratory one level below the main deck. The sea gravimeter was located approximately at the vessel's nominal water line, 1.5 m to portside from the centerline, and 47 m forward of the stern.

The gravimeter system KSS31M is a high-performance instrument for marine gravity measurements, manufactured by Bodenseewerk Geosystem GmbH. While the sensor is based on the Askania type GSS3 sea gravimeter designed by Prof. Graf in the 60ties, the development of the horizontal platform and the corresponding electronic devices took place at Bodenseewerk Geosystem in the second half of the 70ties. The system was modernised and modified in 2001 by the successor company Bodensee Gravimeter Geosystem GmbH. The KSS31M system consists of two main assemblies: the gyro-stabilized platform with the gravity sensor and the data handling subsystem.

The gravity sensor GSS30 (Fig. 1.12.1) consists of a tube-shaped mass that is suspended on a metal spring and guided frictionless by 5 threads. It is non-astatized

and designed to be insensitive to horizontal accelerations. This is achieved by limiting the motion of the mass to the vertical direction. Thus it is a straight line gravity meter avoiding cross coupling effects of beam type gravity meters. The main part of the total gravity acceleration is compensated by the mechanical spring, but gravity changes are compensated and detected by an electromagnetic system. The displacement of the spring-mass assembly with respect to the outer casing of the instrument is measured using a capacitance transducer.

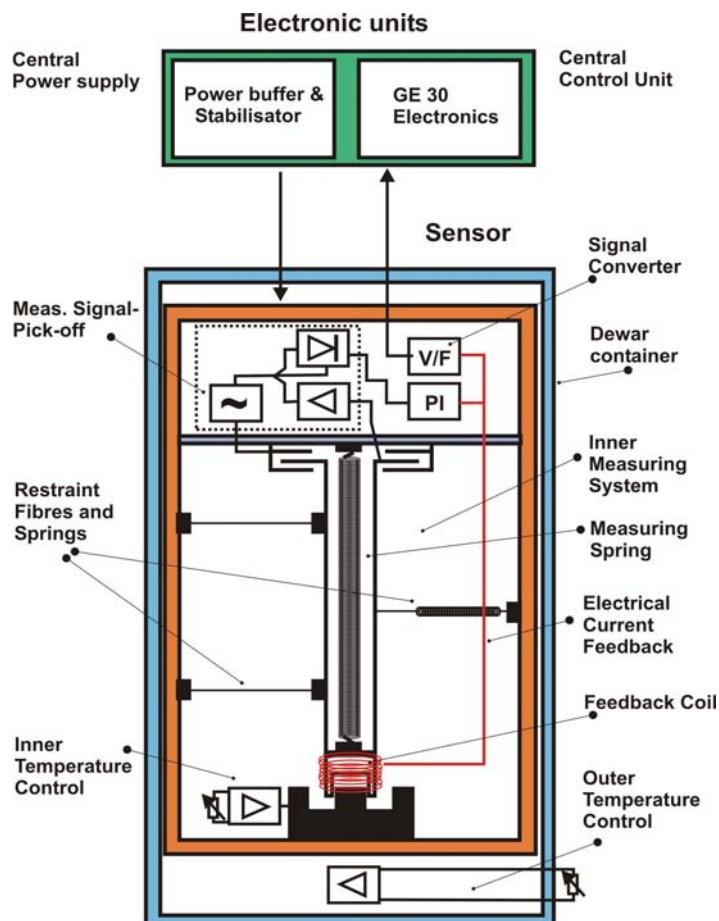


Fig. 1.12.1: Principle sketch of the gravity sensor GSS30 of the gravimeter system KSS31M

The leveling subsystem consists of a platform stabilised in two axes by a vertical, electrically erected gyro. The stabilisation during course changes can be improved by providing the system with online navigation data. The control electronics and the power supply of the platform are located in the data handling subsystem unit. Functions like gyro run-up and -down sequences and the automatic platform caging are performed by the system controller unit located in the data handling subsystem, too. The stabilised platform will keep the sensor in an upright position with an accuracy of leveling in the order of 0.5 minutes of arc. This is particularly important as the sensor is very sensitive to tilting. Vertical acceleration, however, cannot be eliminated. Luckily on a ship the vertical acceleration oscillates periodically with a period of some seconds. This signal can be eliminated easily by means of lowpass filtering.

The data are transmitted to the data acquisition and processing system in the dry lab and online navigation data from this system are sent with a rate of 1 Hz to support the stabilising platform. The support is realised as follows: The horizontal position of the gyro-stabilised platform is controlled by two orthogonal horizontal

accelerometers. The platform is leveled in such a manner that the horizontal accelerations are zero. If the ship describes a curve, the additional horizontal acceleration will cause the platform to be leveled according to the resulting apparent vertical axis. This axis may differ substantially from the true vertical axis and will result in reduced gravity values and additionally in an effect of horizontal accelerations on the measured gravity. The latter effect is eliminated by supplying the system with online navigation data. A microprocessor calculates the leveling errors from this input and enters them into the platform electronics which corrects the platform accordingly.

1.12.2 Gravity ties to land stations

To compare the results of different gravity surveys the measured data have to be tied to a world-wide accepted reference system. This system is represented by the International Gravity Standardization Net IGSN71 (MORELLI, 1974). The IGSN71 was established in 1971 by the International Union of Geodesy and Geophysics (IUGG) as a set of world-wide distributed locations with known absolute gravity values better than a few tenths of mGal. According to the recommendations of the IUGG, every gravity survey, marine or land, should be related to the datum and to the scale of the IGSN71.

Therefore, gravity measurements on land have to be carried out to connect the gravity measurements at sea with the IGSN71. The marine geophysical group of BGR uses a LaCoste&Romberg gravity meter, model G, no. 480 (LCR G480) for the gravity connections.

We contacted the Geographical Survey Institute of Japan (GSI) concerning point descriptions and absolute gravity values of reference IGSN71 stations. Unfortunately, no IGSN71 reference stations exist or are available around Yokohama. The closest station of the JGSN75 gravity network based on IGSN71 is in Aburatsubo (ABU) near the tide observatory of GSI about 50 km southwest of Yokohama.

R/V SONNE moored at the Yamashita pier No. 3 in the harbour of Yokohama (Fig. 6.5.2). On May 17, tie measurements to point A on the pier opposite the gravimetry laboratory on R/V SONNE have been made. Point A is located near bollard 570 m about 80 m from the northeastern end of the pier. The connection measurements resulted in an average absolute gravity value of 979742.46 mGal (with water level – 2.5 m, IGSN71) for point A at the water level. The reading of the KSS31 at departure time (May 17, 2009, 23:35 UTC) from the pier was –194.20 mGal.

Tab. 1.12.1: Observation report of the gravity tie measurements in Yokohama.

Station	Observer	Date	Time UTC	Reading units	Gravity value [mGal]
A	H	16.05.09	23:30	3318.35	3370.733
ABU	H	17.05.09	00:35	3350.62	3403.590
A	H	17.05.09	01:45	3318.35	3370.733
B	H	09.06.09	01:25	3318.14	3370.520
A	H	09.06.09	01:35	3318.00	3370.377
B	H	09.06.09	01:40	3318.14	3370.520

Observer: H = Heyde. Gravity in mGal was calculated using LCR G 480 scaling table.

Reference Stations:

ABU: Aburatsubo tide observatory

(35°09'34"N, 139°36'55"E, 4.733 m)

979774.65 mGal (IGSN71)

Gravity stations:

A: Yokohama harbour, Yamashita pier No. 3, Bollard 570 m, 80 m from the northeastern end of the pier

B: Yokohama harbour, Yamashita pier No. 3, Bollard 480 m, 170 m from the northeastern end of the pier

Differences between reference and gravity stations:

$$\mathbf{ABU - A} = +32.857 \text{ mGal}$$

$$\mathbf{B - A} = +0.143 \text{ mGal}$$

Absolute gravity at **A:** 979741.793 mGal

Absolute gravity for **A** (reduced to water level -2.5 m) 979742.460 mGal (IGSN71 system) used for the gravity tie on 17.05.2009 (23:35 UTC).

Reading of sea gravimeter KSS31 at that time: -194.20 mGal.

Absolute gravity at **B:** 979741.936 mGal

Absolute gravity for **B** (reduced to water level -3 m) 979742.736 mGal (IGSN71 system) used for the gravity tie on 09.06.2009 (01:45 UTC).

Reading of sea gravimeter KSS31 at that time: -195.17 mGal.

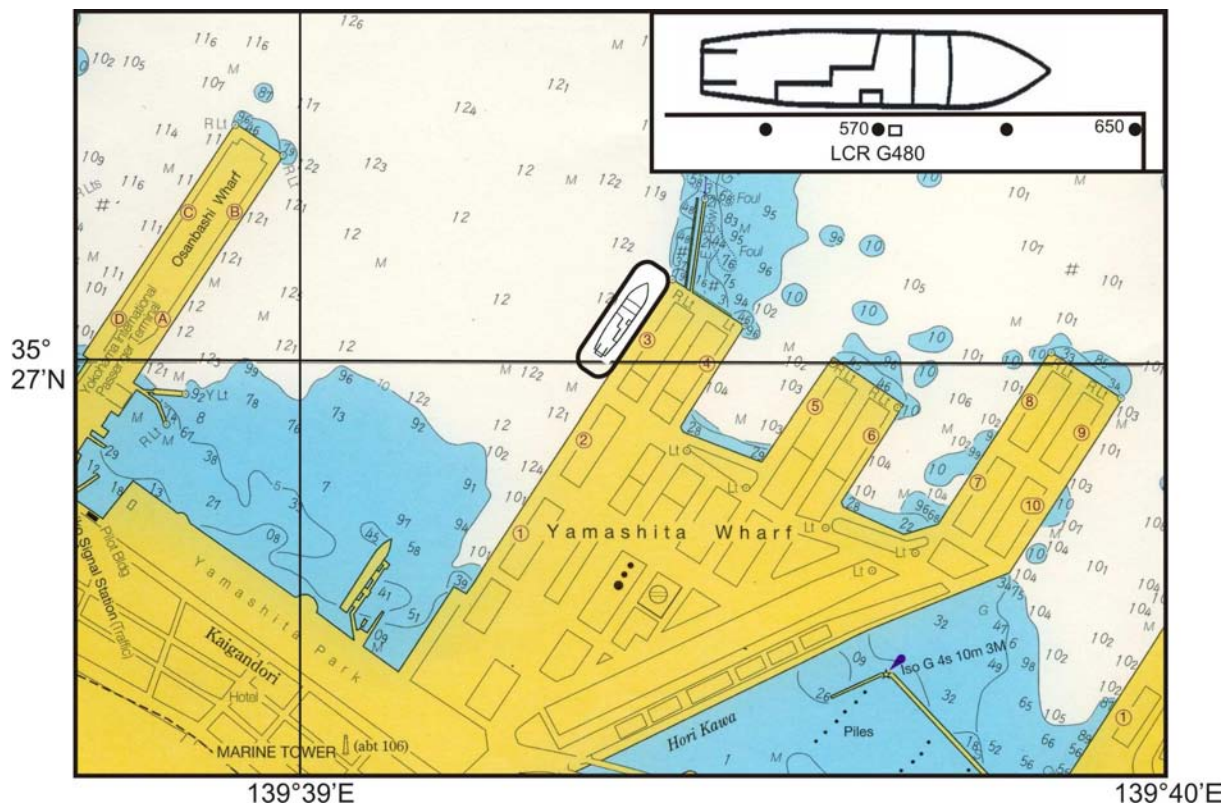


Fig. 1.12.1: Location of the mooring site of R/V SONNE at Yamashita pier no. 3 of Yokohama harbour (from the Japan Coast Guard chart JP66).

At the end of the cruise R/V SONNE moored at the Yamashita pier no. 3 in Yokohama near the bollard 470 m about 180 m from the northeastern end of the pier. On June 9, tie measurements to point **B** on the pier opposite the gravity laboratory on R/V SONNE have been made.

The connection measurements resulted in an average absolute gravity value of 979742.736 mGal (reduced to water level -3 m, IGSN71) for point **B**. It has to be taken into account however that the draught of R/V SONNE was about 0.25 m less than that the leaving time of Yokohama harbour. So the absolute gravity value for point **B** at the height of the KSS31M sensor was 979742.669 mGal. The reading of the KSS31 at the same time (June 9, 2009, 01:45 UTC) was -195.16 mGal.

The instrumental drift for cruise SO-201-1 can be derived from the readings in Yokohama to -1.169 mGal / 22.09 days or -0.053 mGal/day. This drift rate is rather small and lies within the normal drift range of marine gravity measurements with the KSS31M. Nevertheless, it will be applied to the data. On previous cruises, the drift of the instrument ranged from -1.44 mGal/month (SO-98, 1994) to $+1.1$ mGal/month (SO-122, 1997).

Marine gravity measurements were carried out from 18.05.09 (3:42 UTC) till 07.06.09 (6:16 UTC), i.e drift started with -0.009 mGal and ended with -1.075 mGal.

1.12.3 Gravity data processing

Processing of the gravity data consists essentially of the following steps:

- a time shift of 76 seconds due to the overcritical damping of the sensor,
- conversion of the output from reading units (r.u.) to mGal by applying a conversion factor
- of 0.94542 mGal/r.u.. On this cruise this was done in the system itself by hardware settings
- connection of the harbour gravity value to the world gravity net IGSN 71,
- correction for the Eötvös effect using the navigation data,
- correction for the instrumental drift (not performed until completion of the cruise),
- subtraction of the normal gravity (WGS67).

As a result, we get the so-called free-air anomaly (FAA) which in the case of marine gravity is simply the Eötvös-corrected, observed absolute gravity minus the normal gravity. According to the selectable time interval of the data acquisition system, gravity values are available every 20 seconds. These anomalies are named BEARB anomalies in the following.

The gravity anomalies, which are provided every second directly by the data handling subsystem of the KSS31M, were additionally recorded with a separate computer. Free-air gravity anomalies are obtained when the KSS31M is supplied with the necessary navigation data (geographical latitude and longitude, speed, course over ground and heading). These anomalies are available every second. The differences in both data sets are small. For the display and interpretation of gravity data the 20 s values were used. This interval is sufficient for ship-borne data and the 1 Hz data do not provide a higher resolution. However, outliers were removed manually in both data sets.

The BEARB anomalies show short-wavelength oscillations in the order of 1 mGal. These oscillations are suppressed in the KSS31M data (Fig. 1.12.2). The reason is that whereas the Eötvös correction values of the KSS31M are filtered the same way as the gravity data, the Eötvös correction values of BEARB are not filtered. The filtered free-air anomalies provided by the KSS31M were used for display and interpretation.

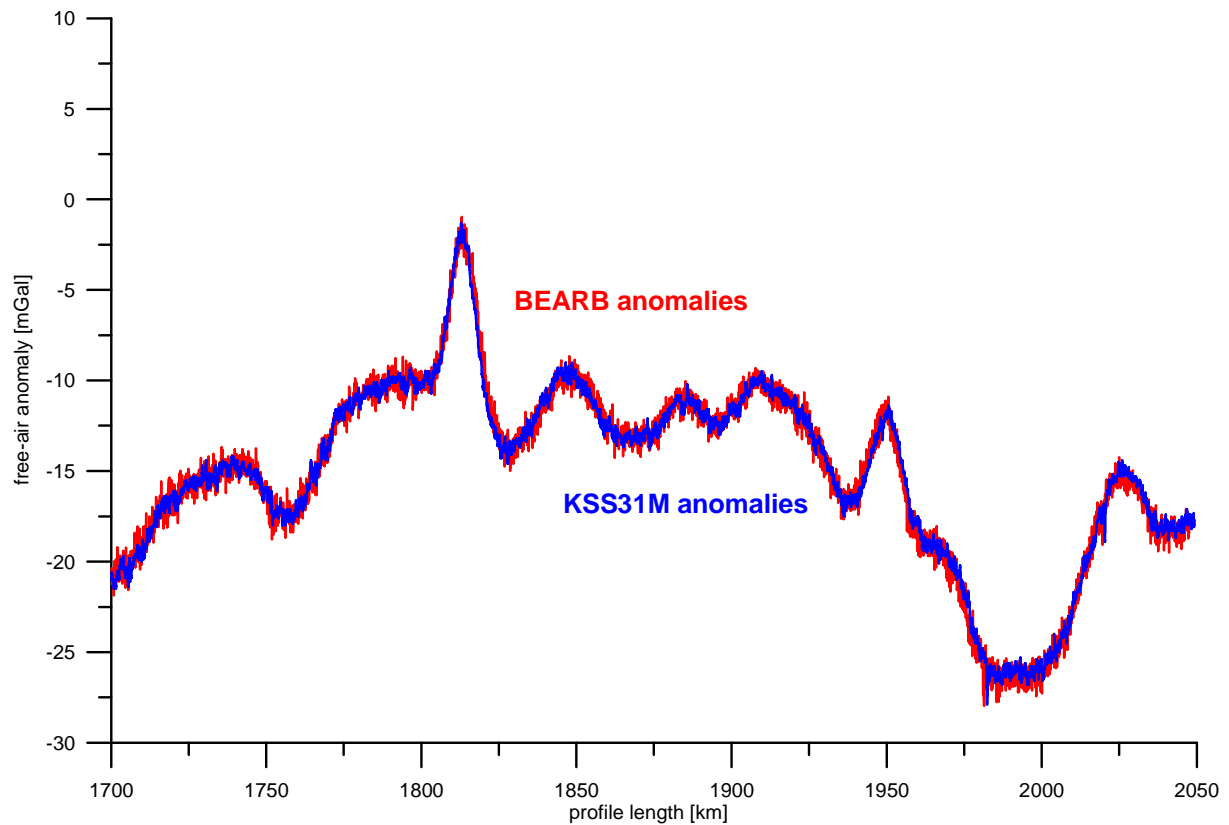


Fig. 1.12.2: Comparison of BEARB and KSS31M free-air gravity anomalies along a part of profile BGR09-M02 measured during medium to rough sea state conditions and a ship velocity of 12-13 knots.

In order to check the accuracy of the data quantitatively the values of gravity profiles at crossovers are usually compared. Unfortunately, there were no crossovers during cruise SO201 because of time constraints.

PRELIMINARY SCIENTIFIC RESULTS

1.13 Bathymetry and morphotectonics of the Emperor Seamount Chain

S. Ladage, R. Freitag

Bathymetric mapping was conducted throughout the cruise SO201-Leg1a. The data achieved so far are along-track lines and do not yet provide a comprehensive bathymetric relief map of the study area. Further bathymetric surveying is necessary during the following cruises. Compared to the 30 minute resolution of the SRTM30PLUS data set, the acquired bathymetric data give far more details. The ground resolution of the SIMRAD EM120 system is between 100 m to 200 m.

During the transit from Yokohma to the Emperor Seamount Chain the abyssal plain of the NW Pacific plate has been crossed. Water depths range between 4000 m and 6400 m. The seafloor relief is very moderate in general. The track ran oblique to the spreading fabric of the oceanic crust. Some relief can be observed while crossing the former transform faults. Several small seamounts and abyssal hills have also been crossed. The seafloor is draped by a pelagic sediment cover, modulating and reducing seafloor relief (Fig. 1.18.13 - Fig. 1.18.18).

Emperor Seamount Chain

The Emperor Seamount Chain has been crossed by five bathymetric tracks during SO201 Leg1a (Fig. 1.13.1). The shallowest water depth of 1245 m was measured on top of Jimmu seamount, the southernmost seamount crossed during this leg. Jimmu seamount rises more than 4500 m above the surrounding seafloor. The more northerly seamounts are not quite as high and reach heights up to 3500 m above surrounding seafloor or about 2500 m water depth.

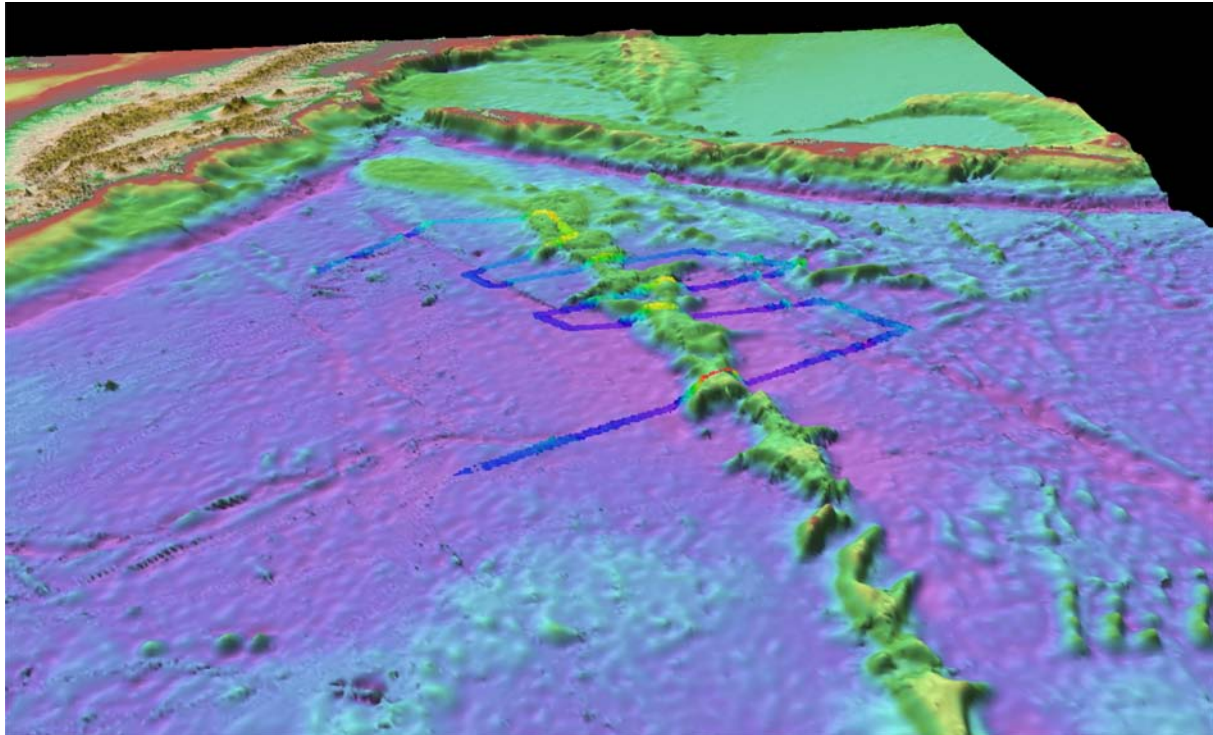


Fig. 1.13.1: 3D-view of the NW Pacific with the Emperor Seamount Chain, the Kurile, and the Kamchatka trench. The survey tracks are overlain onto the SRTM30plus V5.0 data set.

The deepest areas with more than 6300 m water depth were measured around the foot of the Emperor Seamounts. These areas form depressions that are about 300 km wide and some 300 m deeper than the surrounding abyssal plain (Fig. 1.13.3). Those depressions are formed by flexural bending of the oceanic lithosphere due to the excess weight of the seamounts. The depressions are more pronounced in the southern part of the survey area (covered by profiles BGR09-101, -103 and -105), whereas in the northern part (covered by profiles -107 and -109) it can hardly be observed.

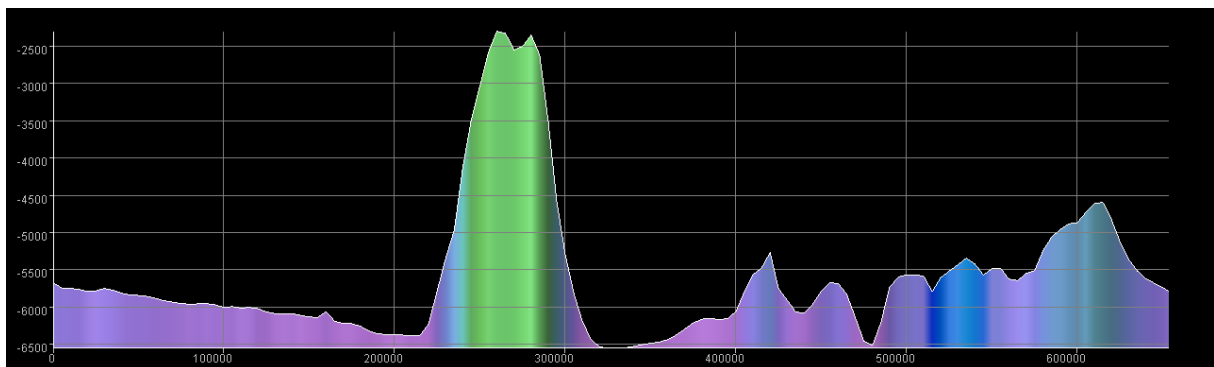


Fig. 1.13.2: Depth profile along line BGR09-103

The western flanks of the seamounts are inclined with angles of 4° to 6° on average, whereas the eastern flanks are slightly steeper with $\sim 8^{\circ}$ - 10° . These slope inclinations are in accordance with slopes of recent ocean island shield volcanoes. Considerably steeper inclinations are observed near slump scars, fractures or faults (Fig. 1.13.3). The steepest slope of $\sim 20^{\circ}$ inclination is located on the western flank of the ridge crossed by profile -107.

In a first approximation the seamount chain is elongated in NNW-SSE direction. However, several morphological highs cut across or are superimposed on the volcanic massifs. The architecture and shape of the seamounts is rather irregular and they appear to be intensively eroded. Several erosional features are observed along the BGR profiles. Slumps, slump scars and gullies are common on the hill slopes (Fig. 1.13.3). Several slump scars as well as a large gully canyon traversing the hill slope can be seen. These erosional processes lead to a rough, irregular morphology of the seamount flanks.

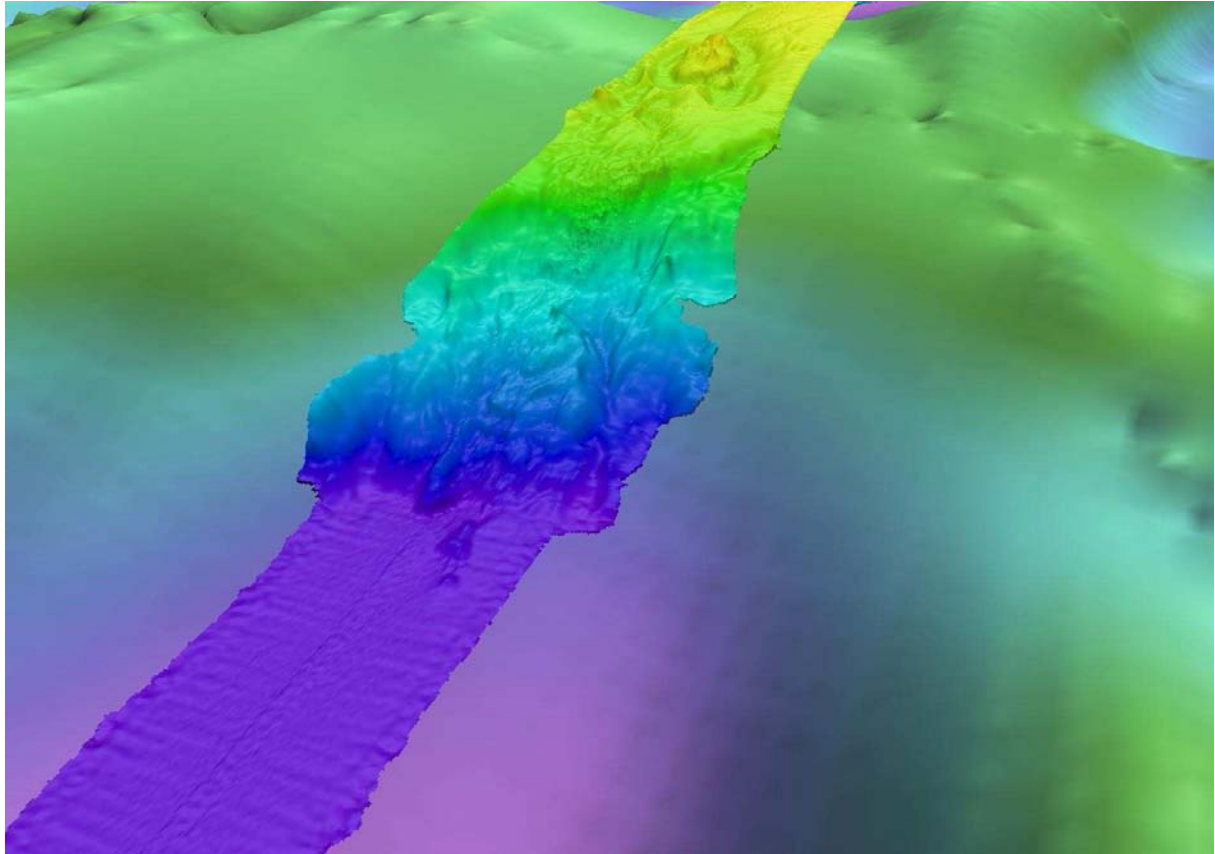


Fig. 1.13.3: 3D-view of the eastern slope of a seamount along line BGR09-103 (view to west). Slump debris is observed at the base of the seamount, as well as gullies and several slump scars at the slope.

On the western flank of the seamount chain along line BGR09-107 a 15 km long block is presumably bordered by fault scarps (Fig. 1.13.4). From the Parasound and the MCS data the block is interpreted as a sedimentary unit. The very steep foothill scarp is about 200 m high. The whole block was possibly creeping or has been sliding downhill.

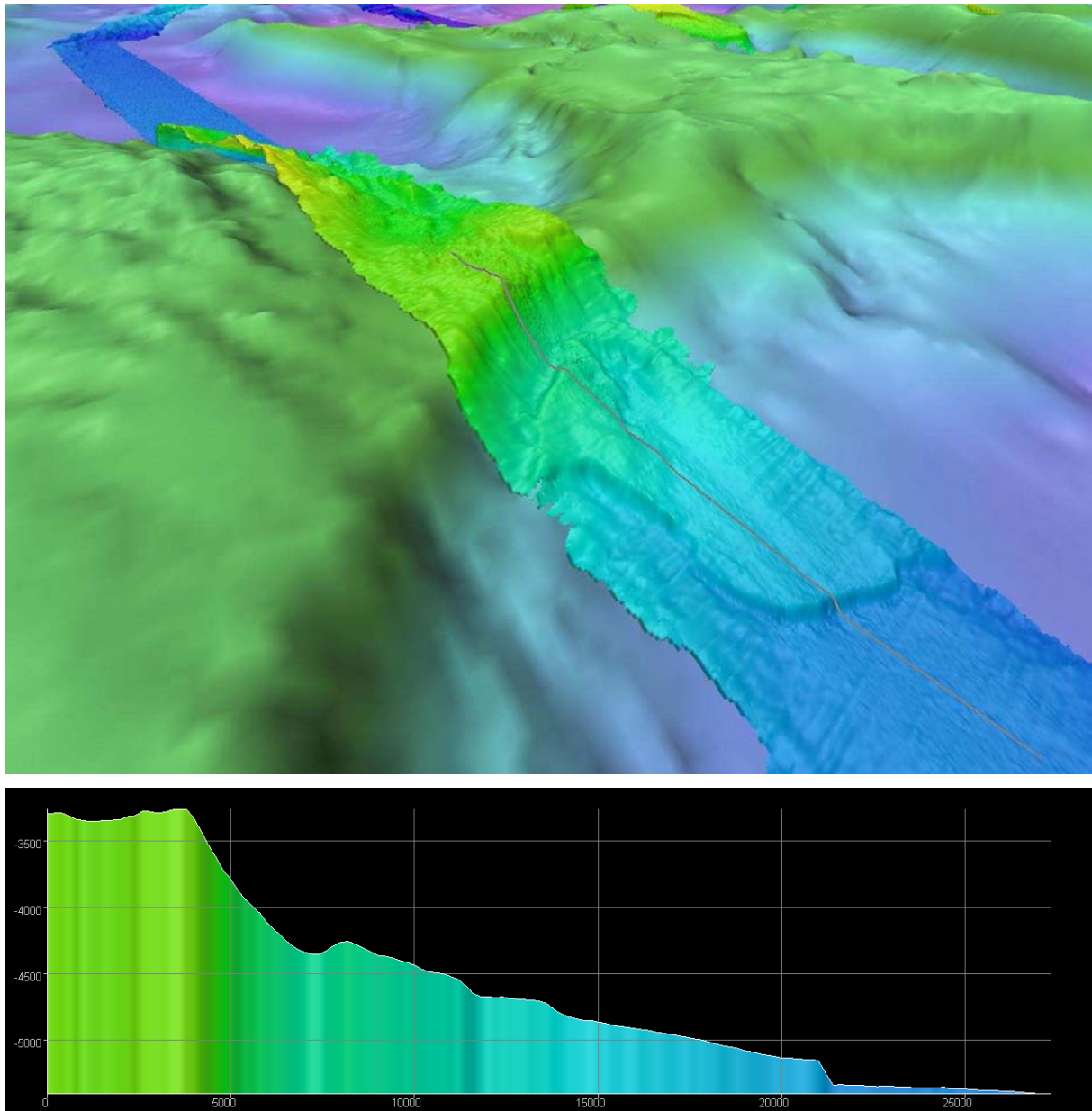


Fig. 1.13.4: Top: 3D-view of the western slope of a seamount (view to east). Bottom: Cross-section along line BGR09-107. Note the scarp along the upper part of the slope and the V-shaped trough parallel to the slope. Note also the steep offset of ~ 200 m at the foot of the slope.

Jimmu Seamount - Guyot

Jimmu Seamount, surveyed with profile BGR09-101 (Fig. 1.13.5), has a remarkably flat top and is the only guyot observed during this cruise. Therefore we suggest that Jimmu Seamount has once been exposed above sea-level. The summit platform exhibits terraces that are slightly ocean-ward inclined, which may be interpreted as paleo-shorelines.

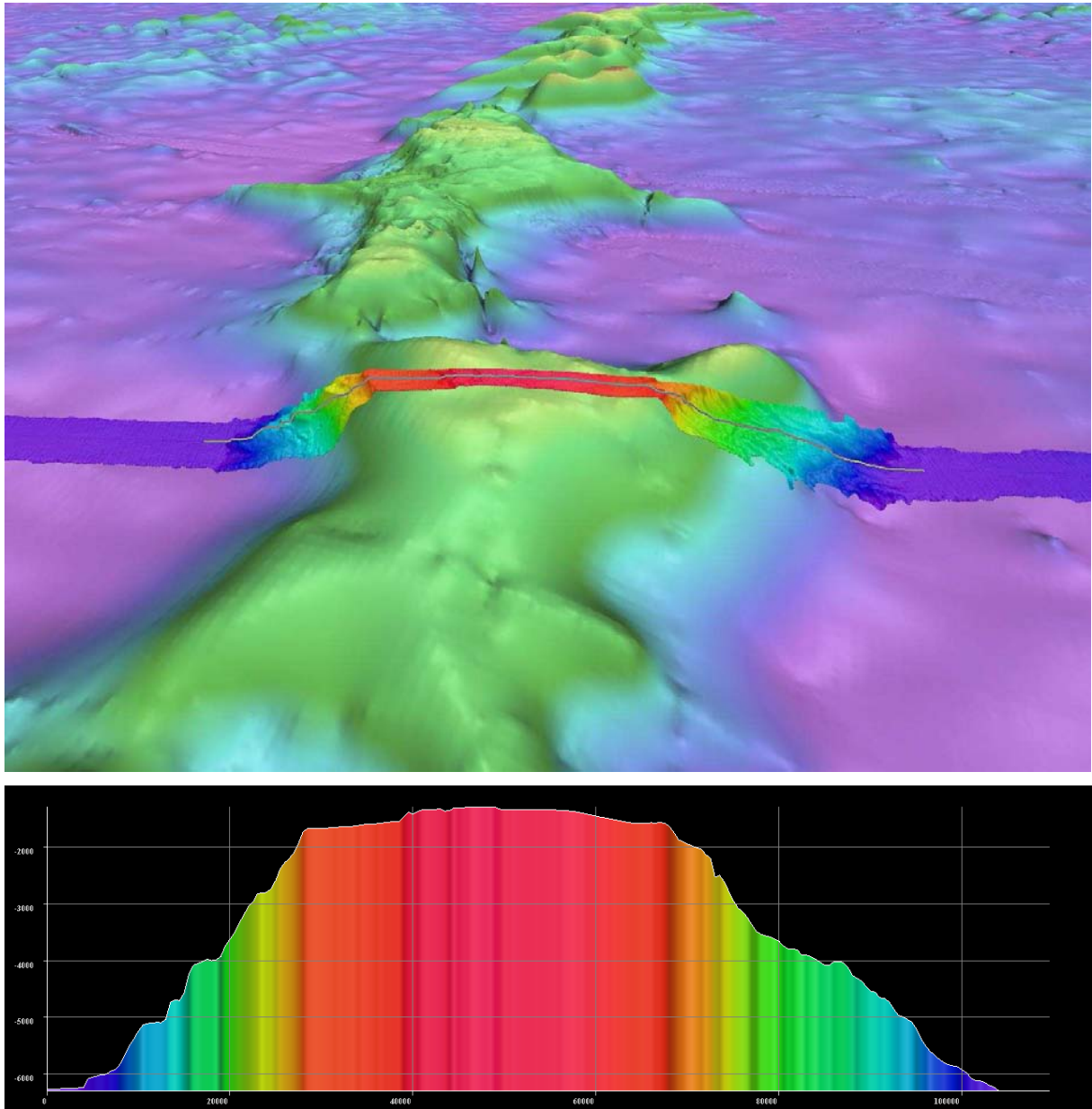


Fig. 1.13.5: 3D-view (top) and cross-section (bottom) of Jimmu Seamount (view to the south) Profile -103 crossed the seamount chain between two bathymetric highs. A small volcanic caldera with a central cone, about 500 m high was mapped (Fig. 1.13.6). The diameter of the caldera is about 8000 meters and it is 150 meters deep, measured from the rim. The central cone resembles a lava dome.

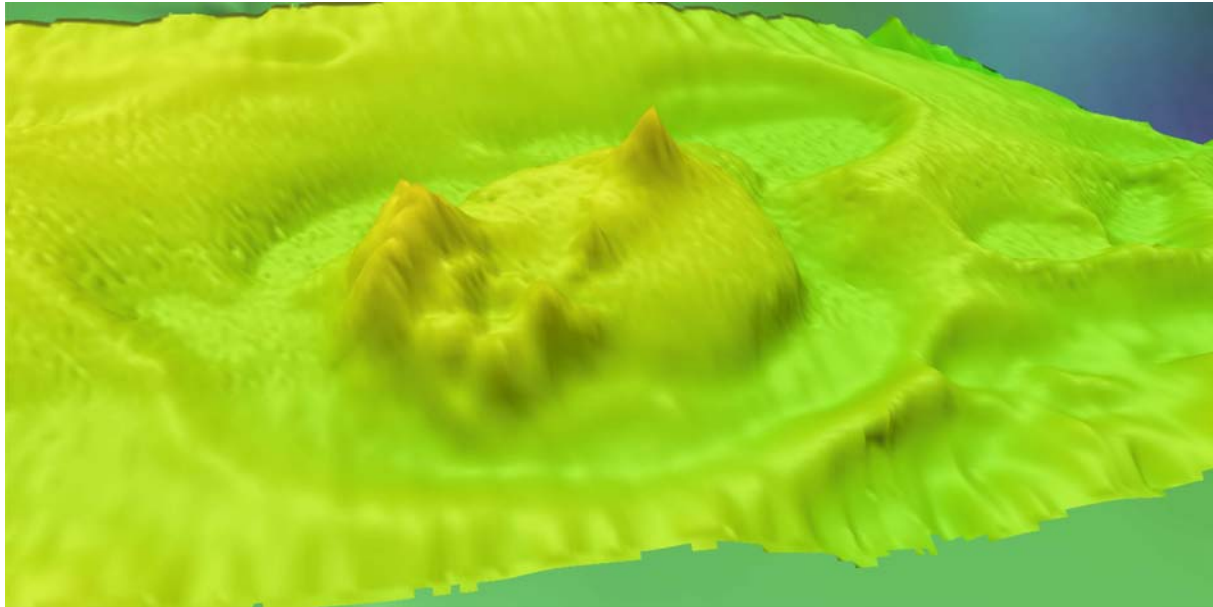


Fig. 1.13.6: 3D-view of a caldera mapped along profile BGR09-103.

West Emperor Fault

Approximately 100 km west of the northern Emperor Seamount Chain a prominent fault extends for some 700 km in NW-SE direction. We crossed this fault four times during SO201 Leg1a and termed it West Emperor Fault (WEF; Fig. 1.13.7). It appears to be a normal fault with an increasing throw of up to 700 m towards the NW. The fault tip lies somewhere between lines BGR09-103 and BGR09-105. The hanging wall exhibits an elevated shoulder, some 100-200 m above the regional surface. We speculate that this could be due to elastic rebound. Several additional small-scale structures can be observed along the fault, such as a relay ramp along profile BGR09-107 (Fig. 1.13.8).

The WEF lies parallel to the former transform faults of the NW Pacific plate and it may be that this normal fault formed at the zone of weakness induced by such a transform fault. The fault possibly has a regional significance because a WSW-ENE trending structural high that cuts across the seamount chain connects fairly well to the fault. This structural high separates two morphological domains of the oceanic crust around the seamount chain. As described above, the southern part exhibits the well developed downflexure of the oceanic lithosphere. In contrast in the northern part this flexure is not as strongly developed, or absent.

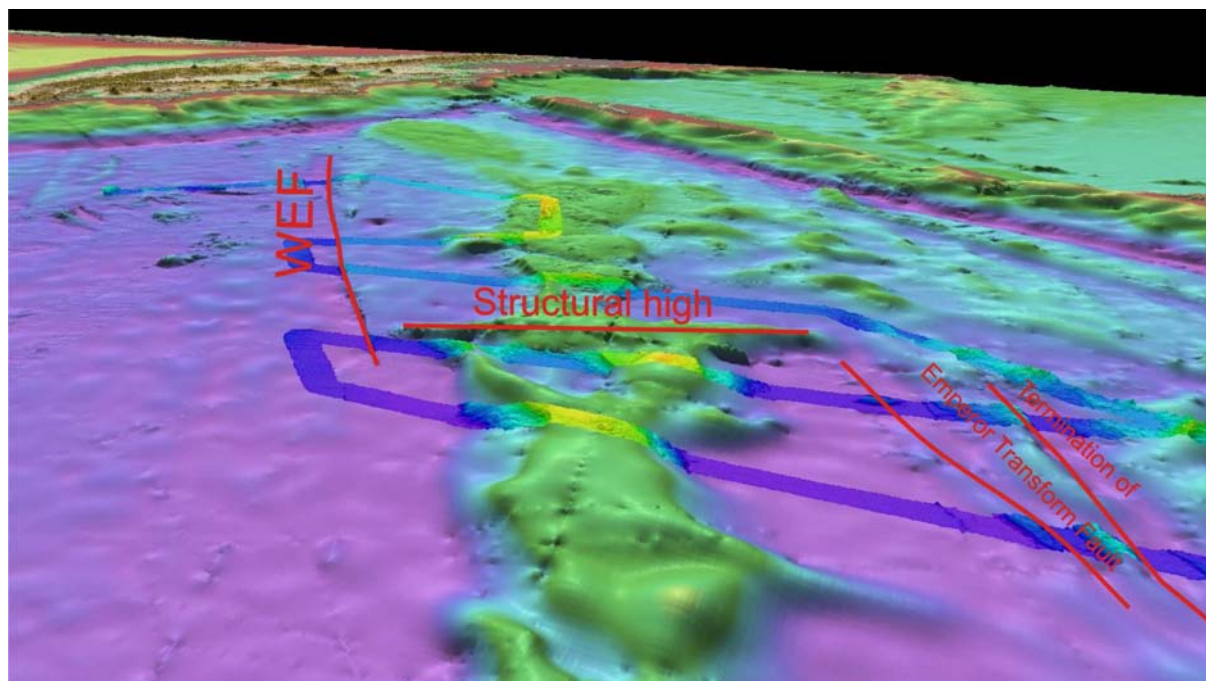


Fig. 1.13.7: 3D-view of the West Emperor Fault and morphotectonic setting.

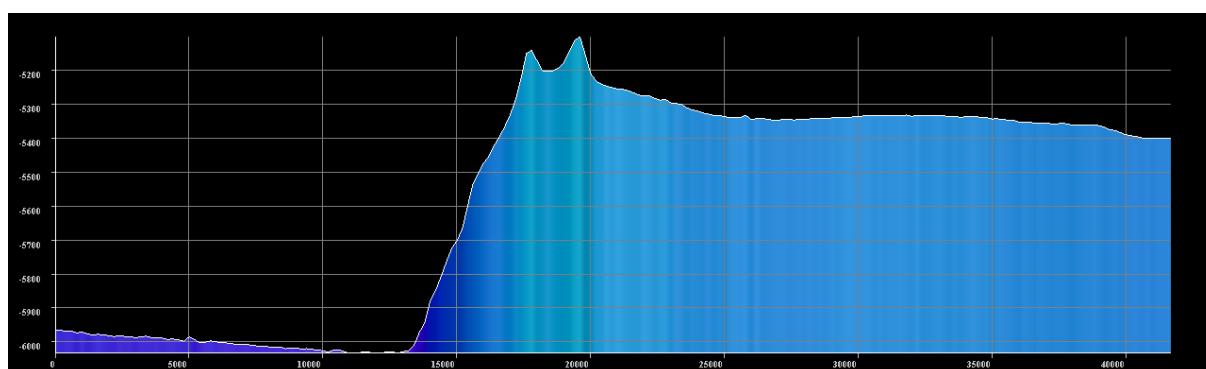


Fig. 1.13.8: Detailed 3D-view 3D-(top) and cross section (bottom) of the West Emperor Fault along line BGR09-107. Note the relay ramp

1.14 Multi-channel seismic interpretation

C. Gaedicke, D. Franke, S. Ladage

Multi-channel seismic profiles (MCS) were interpreted on migrated time sections. We are fully aware that interpretation is only preliminary and restricted to brief descriptions of major seismic units and tectonic structures.

Oceanic crust

The oceanic crust is partly transparent, partly diffractive down to the Moho level. Its top generally lies below about 8 s TWT west of the seamount chain (Fig. 1.14.1). Its top is a distinct, continuous reflector that is highly dissected by normal faults. Throw along these faults is around 300 ms TWT. A few reflections at about 0.75 s TWT beneath the top oceanic crust reflection may represent the layer 2 / layer 3 transition.

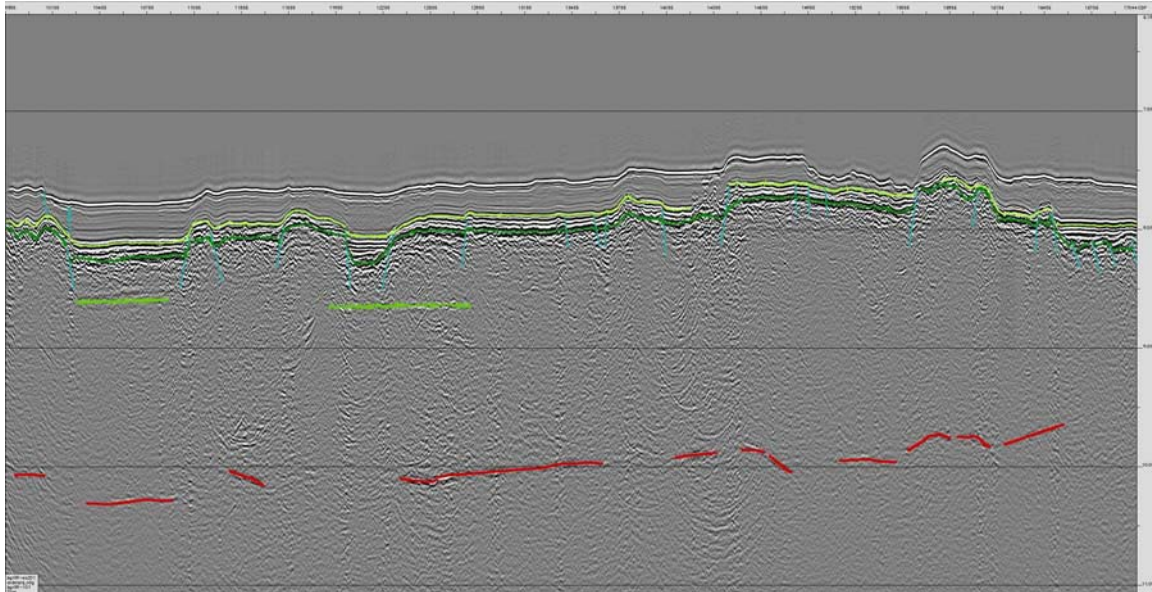


Fig. 1.14.1: Part of multi-channel seismic profile BGR09-101 imaging the typical oceanic crust west of the Emperor Seamount Chain. (colours: red = Moho reflection, light green = intraoceanic crust reflection, dark green = top-oceanic crust, light green = 'base of sediments', cyan = normal fault).

Identification of the top-oceanic crust reflection was hampered in the vicinity of the seamounts by additional, distinct low-frequency reflections on top of the assumed oceanic crust. This reflection band thickens towards the seamounts and is probably caused by lava flows, tuffs, ashes, and volcanic edifices that were emplaced during seamounts formation. This reflection band may also comprise sedimentary layers. In the stacked seismic sections the top oceanic crust reflection appears as a typical highly diffractive horizon. However, at the inflection points, close to the onset of the low-frequency reflections on top, it changes from highly diffractive to more continuous, hummocky reflections. Occasionally it is possible to trace the top-oceanic crust reflection for some kilometers beneath the seamounts. Apparently this area was uplifted during the formation of the volcano.

On the eastern side of the southern seamounts the wedge-shaped trough reaches a depth of about 10 s TWT (thickness of 1.8 s TWT). The thickness of the volcanoclastic infill is up to 1 s TWT on both sides of the seamount. However in the east, the volcanoclastic infill is tilted, indicating continuing subsidence in the east after the emplacement of the seamount.

Moho

Moho reflections occur around 10 s TWT, predominantly more than 100 km away from the seamounts and on their western sides (Fig. 1.14.1). The oceanic crust bends from around 8 s TWT down towards the seamounts for about 90 km and it reaches a depth of 9 to 10 s TWT at the foot of the seamounts. The wedge-shaped trough (thickness of 1.0 s TWT) is filled up in the southern part of the study area by volcano-sedimentary material, levelling out the depression, while towards the north subsidence continued after the emplacement of the volcano-sedimentary wedge fill.

Seamounts

Seamounts form prominent features on the oceanic crust. They rise to more than 6.5 s TWT above the surrounding seafloor in the south of the study area. In map view the seamount chain displays a zigzag pattern, the two directions being NNE and NNW. The tops of the seamounts have an almost flat morphology that appears to be erosional which characterises them as guyots. There are central elevations rising over the guyot surfaces that have the same reflection characteristics as the surrounding seamount crust. These may be secondary volcanic buildups that modified the formerly flat morphology. Line BGR09-103 crosses a seamount with a caldera (diameter 6.5 km) near the center of the ridge.

Near the seamount surfaces the reflection pattern is similar to that above the oceanic crust adjacent to the seamounts (Fig. 1.14.2). The eastern flanks of the seamounts are usually steeper than the western flanks, except along BGR09-105, where the seamount is tilted towards the west. Here, the seamount chain splits up into two seamounts with a depression in between. The oceanic crust beneath this depression is elevated by about 1 s TWT compared to the surrounding depth of the oceanic crust.

The western flanks are partially covered with sediments up to 200 ms TWT thickness. Along line BGR09-109 the seamount forms two separate blocks both of which are around 20 km wide. There might be a major, westward dipping normal fault dissecting the seamount into two larger tilted blocks.

The flanks of the seamounts are generally dissected by numerous steep normal faults. Internally, the seamounts are widely transparent. However, on lines BGR09-101 and -103 (Fig. 1.14.2), there are prominent internal reflectors 0.75 s TWT beneath the sediment base reflector. On line BGR09-103, this reflector follows the topography of the seamount surface, while on line BGR09-101 this reflection dips towards the east and is truncated by the seamount surface near its centre. Deep structures of the seamounts may be masked by seafloor multiples.

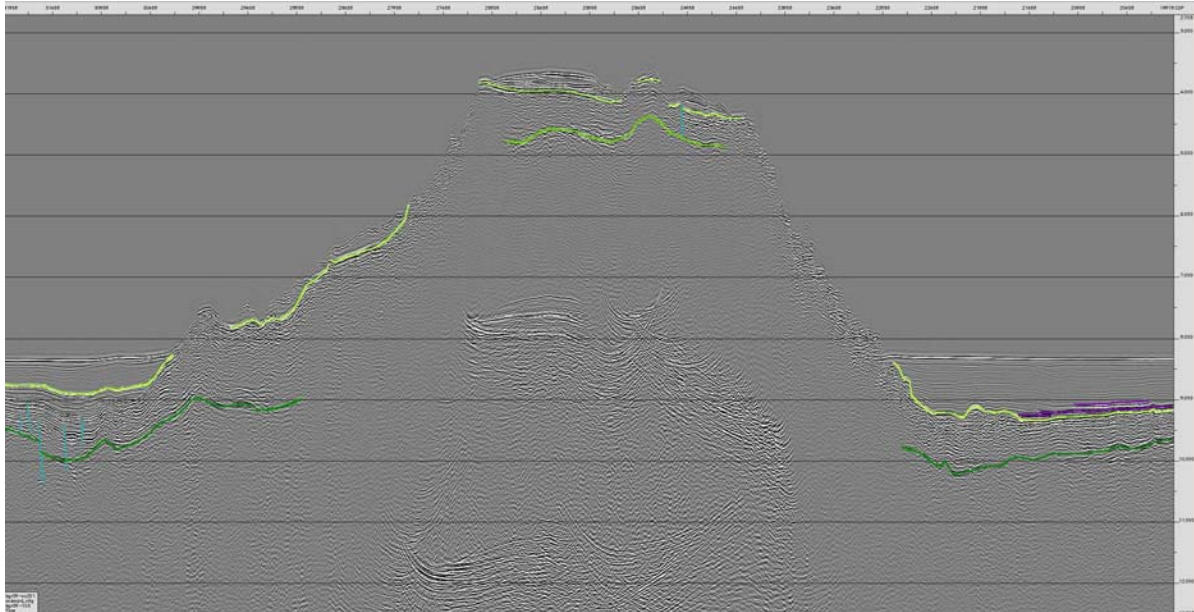


Fig. 1.14.2: Part of multi-channel seismic profile BGR09-103 crossing the Jimmu Seamount. For colours refer to **Fig. 1.14.1**

Perched packages of stratified sediments are widespread on top of the seamounts. Stratification is mostly near-horizontal with internal truncating reflections. In addition, there is one sediment package on Line BGR09-105, where the strata are inclined and thin towards the SW. The depression between the two separate seamounts along line BGR09-105 is filled with 800 ms TWT of sediments.

Sediment packages are thin (thickness 300 ms TWT) in the southern part of the study area. On line BGR09-107, the major seamount (which is significantly lower than those in the south) shows a larger, concave-up depression that is almost devoid of sediments.

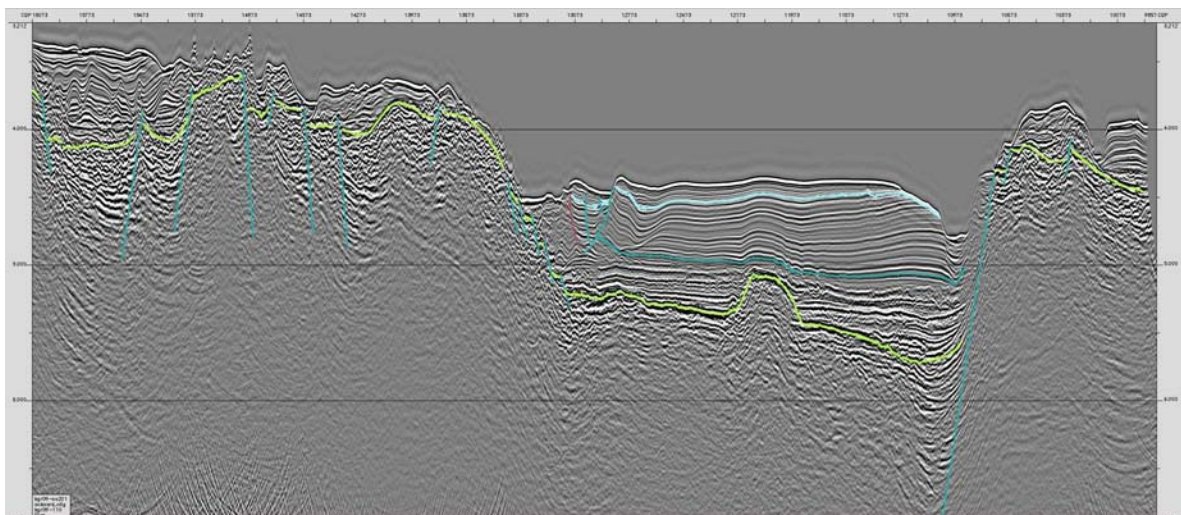


Fig. 1.14.3: Part of multi-channel seismic profile BGR09-110 crossing the Wayne seamount. For colours refer to **Fig. 1.14.1**

On Wayne seamount (BGR09-109 to -111) the sediment packages display a greater proportion of internally undulating reflections with sediments pinching out in comparison to the profiles to the south (Fig. 1.14.3). On line BGR09-109 there are two sedimentary packages to the SW and to the NE of the major normal fault

described above. The internal reflection pattern of both packages is very similar. While the reflectors in the NE package lap onto the inclined seamount surface, the corresponding reflectors are truncated on the NE side of the SW package. The intervening depression appears to be erosional. The same SW package is truncated on its SW side towards an erosional depression, but in addition the sediments pinch out slightly towards the SW.

On lines BGR09-109 through -111, the degree of filling of erosional depressions ranges from those devoid of any later infill, over v-shaped depressions that are filled half-way to those that are completely filled. Internally, these infills show undulating thicknesses and pinch-outs.

In summary, the co-existence of erosional truncations of sedimentary packages, channel-fills, undulating thicknesses and pinch-outs within the sedimentary packages accounts for a significant contribution of deep-sea currents on the depositional environment.

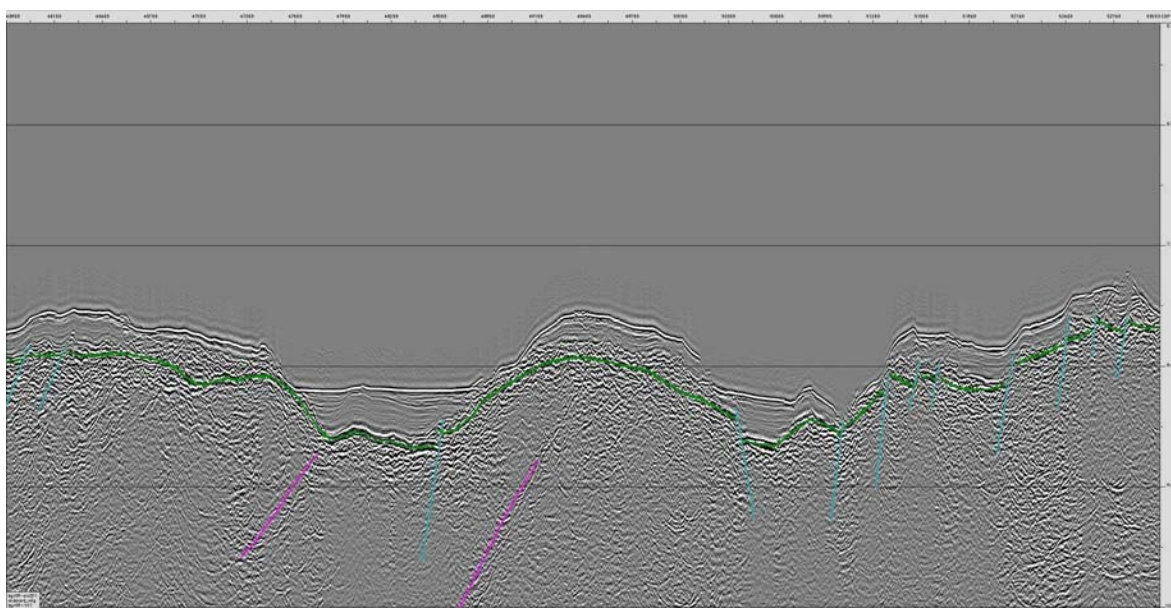


Fig. 1.14.4: Part of multi-channel seismic profile BGR09-101 crossing a fracture zone east of the Emperor Seamount Chain. For colours refer to **Fig. 1.14.1**

Fracture zones

The most prominent fracture zone, which occurs on the eastern side of the Emperor Seamount chain is already visible on the satellite altimetry data. It is traceable starting from the SE and meets the study area in an acute angle. On the seismic data, this fracture zone appears not as a single fracture, but comprises of a complex pattern of ridges and basins, separated by fractures. On profile BGR09-101 two basins border one prominent ridge (Fig. 1.14.4). The basins are filled with about 400 ms (TWT) of sediments. They are bounded by two normal faults. The ridge is elevated about 450 meters above the top of the basin sediments. In general, the relief in this southernmost profile is quite smooth compared to the northern profiles. The total difference in topography is less than 700 meters.

On Profile BGR09-103, a wider portion of the fracture zone is imaged. It consists of two ridges which are separated by a basin (Fig. 1.14.5). These ridges are elevated about 1500 and 500 meters above the surrounding seafloor; respectively. The lower

flanks of the higher seamount are inclined in a similar angle. On Profile BGR09-105 the fracture zone looks different: again two basins border one asymmetric ridge (Fig. 1.14.6). The ridge is elevated about 1100 meters above the top of the adjacent basin and is about 38 km wide. The peak of this ridge is located in the east and the eastern flank is steeper than the western. The major fault of the fracture zone may be located near the eastern flank.

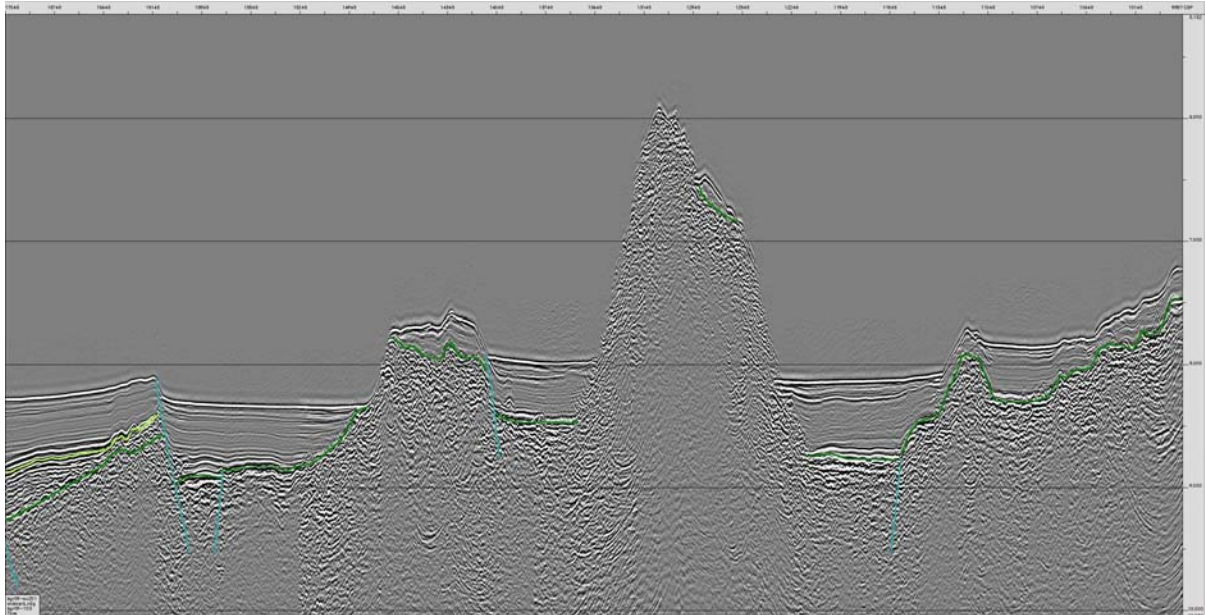


Fig. 1.14.5: Part of multi-channel seismic profile BGR09-103 crossing fracture zone east of the Emperor Seamount Chain. For colours refer to **Fig. 1.14.1**

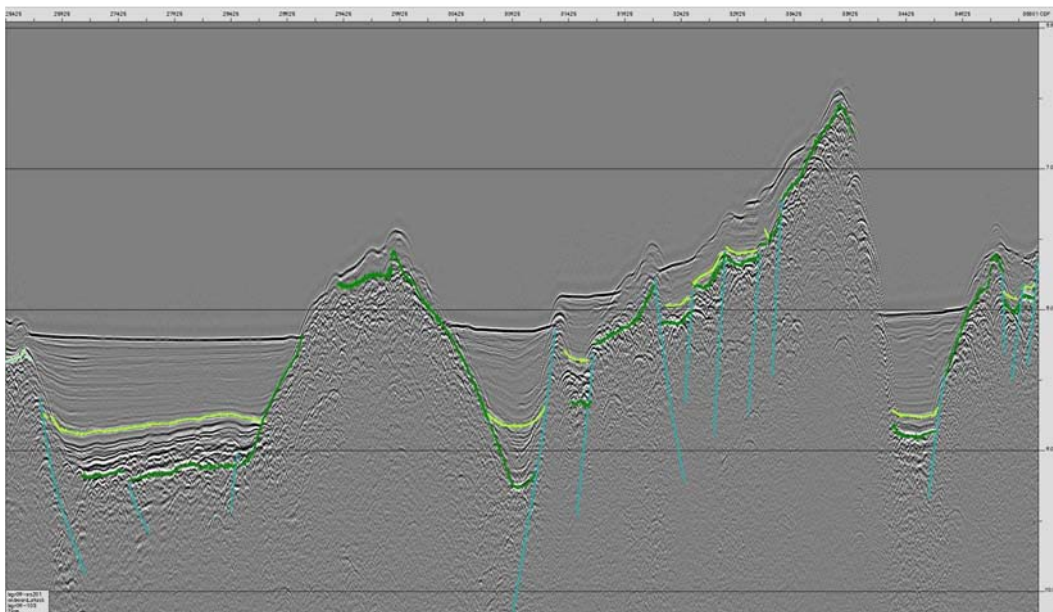


Fig. 1.14.6: Part of multi-channel seismic profile BGR09-105 crossing fracture zone east of the Emperor Seamount Chain. For colours refer to **Fig. 1.14.1**

Sedimentary unit

We distinguished two sedimentary environments in the working area: (1) the deep sea on oceanic crust away from the influence of seamount, and (2) the deep sea in the vicinity of seamounts.

(1) The oceanic crust is covered by a sedimentary sequence with parallel, continuous low amplitude reflections. This sequence drapes the oceanic crust. Its thickness varies between 300 to 350 ms (TWT) depending on the relief of the underlying crust (Fig. 1.14.1). Generally the thickness is higher in depressions than on oceanic ridges. The uniform thickness, transparent appearance and draping character point to a pelagic origin of this sequence that typically consist of diatom ooze with admixtures of clay and volcanic ash at ODP Site 881 (Shipboard Scientific Party, 1992).

The uppermost part of this sequence shows perfectly stratified sediment in Parasound records. Penetration is up to 60 m. The parallel reflections are traceable over hundreds of kilometers and thus confirm the pelagic origin of this unit.

On the western part of profile BGR09-101 we observe an erosional channel some 9 km wide and 180 m deep cutting through the pelagic sequence (CDP 14900 to 15680).

(2) The seamounts have a significant impact on the sedimentary environment in their vicinity. The lithospheric flexure of the oceanic crust due to the density and volume of the seamounts lead to an increase of the accommodation space and to the formation of separate basins parallel to both side of the seamount chain. The oceanic crust lies at a depth of 8.0 s (TWT) some 100 km to the west of the Jimmu Seamount whereas it lies at 9.4 s (TWT) at the toe of a seamount (Fig. 1.14.7). The thicknesses of both, the pelagic sediments described above and of the underlying sediments increase towards the seamounts. The lower sequence is about 1.4 s (TWT) thick and displays continuous high-amplitude reflections in its upper part. The lower part of this sequence may also shows discontinuous, sometimes even chaotic reflections with lower amplitudes. Therefore, the lower boundary to the underlying oceanic crust is not well imaged as a strong reflector.

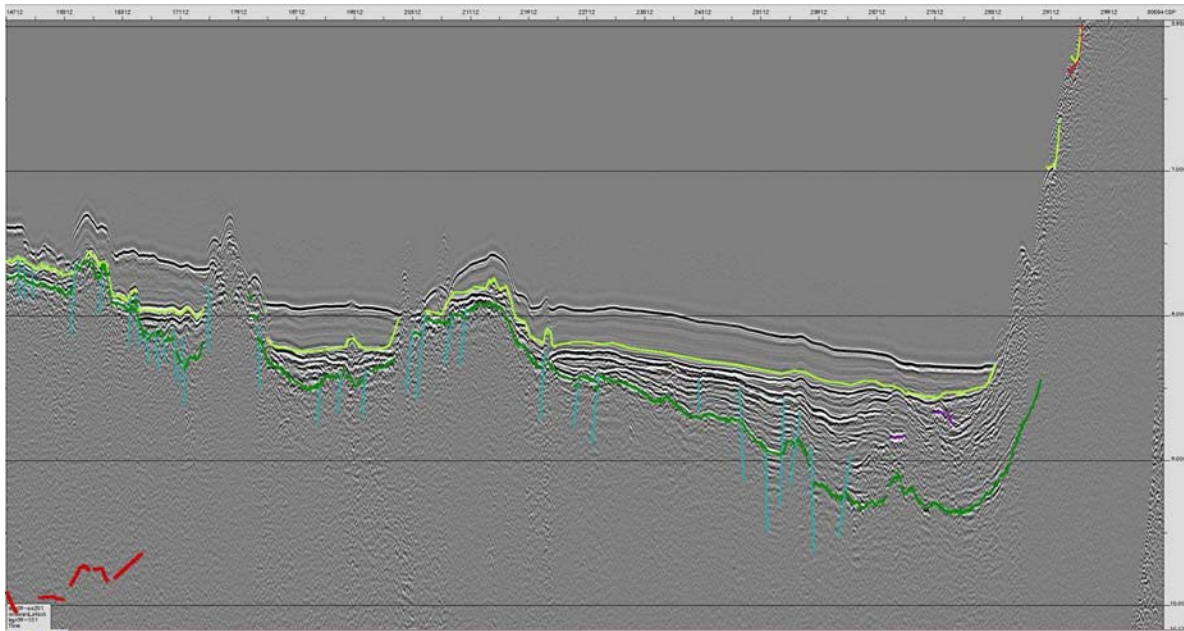


Fig. 1.14.7: Part of multi-channel seismic profile BGR09-101 crossing the flexural basin west of the Jimmu Seamount. For colours refer to **Fig. 1.14.1**

In the vicinity of the seamounts, the upper sequence differs slightly from the typical oceanic environment. The thickness is up to 1.0 s (TWT) to the NE of Jimmu Seamount. Within this sequence, transparent facies suggest the activity of mass wasting processes like debris flows, which originated on the flanks of the seamounts. On profile BGR09-103, one single debris flow is traceable for at least 30 km. Its thickness is about 150 ms (TWT). In the lower part of this sequence, some high amplitude reflectors (bright spots) occur. These reflectors are preliminarily interpreted as volcanic sills.

1.15 PARASOUND recordings

T. Pletsch, E. Sukhooev, H. Thöle, N. Tsukanov

Approximately 6000 line kilometers of high-resolution sub-bottom profiles were collected during cruise SO201 Leg 1a using the PARASOUND system. The general observations from the obtained Parasound records within the survey area can be described as follows:

(1) The realm of the deep sea away from the influence of the seamounts is generally dominated by an acoustic facies characterised by numerous distinct, closely spaced and continuous parallel reflectors (Fig. 1.15.1). These reflectors are conformable with the surface topography and can be traceable over hundreds of kilometers. The acoustic penetration is often around 80 m. The draping character and the layered internal reflection pattern suggest undisturbed pelagic or hemipelagic depositional conditions which are typical for abyssal plains.

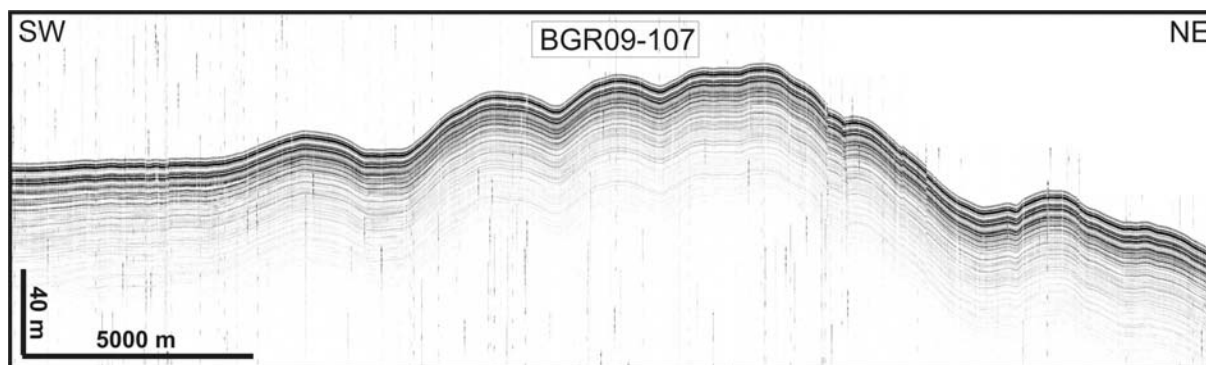


Fig. 1.15.1: Part of Parasound profile BGR09-107 showing perfectly stratified sediments, which are typical for the depositional environment of the abyssal plains.

(2) The uppermost sedimentary sequence along the Emperor Seamounts and other topographic highs is characterized by the occurrence of single and stacked transparent sedimentary lenses (Fig. 1.15.2 & Fig. 1.15.3). The stacked, transparent lenses are separated by single distinct reflection bands or by sequences of layered facies up to several metres in thickness. Commonly, the transparent acoustic facies fills topographic depressions and the thickness of individual lenses ranges from a few metres to more than 40 m. The geometry and the internal acoustic transparency of the observed features points to deposits related to mass wasting processes like debris flows that originated on the flanks of the sea-mounts. The acoustic transparency reflects internal homogenization, probably resulting from a disintegration of slope-failed masses by shear deformation and mixing with ambient water during debris flow formation (Middleton & Hampton, 1973; Nardin et al., 1979).

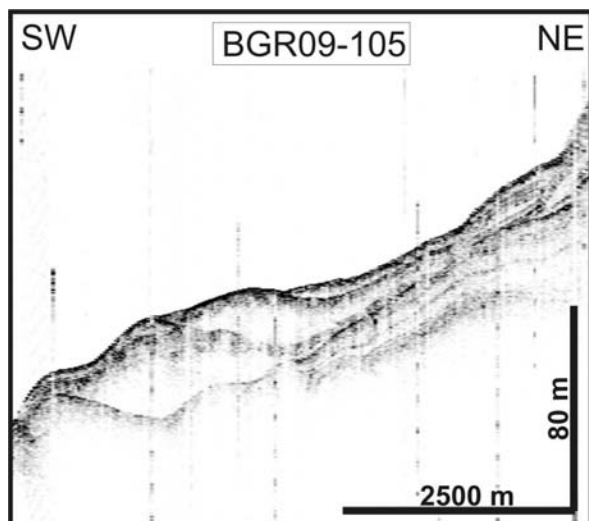


Fig. 1.15.2: Part of Parasound profile BGR09-105 showing two lenses of acoustically transparent masses on the western flank of the Emperor Seamounts.

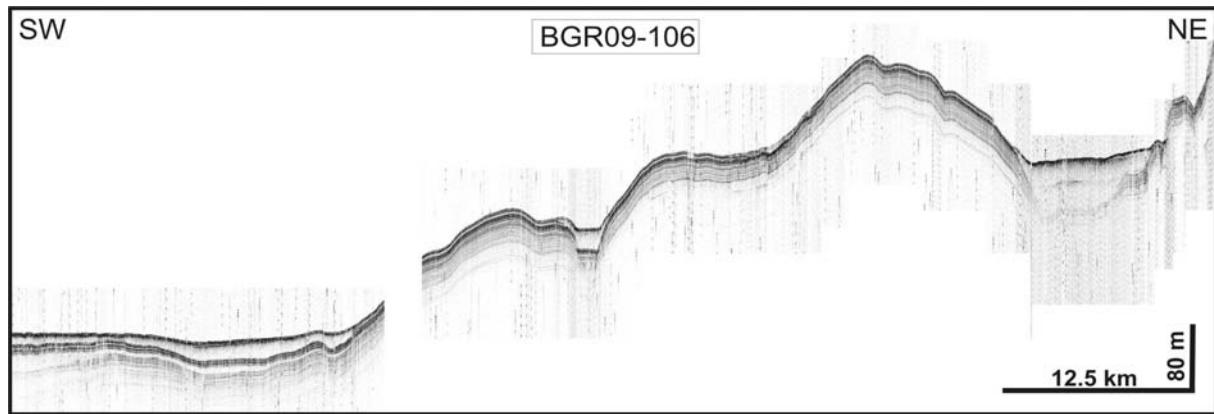


Fig. 1.15.3: Part of Parasound profile BGR09-107 showing acoustically transparent layers within the depressions.

(3) On the top of the seamounts, which often show an almost flat morphology there are individual sedimentary packages which partly show numerous parallel, horizontal reflectors. Apart from this hydroacoustic character so typical of deep-sea deposits (see above), parts of the sedimentary packages display undulating reflectors and pinch-outs. As seen in multi-channel seismics, there are depressions cutting across the sedimentary packages or delimiting these at their lateral borders towards the seamounts. These depressions display different stages of sedimentary infill (Fig. 1.15.4). The combination of undulating thicknesses, pinch-outs and depressions with different degrees of infill point to a depositional environment where both drift sediments and the cross-cutting erosional furrows may have originated from the activity of vigorous intermediate water currents.

Beside these stratified sediment packages strong seafloor reflectors also appear on the top of the seamounts. The sea in these areas floor is either covered with coarse-grained sediments or sediments are absent.

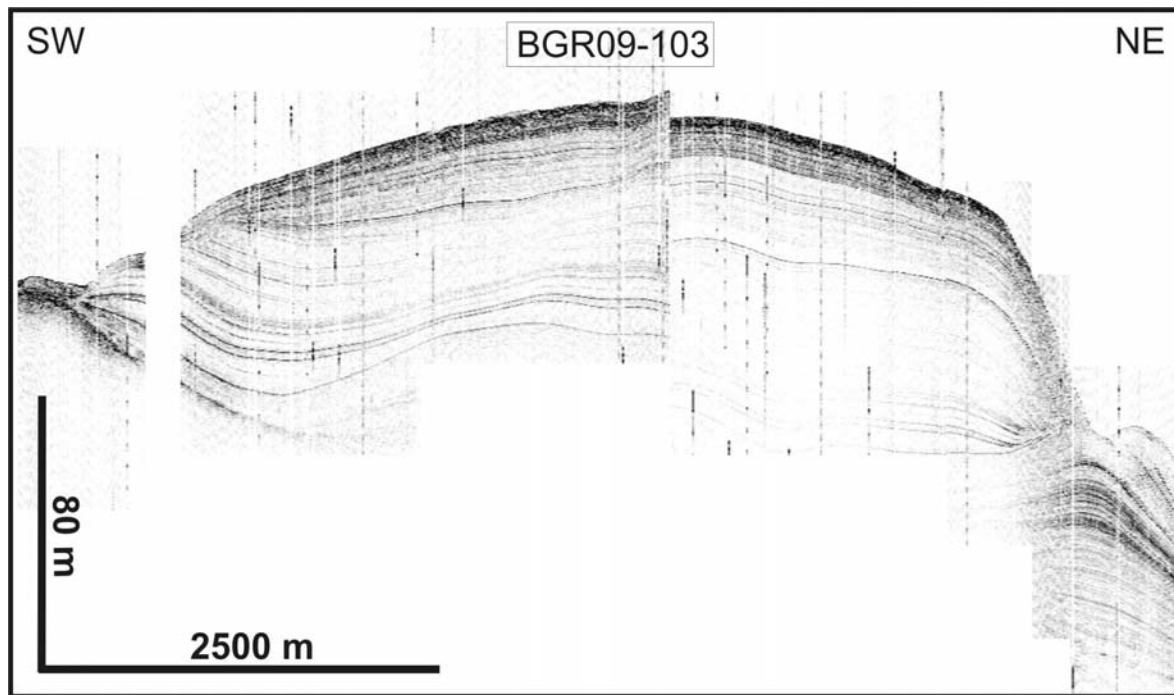


Fig. 1.15.4: Part of Parasound profile BGR09-103 showing an example of an individual package of stratified sediments on top of a seamount.

(4) Most of the high-resolution sub-bottom profiles crossing the flanks of the seamounts do not show information about the morphology or the structure of the sediments because slope angles usually exceed 4° and the signal of the Parasound echosounder is often lost due to the steep slopes. The diffuse reflections obtained from these areas provide no or little information about the uppermost sedimentary sequence on the flanks of the seamounts.

1.16 Magnetic and seafloor spreading anomalies

U. Barckhausen

1.16.1 Transit profiles

A compilation of magnetic lineations in the world's oceans (Cande et al., 1989) provides relatively good age information for the waters offshore northern Japan which were crossed during the transits from Yokohama to the study area and back. However, off the Kuril Islands and all the way north to the waters offshore Kamtchatka, major parts of the oceanic crust were formed during the so-called Cretaceous Magnetic Superchron when no reversals seem to have occurred between 83 Ma and 118 Ma (Fig. 1.16.1) and therefore the age of the oceanic crust in these areas can only be estimated.

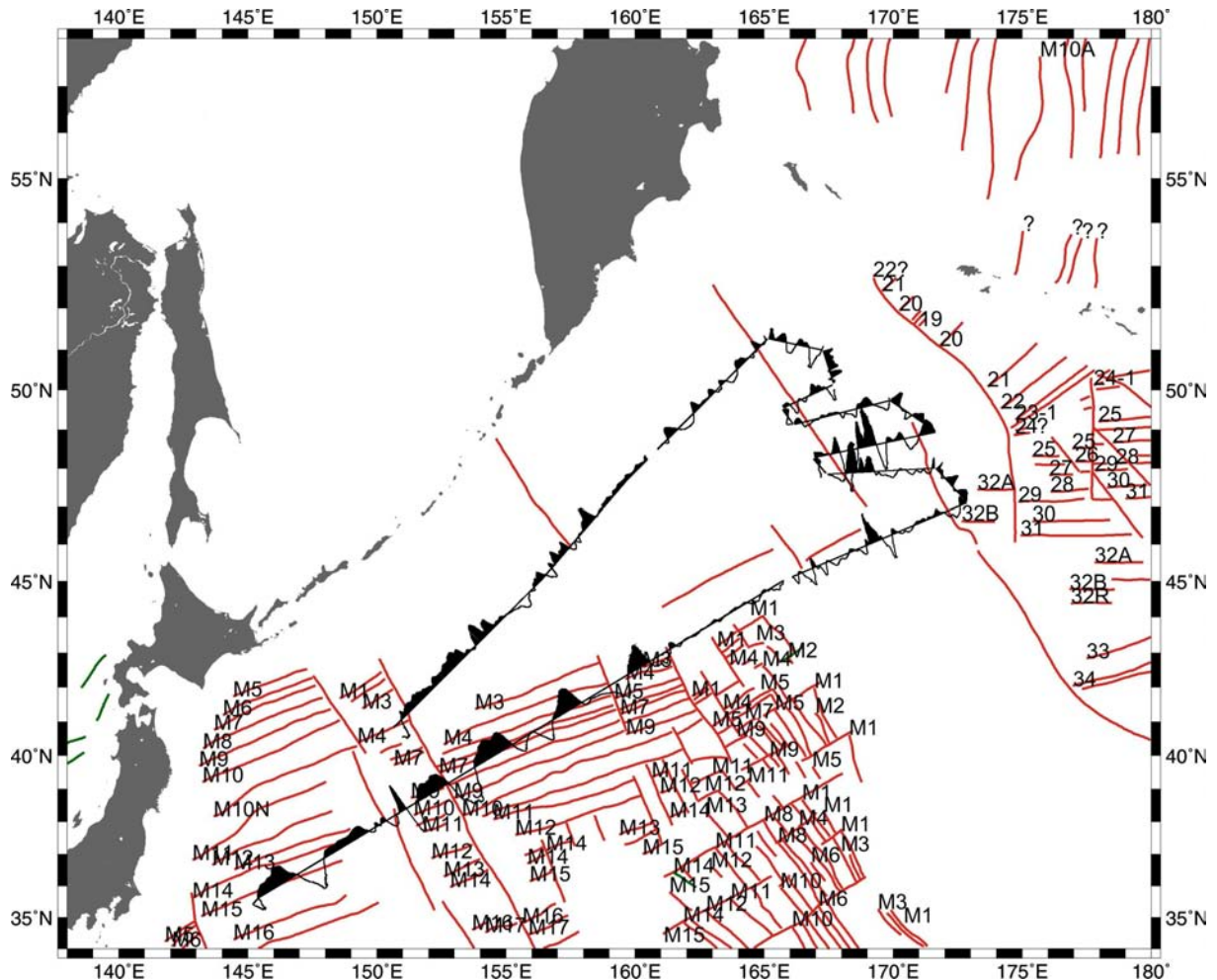


Fig. 1.16.1: Magnetic anomalies (red lines) of the northwestern Pacific after Cande et al. (1989). Numbers indicate magnetic chrons. Wiggles show magnetic anomalies along shiptracks of cruise SO-201.

The long transit which was necessary during cruise SO-201 to reach the study area was used for magnetic profiling with BGR's state of the art magnetometer array. The seafloor spreading anomalies which strike approximately N65°E offshore northern Japan were crossed at a very shallow angle by the transit profile BGR09-M02, sailed in direction N52°E. After full gradiometer processing, the magnetic data show the expected long wavelength anomalies of the 125 to 138 Myrs. old oceanic crust with sharp jumps where fracture zones were crossed. The seafloor spreading anomalies in this area offshore northern Japan are well studied and relatively easy to interpret given their large amplitudes so that there is no necessity to try to reinterpret them on the basis of Profile BGR09-M03 which is not very well suited for this purpose.

At longitude 161.3°E, the transit profile crosses a fracture zone which is associated with an age jump within the oceanic crust to ages younger than 118 Ma and thus belonging to the Cretaceous Magnetic Quiet Zone (CMQZ). The amplitudes of the anomalies drop to a fraction of the values observed further to the west and they are particularly low in this area since the profile runs almost exactly parallel to any existing magnetic and morphological structures formed at the spreading ridge. At longitude 166°E, the strike direction of these seafloor structures changes so that they were crossed almost perpendicularly and hence the amplitudes of the magnetic

anomalies increase even though the crust still belongs to the CMQZ. These magnetic anomalies cannot be interpreted as seafloor spreading anomalies.

The transit back to Yokohama was sailed parallel to the southeastern coast of Kamtchatka and along the Kuril Islands just outside the 200 nm EEZs of the Russian Federation and Japan. The major part of the oceanic crust surveyed with this magnetic profile (east of longitude 151°E) is believed to belong to the CMQZ. However, only a limited data coverage exists in this area so far, especially offshore Kamtchatka and the northern Kuril Islands. The amplitudes of the magnetic anomalies observed on our profile east of longitude 161°E are astonishingly large and the wavelengths very short for CMQZ crust with seafloor fabric structures that presumably strike perpendicularly to the well-defined fracture zones and thus sub-parallel to the profile's direction. In southwestern direction, a short section of the profile follows with very low amplitude magnetic anomalies as expected for typical CMQZ crust. However, at longitude 158°E another fracture zone is crossed by the profile and the character of the anomalies changes again to relatively large amplitudes and wavelengths which might resemble seafloor spreading anomalies. After crossing the fracture zone at longitude 151°E the well-mapped anomalies M3 and M4 off northern Japan were encountered and the profiling ended shortly thereafter.

1.16.2 Magnetic anomalies of the Emperor Seamount Chain area

Magnetic anomalies in the study area of the Emperor seamount chain are dominated by the high amplitude magnetic signatures of the giant seamounts. These result from the remanent magnetisations of the large basaltic bodies and overprint the weak background pattern of the anomalies originating from the older oceanic crust at the base of the seamounts (Fig. 1.16.2). The formation of each of the large seamounts over the Hawaii hotspot probably took at least several hundreds of thousands of years according to what is known from today's Hawaiian islands. As a result of the long time span which was needed to build up the huge basaltic bodies in countless volcanic eruptions, the individual lava flows have different remanent magnetisation directions and the seamounts do not express themselves in the magnetic field as classical dipole anomalies, but rather split up into a series of strong anomalies which are partly related to their morphology (Fig. 1.16.2), but mainly reflect the different stages of the seamount formation over time.

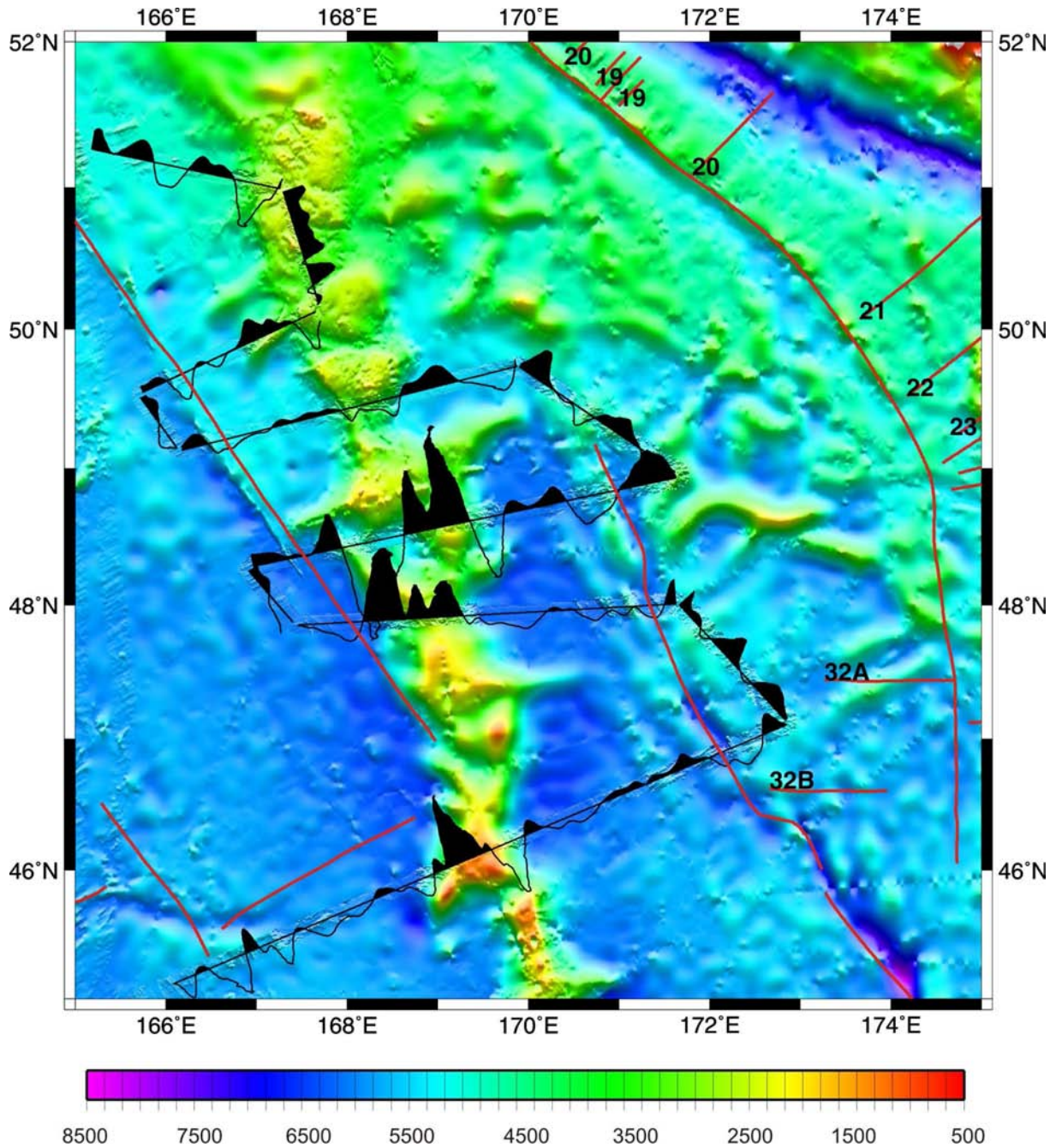


Fig. 1.16.2: Magnetic anomalies along ship tracks of cruise SO-201 over the Emperor seamounts shown as wiggles. Red lines are magnetic lineations after Cande et al. (1989). Numbers indicate magnetic chrons. Background shows the color coded bathymetry derived from satellite data.

The magnetic anomalies measured on the profiles of cruise SO-201 are generally in good agreement with those of the global compilation EMAG2 (Maus et al., 2008) (Fig. 1.16.3). The Emperor seamount chain forms a band of high amplitude anomalies surrounded by the weak anomalies of the underlying oceanic crust which presumably formed during the CMQZ. West of a fracture zone running subparallel to the Emperor seamount chain, the magnetic lineations map of Cande et al. (1989) shows east-west trending anomalies 32A and 32B. Profiles BGR09-102 and BGR09-106 were acquired in this area roughly parallel to the fracture zone. We tried o

correlate these profiles with a synthetic line calculated as a forward model from a magnetic reversal timescale (Cande and Kent, 1995) to test whether the new data would confirm a crustal age of roughly 70 Ma. (Fig. 1.16.4). The test shows that correlation with anomalies 30 through 32 is possible even though it must clearly be stated that the two short profiles with a gap between them are not sufficient to be regarded as a proof of correlation. The findings are in agreement with the anomalies in the map of Cande et al. (1989) since "32A" is the old name for the anomaly which in modern reversal timescales is being called "32n.1n" (Fig. 1.16.5).

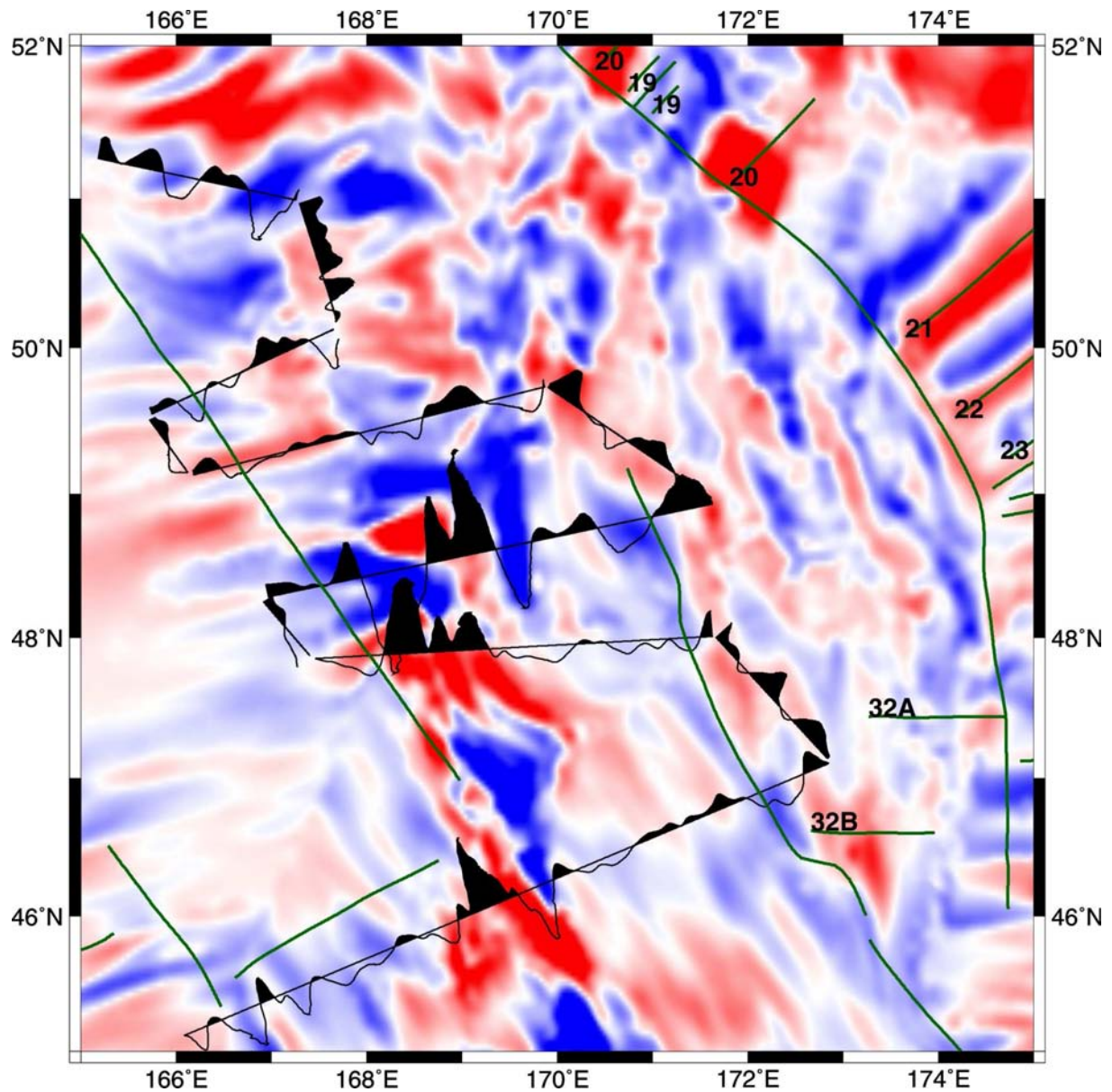


Fig. 1.16.3: Magnetic anomalies along ship tracks of cruise SO-201 over the Emperor seamounts shown as wiggles. Green lines are magnetic lineations after Cande et al. (1989). Numbers indicate magnetic chrons. Background shows magnetic anomalies of the 2-minute Earth Magnetic Anomaly Grid (EMAG2) (Maus et al., 2008); red: positive anomalies, blue: negative anomalies.

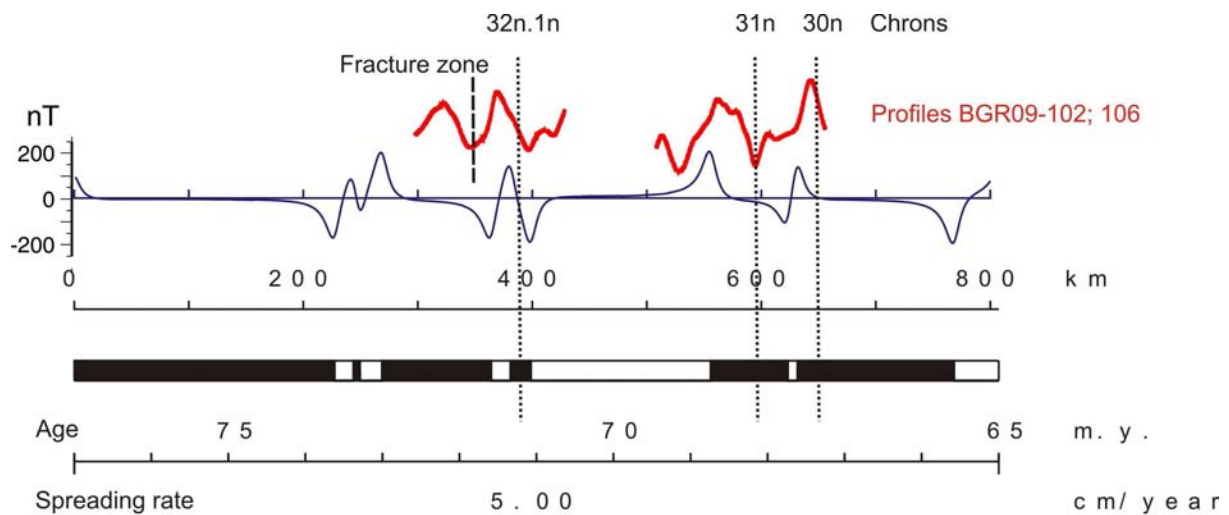


Fig. 1.16.4: Profiles BGR09-102 and BGR09-106 (red) correlated with a synthetic profile and age scale. The synthetic profile was calculated using the magnetic reversal time scale of Cande and Kent, 1995.

It was also tried to find correlations of the magnetic anomalies of the oceanic crust on the long profiles crossing the seamounts. However, it is only possible to draw some very tentative lines connecting some more or less prominent highs and lows in the profiles (Fig. 1.16.5). These lines coincide with the general trend of morphological structures at the seafloor where it is not overprinted by the seamounts. No identification of seafloor spreading anomalies was possible and hence no age can be attributed to the oceanic crust underlying the Emperor seamount chain.

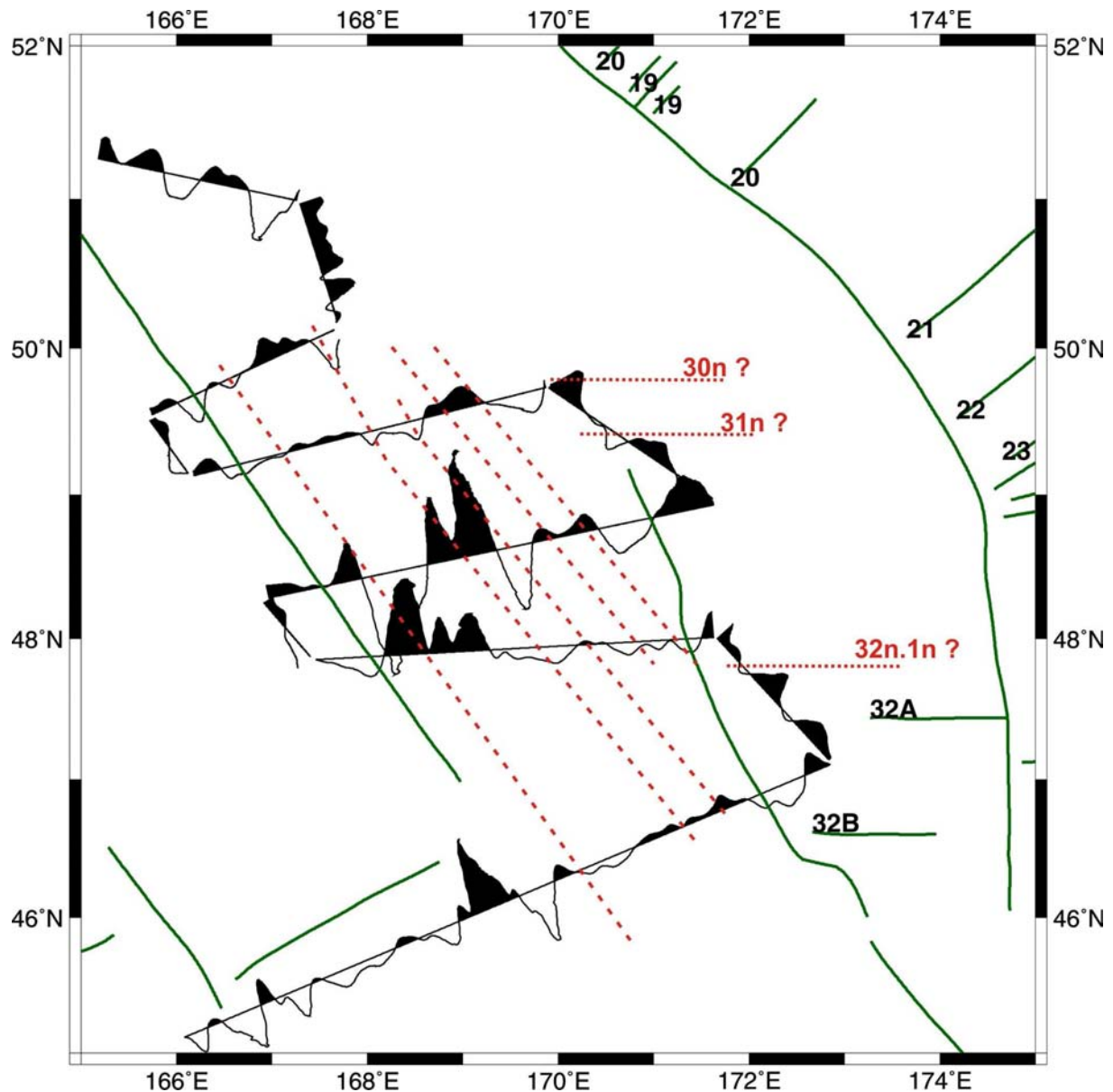


Fig. 1.16.5: Magnetic anomalies along ship tracks of cruise SO-201 over the Emperor seamounts shown as wiggles. Green lines are magnetic lineations after Cande et al. (1989). Numbers indicate magnetic chrons. Red dotted lines show seafloor spreading lineations according to Fig. 7.4.4, red dashed lines tentatively indicate possible correlations of magnetic anomalies in the oceanic crust underlying the seamount chain. These cannot be age dated as seafloor spreading anomalies.

1.17 Gravity data: description and preliminary interpretation

I. Heyde

1.17.1 Gravity database

Gravity measurements were carried out continuously during the cruise. Therefore gravity data along all 15 profiles with a total length of 5894 km were measured. In addition about 1000 km were measured along transits. The distribution of the survey profiles can be seen in the track chart in Fig. 4.1.1. Despite the sparse coverage of the survey area a map of the free-air gravity anomalies was prepared (Fig. 1.17.1).

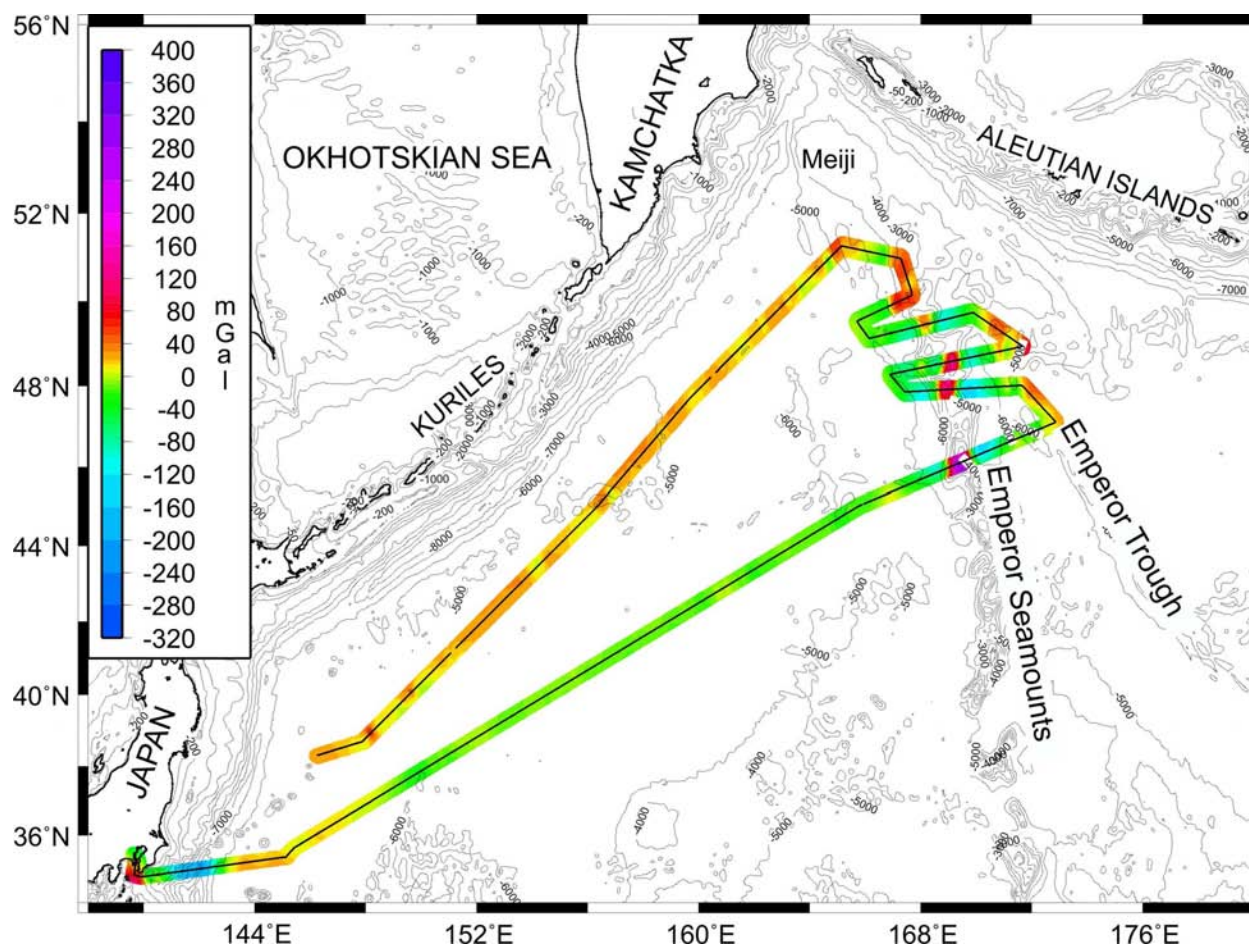


Fig. 1.17.1: Map of the free-air gravity anomalies in the survey area of cruise SO-201. The map is drawn up to a distance of 25 kilometres from the tracks. The map is based on a 1 x 1 (arc-)minutes grid and it is underlain by the bathymetry of Andersen et al. (2008).

1.17.2 Comparison with gravity anomalies derived from satellite altimetry

The analysis of crossover errors during many former cruises shows that our gravity measurements are far more precise than alternate methods to measure the marine gravity field such as the calculation of free-air gravity anomalies from satellite altimeter measurements. A satellite altimeter uses a pulse-limited radar to measure the altitude of the satellite above the closest point to the sea surface. Global precise tracking coupled with dynamic orbit calculations provide an independent measurement of the height of the satellite above the ellipsoid. The difference between these two measurements is equal to the geoid height. In marine areas the free-air anomaly can be calculated from the slope of the geoid. Closely spaced satellite altimeter profiles collected during the GEOSAT Geodetic Mission (~ 6 km) and the ERS 1 Geodetic phase (~ 8 km) were used by different groups to calculate grids of the free-air gravity anomalies.

Our data set can serve as a reference for the comparison of two different satellite gravity data compilations. The first is the one from Sandwell and Smith (1997), version 16.1, referred to as SDW16.1 in the following. The second data set is from the DTU Space Center, Copenhagen (Andersen et al., 2008) referred to as DNSC08 here. Andersen and colleagues (2008) implemented a new technique for the interpolation of the gravity field called adaptive interpolation. With adaptive

interpolation the parameters for the covariance function have been determined empirically from the altimetry and subsequently interpolated to the position of interpolation. This has shown to be efficient in removing track-like structures in areas of high ocean variability as the variance is much better determined.

Subtracting the 1 x 1 minute grid of the SDW16.1 and DNSC08 data from the 1 x 1 minute grid of the shipboard data one obtains the maps of the differences shown in Fig. 1.17.2. The maps are masked beyond a distance of 3 kilometres from the SO-201 profiles. The differences of both datasets range between +10 and -14 mGal, but the differences are below ± 4 mGal along most tracks. There is no pronounced areal distribution of the differences, but of course they increase rapidly away from the track where seamounts are crossed.

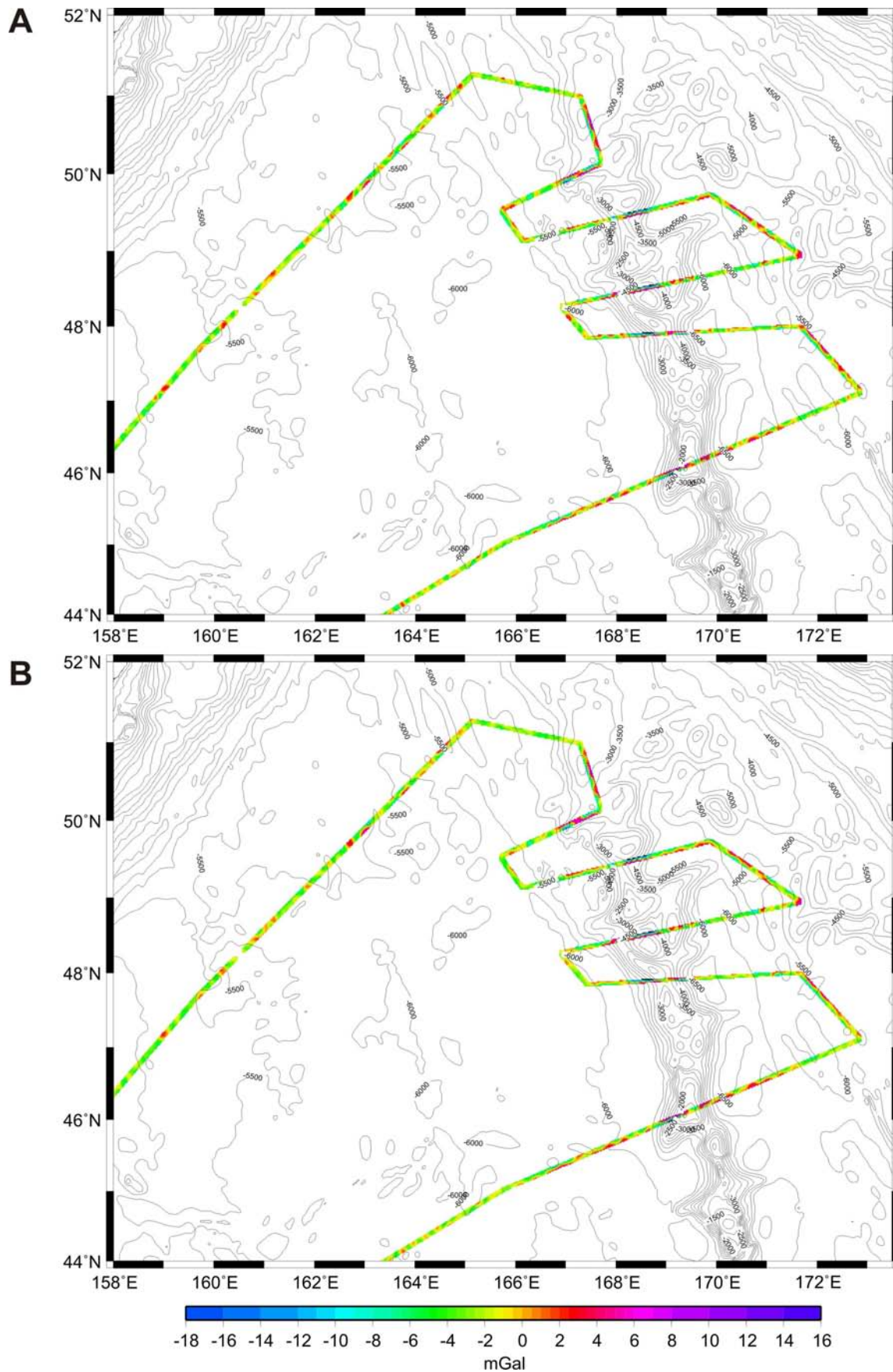


Fig. 1.17.2: Differences of the shipboard free-air gravity data and the gravity datasets derived from satellite altimetry (**A:** Sandwell and Smith (1997), version 16.1; **B:** Andersen et al. (2008), DNSC08).

Satellite gravity anomalies along the complete track were additionally calculated with bicubic interpolation out of the 1 x 1 minute grids and subtracted from the shipboard data (Fig. 1.17.3). The mean differences are nearly the same (DNSC08: -2.10 mGal; SDW16.1: -2.07 mGal). However, the standard deviation is lower for the DNSC08 data (1.88 mGal vs. 2.09 mGal). Considering the standard deviation as the main criteria, the above statistical results helped us to decide to use the DNSC08 data set for further gravity map compilations in areas where no SO201 shipboard data were measured. The difference of about 2 mGal between the ship data and both satellite data sets may be caused by the drift of the gravity meter. Another explanation would be an offset of the gravity reference station with regard to the satellite data. This will be clarified after the cruise.

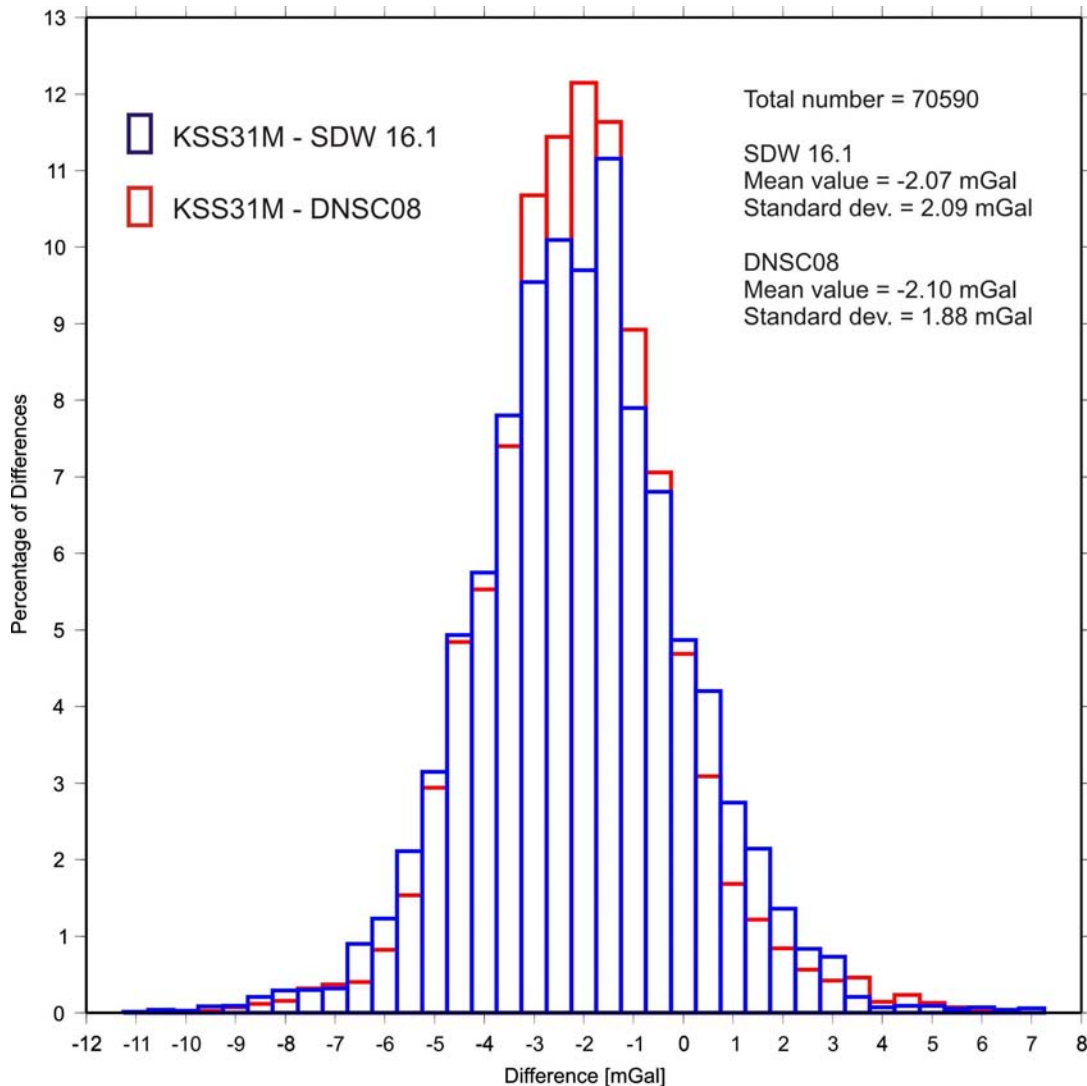


Fig. 1.17.3: Histogram of differences between shipboard KSS31M free-air gravity anomalies and the corresponding gravity datasets derived from satellite altimetry.

To illustrate the differences between the data sets in detail, Fig. 7.5.4 shows exemplary a comparison along profile BGR09-112. The wavelength range of satellite and shipboard anomalies is comparable. In oceanic areas with nearly flat sea-floor the satellite data show oscillations with a wavelength of about 25 km and amplitudes of ± 3 to 5 mGal which do not correlate with anomalies in the shipboard data. We consider these differences to represent the error in the satellite data.

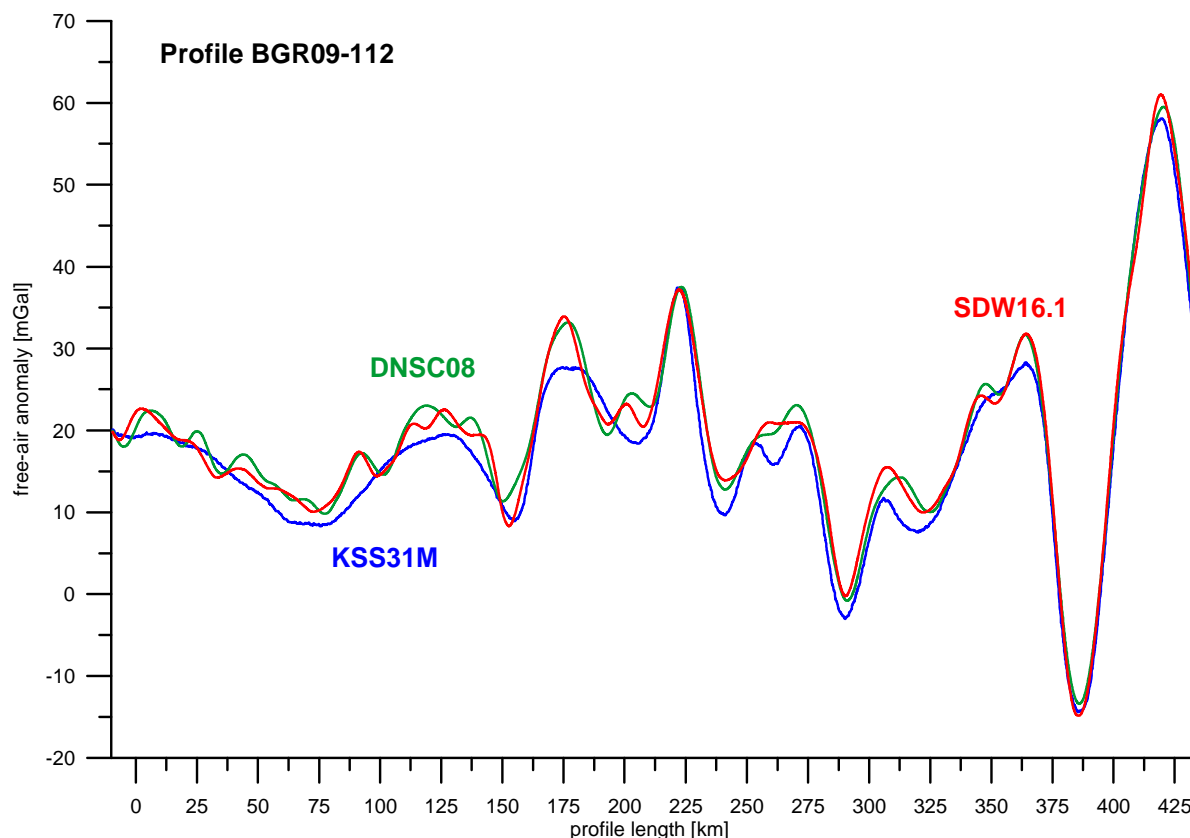


Fig. 1.17.4: Comparison of the ship-based KSS31M and satellite (DBSC08 and SDW16.1) free-air gravity anomalies along profile BGR09-112.

To conclude the free-air gravity anomalies derived from satellite altimetry are of great importance to get an overview of the gravity field in an oceanic area. For detailed investigations, however, shipboard gravity measurements are indispensable.

1.17.3 Gravity anomaly maps

Combined free-air gravity map

In order to get a complete idea of the gravity field in the survey area DNSC08 gravity data were included in areas with no SO-201 shipboard data for the compilation of the free-air gravity map shown in Fig. 7.5.5. A constant value of 2 mGal was subtracted from the DNSC08 data. Shipboard data of other cruises were not considered yet.

The gravity map is dominated by the anomalies of the main topographic features in the survey area. The oceanic crust in the SW is characterized by free-air anomalies between -30 to $+10$ mGal. The water depth is uniformly about 5500 to 6000m. Towards the NW the free-air gravity values increase to 60 - 80 mGal. However, isostasy requires that normal oceanic crust does not cause large free-air gravity anomalies. This is confirmed by worldwide observations of marine gravity. The positive free-air anomalies result from the influence of the subduction bulge due to the downgoing lithosphere of the Pacific plate. Narrow NW-SE or SW-NE trending gravity minima can be correlated with fault zones. However, only the fault zones from the seafloor-spreading world map of Cande et al. (1989) are shown in the map. Landward, an about 100 km wide negative anomaly runs from SW to NE, which gravity values decreasing down to -320 mGal. They reflect the Kuril-Kamchatka

trench with water depths of more than 8000 m. Further towards the coast the gravity values increase rapidly with decreasing water depth.

The oceanic crust in the SE is characterized by more variable gravity anomalies between -100 to +80 mGal. In addition to the positive effect of the subduction bulge, higher gravity values can be correlated with topographic highs like seamounts. Low values reflect bathymetric lows like the Emperor trough or a distinct NW-SE trending fault zone further north. An about 75 km wide negative anomaly running from NW to SE reflects the Aleutian trench with water depths of 7000 m. Northward the values increase rapidly with decreasing water depth towards the Aleutian islands.

The most prominent feature on the oceanic crust is the NNW-SSE trending chain of 30 to 70 km wide gravity maxima of up to 300 mGal caused by the Emperor seamounts with heights of up to 5000 m. The gravity maxima are accompanied by 80 to 100 km wide gravity lows on both sides of the seamount chain. They reflect the flexure of the lithosphere due to the additional mass of the volcanic load. The flexural rigidity of the lithospheric plate results in a regional isostatic compensation and in an increase of the water depth of about 500 m. The northward extension is not formed by individual seamounts but by the broad Obruchev Rise and Meiji Rise close to the triple junction.

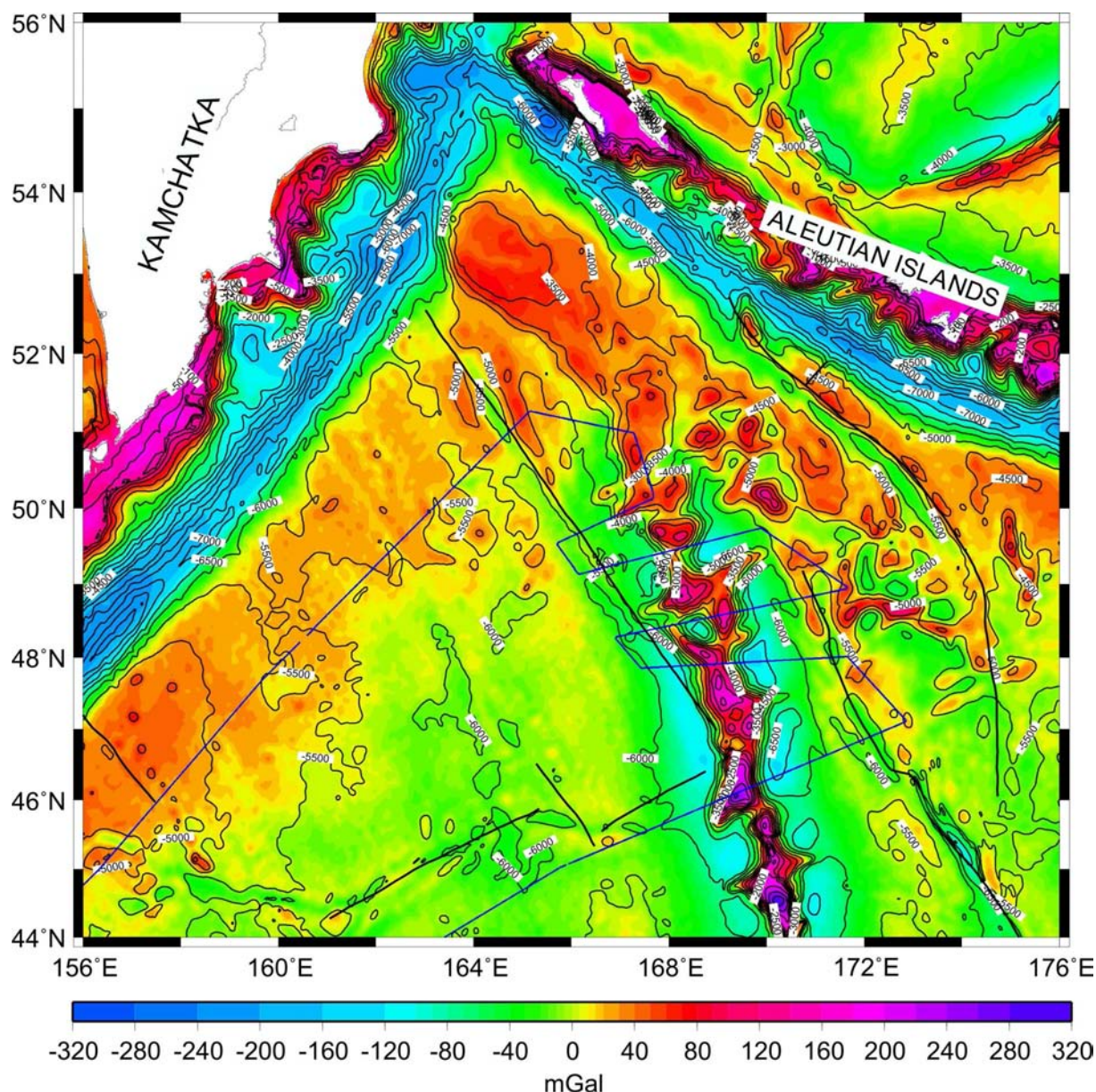


Fig. 1.17.5: Free-air gravity anomaly map. The underlying grid of gravity was compiled by merging SO-201 gravity observations and DNSC08 gravity data derived from satellite altimetry. Fault zones of Cande et al. (1989) are marked black, the ship track blue. The map is based on a 1 x 1 (arc-)minutes grid and is underlain by the bathymetry from Andersen et al. (2008)

Bouguer gravity anomaly map

The underlying grid of gravity was compiled by merging SO-201 gravity observations and DNSC08 satellite gravity data (Fig. 1.17.6). The water depth values were taken from the ship's echo sounding system and from the DNSC08 bathymetry data (Andersen et al. 2008) where no echo sounder depths were available. The reduction density was 1.64 g/cm³ and an infinite horizontal slab was assumed. A topographic reduction was not performed. On the oceanic crust the anomalies are positive (up to +440 mGal) with a smooth increase of values both to the SW and to the East. Bathymetric lows like the Emperor Trough show the highest gravity values. The Emperor seamounts, especially the Detroit Tablemount and the Obruchev/Meiji Rise

are characterised by lower Bouguer gravity values indicating a thicker cover of lower density material. Landward the values decrease rapidly.

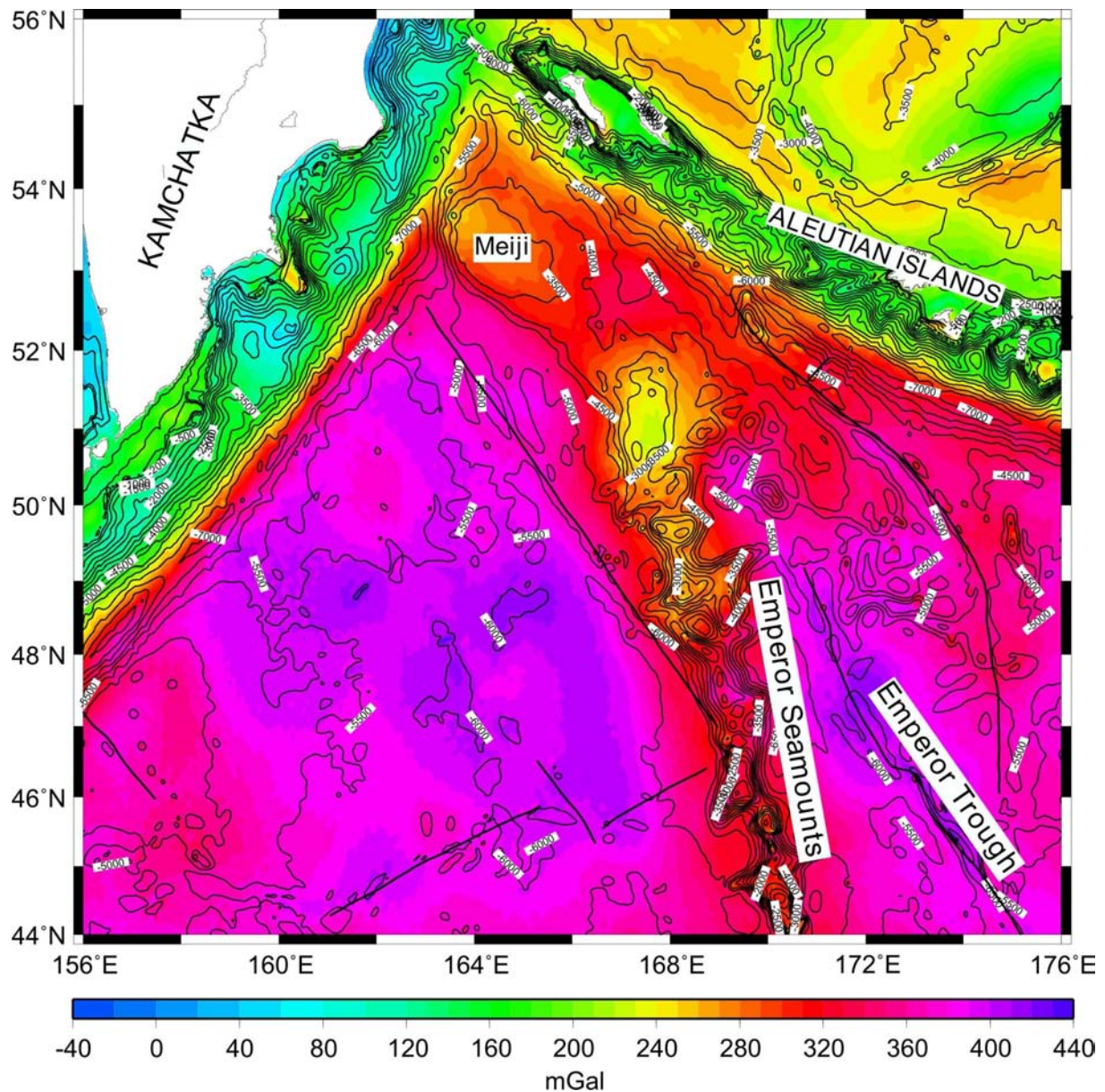


Fig. 1.17.6: Map of Bouguer gravity anomalies. The reduction density was 1.64 g/cm³. The map is underlain by the bathymetry from Smith and Sandwell (1997), version 9.1.

1.17.4 Interpretation by forward modeling

The mostly elongated structure of the free-air gravity anomalies in a NNW-SSE direction suggests that the forward modeling of the free-air anomalies can be carried out two-dimensionally. The gravimetric 2D models represent first approaches to explain the observed free-air gravity anomalies and form the basis of a comprehensive 3D density model which will be developed after the cruise.

2D forward modeling of the free-air anomalies was carried out with the software GM-SYS (Northwest Geophysical Associates, Inc.) along the four profiles which cross the seamounts completely. The corresponding results of the MCS interpretation were

taken into account. The interpretation of the MCS data was based on time-stacked data. These time sections yield valuable information about the upper subsurface structures. The depth of prominent horizons was calculated by using mean interval velocities. Furthermore, the velocities can be converted to density with density-velocity relations such as the extended Nafe and Drake relation (Ludwig et. al., 1970). Two density models developed on SW-NE running profiles that cross the main units of our survey area are presented in the following.

BGR09-101

The southernmost Profile BGR09-101 is about 570 km long and crosses Jimmu Guyot and the Emperor Trough from SW to NE. Fig. 7.5.7 shows the density model resulting from the 2D forward modeling of the free-air gravity anomalies. The oceanic crust is divided in two layers ($\rho_1=2.8 \text{ g/cm}^3$ and $\rho_2=2.95 \text{ g/cm}^3$) with total thickness of about 6 km. The layer boundary was recognised in the MCS data on BGR09-109 and used in all models. The Moho position at 12.5 km in the SW follows the MCS interpretation. The crust is overlain by 200 to 400 m of sediments, which can be divided in pelagic sediments of low density ($\rho=2 \text{ g/cm}^3$) and a volcanoclastic sequence of higher density ($\rho=2.4 \text{ g/cm}^3$). The geometry was taken from the seismic interpretation. The Jimmu Guyot ($\rho_1=2.85 \text{ g/cm}^3$ and $\rho_2=2.95 \text{ g/cm}^3$) with a height of nearly 5 km causes a gravity anomaly of more than 300 mGal. The division into two basalt units is necessary to explain the central absolute gravity maximum. That is supported by the inhomogeneous magnetic properties required to explain the measured magnetic field. The flexure of the oceanic crust due to the load of the seamount results in sedimentary basins of 1.5 to 2 km thickness, with the eastern one being considerably deeper. The up to 6 km thick root of the seamount is asymmetrical with its deeper part in the E. Deep crustal sill complexes as proposed by Watts et al. (1985) for Hawaiian seamounts were not considered yet. The Emperor Trough is characterised by two sediment-filled depressions separated by a high. A change of the thickness and/or density of the oceanic crust layers is not necessary to explain the measured gravity anomalies.

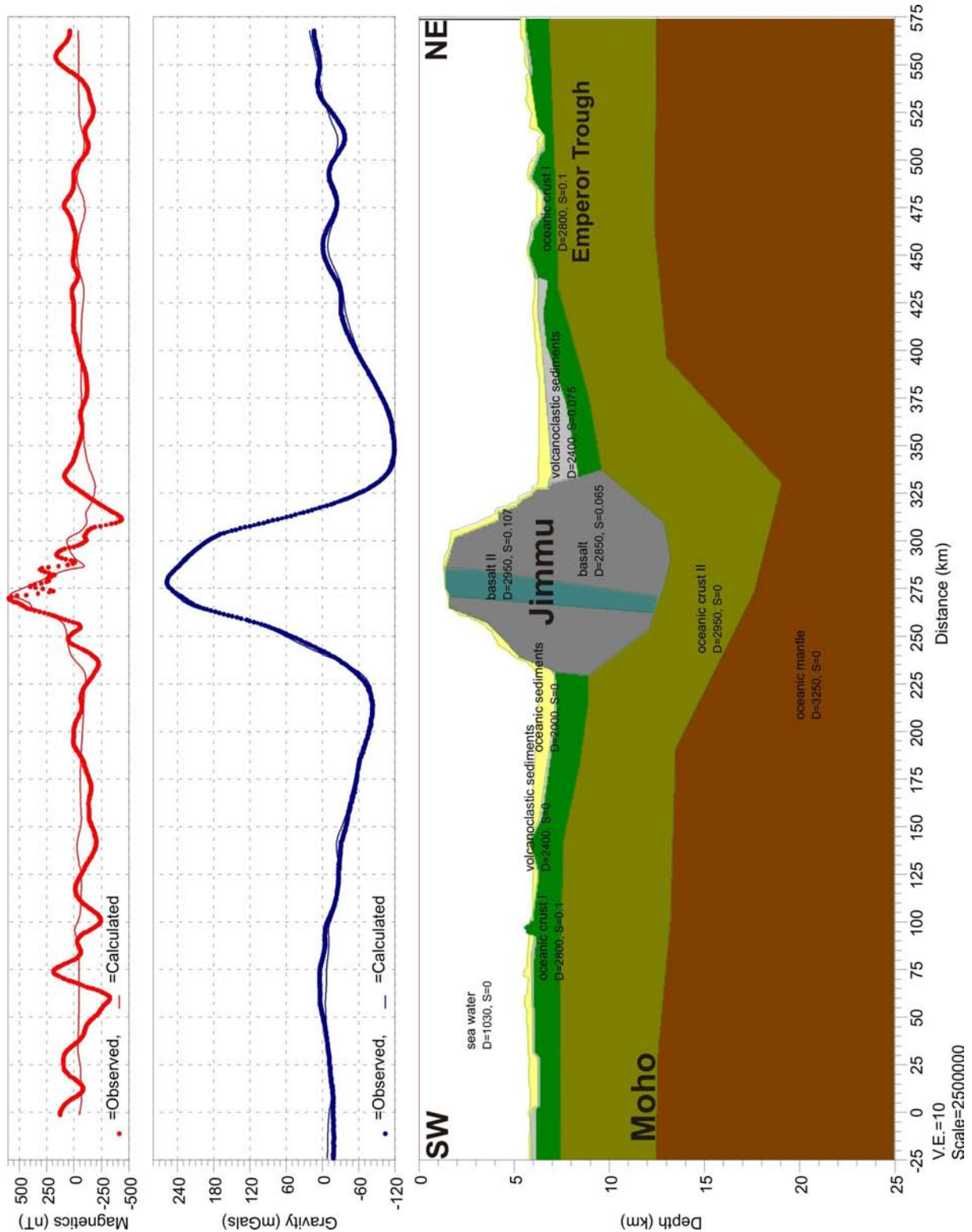


Fig. 1.17.7: 2D density model explaining the free-air gravity anomalies along BGR09-101. Dotted lines: observed anomalies; Continuous line: calculated anomalies. Density values are given in kg/m³, susceptibilities in SI units.

BGR09-107

BGR09-107 is located about 380 km to the N of profile BGR09-101. It has a length of 280 km and crosses the Emperor Seamount Chain north of Tenji Guyot. Fig. 6.5.8 shows the preliminary density model resulting from the 2D forward modeling of the free-air gravity anomalies. Density values of the structural units are taken from the previous model. The Moho is shallower in the SW than in the previous model but is in accordance with the MCS interpretation on the northward following profiles BGR09-108 and -109. The seamounts are not crossed at their maximal elevation so the gravity anomaly is only about 90 mGal. The up to 6 km thick root of the seamount is asymmetrical with its deeper part in the E. The adjacent basins filled with volcanoclastic and pelagic sediments are deeper (up to 2.6 km) than on the southernmost profile. Their geometry was taken from the MCS interpretation. In order to explain the trend of the gravity anomalies towards the SW the oceanic crust needs to thin out to 4 to 5 km.

The presented density models will change when further interpreted and depth-migrated MCS data become available. But already now they provide some information concerning the thickness and density of the structural units of the northwestern part of the Pacific plate.

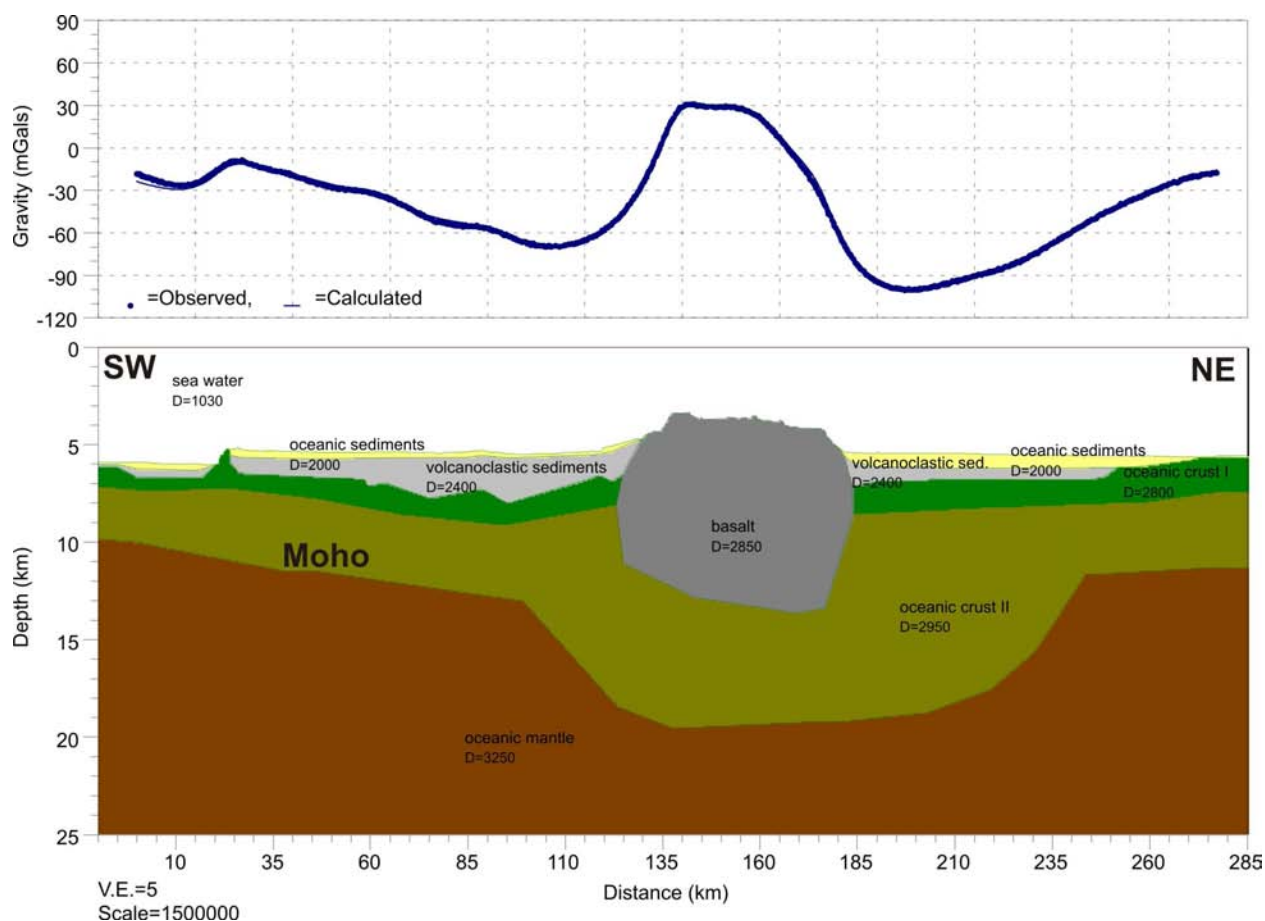


Fig. 1.17.8: 2D density model explaining the free-air gravity anomalies along BGR09-107. Dotted lines: observed anomalies; Continuous line: calculated anomalies. Density values are given in kg/m^3

ACKNOWLEDGEMENTS

We are grateful to Master Lutz Mallon and his crew for excellent cooperation and support during the cruise.

We acknowledge the participating of scientists from Russia. They contributed greatly to the success of the cruise.

Cruise SO 201 Leg 1a KALMAR was funded by the German Ministry of Education and Research (BMBF) under project No. 03G0201B. We gratefully acknowledge the continuous support for the marine sciences with the outstanding research vessel SONNE.

REFERENCES

- ANDERSEN, O.B., KNUDSEN, P., BERRY, P. AND KENYON, S., 2008: The DNSCO8 ocean wide altimetry derived gravity field. Presented EGU-2008, Vienna, Austria, April, 2008.
- BARGAR, K.E. & JACKSON, E.D. (1974): Calculated volumes of individual shield volcanoes along the Hawaiian–Emperor Chain. U.S. Geol. Surv. J. Res. 2, pp. 545–550.
- CANDE, S.C., & KENT, D.V. (1995) Revised calibration of the geomagnetic polarity time- scale for the Late Cretaceous and Cenozoic, J. Geophys. Res., 100, pp. 6093-6095.
- CANDE, S.C., LABRECQUE, J.L., LARSON, R.L., PITMAN, W.C., GOLOVCHENKO, X., & HAXBY, W.F., 1989: Magnetic lineations of the world's ocean basins. LDGO contribution 4367, AAPG, Tulsa, Oklahoma.
- DUNCAN, R.A. & KELLER, R.A., 2004. Radiometric ages for basement rocks from the Emperor Seamounts, ODP Leg 197. *Geochem., Geophys., Geosyst.*, 5(8):Q08L03.
- EILERS, G., ROESER, H.A. & KEWITSCH, P. (1994) Reduktion geomagnetischer Variationen durch ein Gradientenmagnetometer: BGR-Report 110.615, pp. 1-73.
- ENGELS, M., BARCKHAUSEN, U. & GEE, J.S., A new towed marine vector magnetometer: methods and results from a Central Pacific cruise: *Geophys. J. Int.*, 172, pp. 115-129, 2008.
- EILERS, G., ROESER, H.A. & KEWITSCH, P. (1994) Reduktion geomagnetischer Variationen durch ein Gradientenmagnetometer: BGR-Report 110.615, pp. 1-73.
- ENGELS, M., BARCKHAUSEN, U. & GEE, J.S., A new towed marine vector magnetometer: methods and results from a Central Pacific cruise: *Geophys. J. Int.*, 172, pp. 115-129, 2008.
- FREITAG, R., GAEDICKE, C., BARANOV, B. & TSUKANOV, N. (2001): Collisional processes at the junction of the Aleutian–Kamchatka arcs: new evidence from fission track analysis and field observations. *Terra Nova*, 13, pp. 433–442.
- GAEDICKE, C., BARANOV, B., SELIVERSTOV, N., ALEXEIEV, D., TSUKANOV, N. & FREITAG, R. (2000): Structure of an active arc-continent collision area: Aleutian-Kamchatka Junction. *Tectonophysics*, 325, pp. 63-85.
- KELLER, R.A., DUNCAN, R.A., & FISK, M.R. (1995): Geochemistry and $^{40}\text{Ar}/^{39}\text{Ar}$ geochronology of basalts from ODP Leg 145 (North Pacific transect), ODP Sci. Results 145, pp. 333-344
- LUDWIG, J.W., NAFE, J.E., & DRAKE, C.L., 1970: Seismic refraction, in: A.E. MAXWELL (Ed.), *The Sea*, Vol. 4, 53-84, Wiley, New York.
- MAUS, S., MACMILLAN, S., CHERNOV, T., CHOI, S., DATER, D., GLOVKOV, V., LESUR, V., LOWES, F., LÜHR, H., MAI, W., MCLEAN, S., OLSEN, N., ROTHER, M., SABAKA, T., THOMSON, A. & ZVEREVA, T. (2005) The 10th-Generation international Geomagnetic Reference Field: *Geophys. J. Int.*, v. 161, pp. 561–656.
- MAUS, S., BARCKHAUSEN, U., MÜLLER, D. & FAIRHEAD, D. (2008) EMAG2: A 2-arc-minute resolution global magnetic anomaly grid compiled from satellite, airborne

and marine magnetic data, *Eos Trans. AGU*, 89(53), Fall Meet. Suppl., Abstract GP53A-0776.

MIDDLETON, G.V. & HAMPTON, M.A. (1973): Mechanics of flow and deposition. In Middleton, G.V., Bouma, A.H. (eds), *Turbidites and Deep Water Sedimentation*. Society of Economic Paleontologists and Mineralogists Pacific Section Short Course, pp. 1-38.

MORELLI, C., 1974: The International Standardization Net 1971. International Association of Geodesy Special Publication 4, 194.

NARDIN, T.R., HEIN, F.J., GORSLINE, D.S. & EDWARDS, B.D. (1979): A review of mass movement processes, sediment and acoustic characteristics in slope and base-of-slope systems versus canyon-fan-basin floor systems. In DOYLE L.J., PILKEY, O.H. (eds), *Geology of Continental Slopes*. Society of Economic Paleontologists and Mineralogists Special Publication 27, pp. 61-73

SANDWELL, D.T. & SMITH, W.H.F., 1997: Marine Gravity Anomaly from Geosat and ERS-1 Altimetry. *J. Geophys. Res.*, 102, pp. 10039-10054.

SMITH, W.H.F. & SANDWELL, D.T., 1997: Global sea floor topography from satellite altimetry and ship depth soundings. *Science*, 277, pp. 1956-1962.

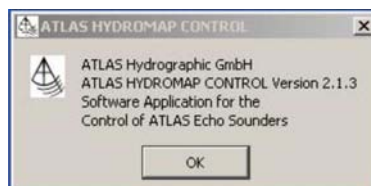
TARDUNO, J.A., DUNCAN, R.A., SCHOLL, D.W., COTTRELL, R.D., STEINBERGER, B., THORDARSON, T., KERR, B.C., NEAL, C.R., FREY, F.A., TORII, M., & CARVALLO, C., (2003): The Emperor Seamounts: southward motion of the Hawaiian hotspot plume in Earth's mantle. *Science*, 301:1064–1069.

WATTS, A.B., TEN BRINK, U.S., BUHL, P., & BROCHER, T.M., 1985: A multichannel seismic study of lithospheric flexure across the Hawaiian-Emperor seamount chain. *Nature*, 315, pp. 105-111.

WORSLEY, T.R. (1973): Calcareous nannofossils, Leg 19 (DSDP). In CREAGER, J.S. & SCHOLL, D.W. (eds.), *DSDP Initial Reports*, 19, pp. 741-750

APPENDIX

1.18 PARASOUND settings during cruise SO201-1a

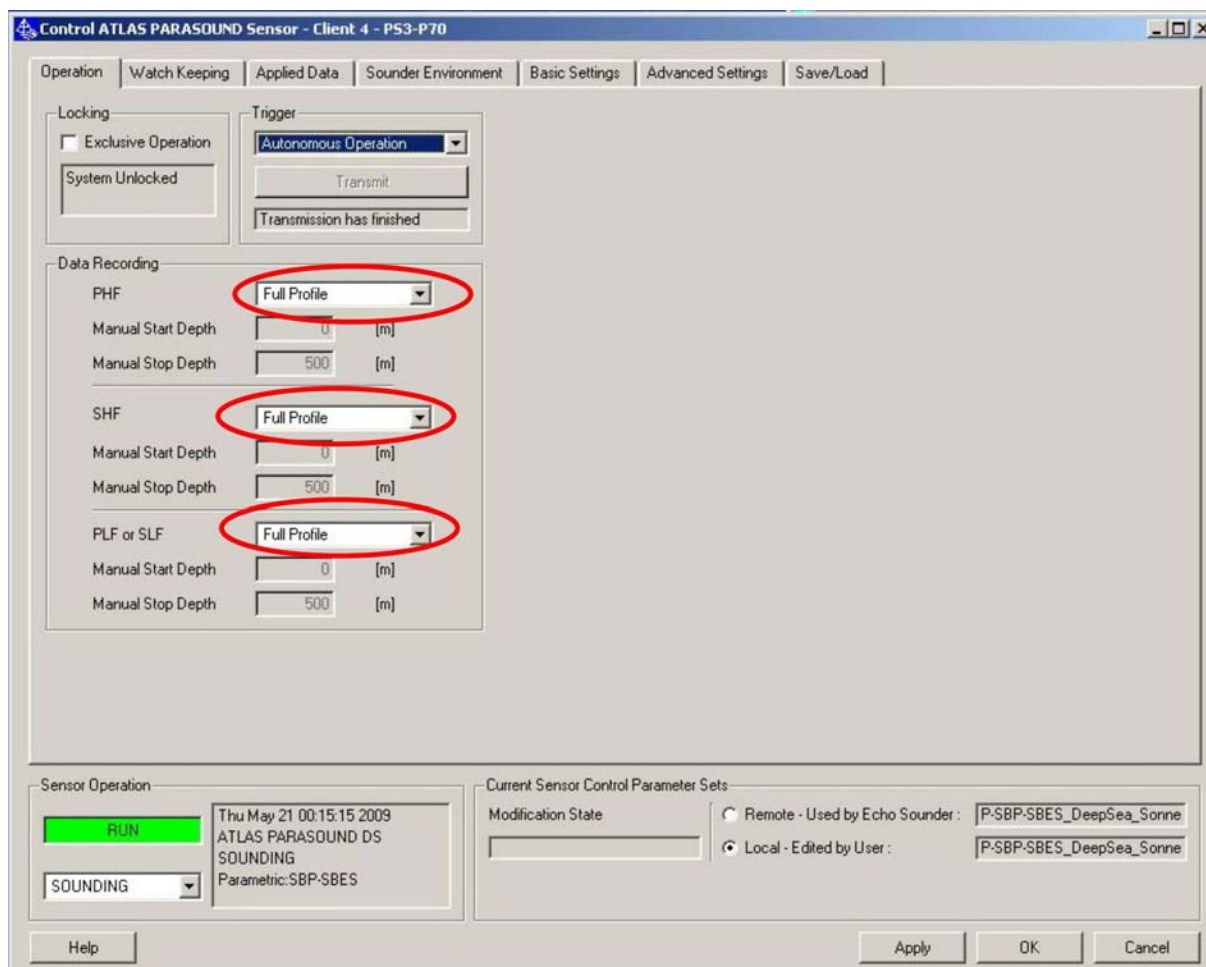


PARASOUND Software installed during SO201-1a: Atlas Hydromap Control, v. 2.1.3

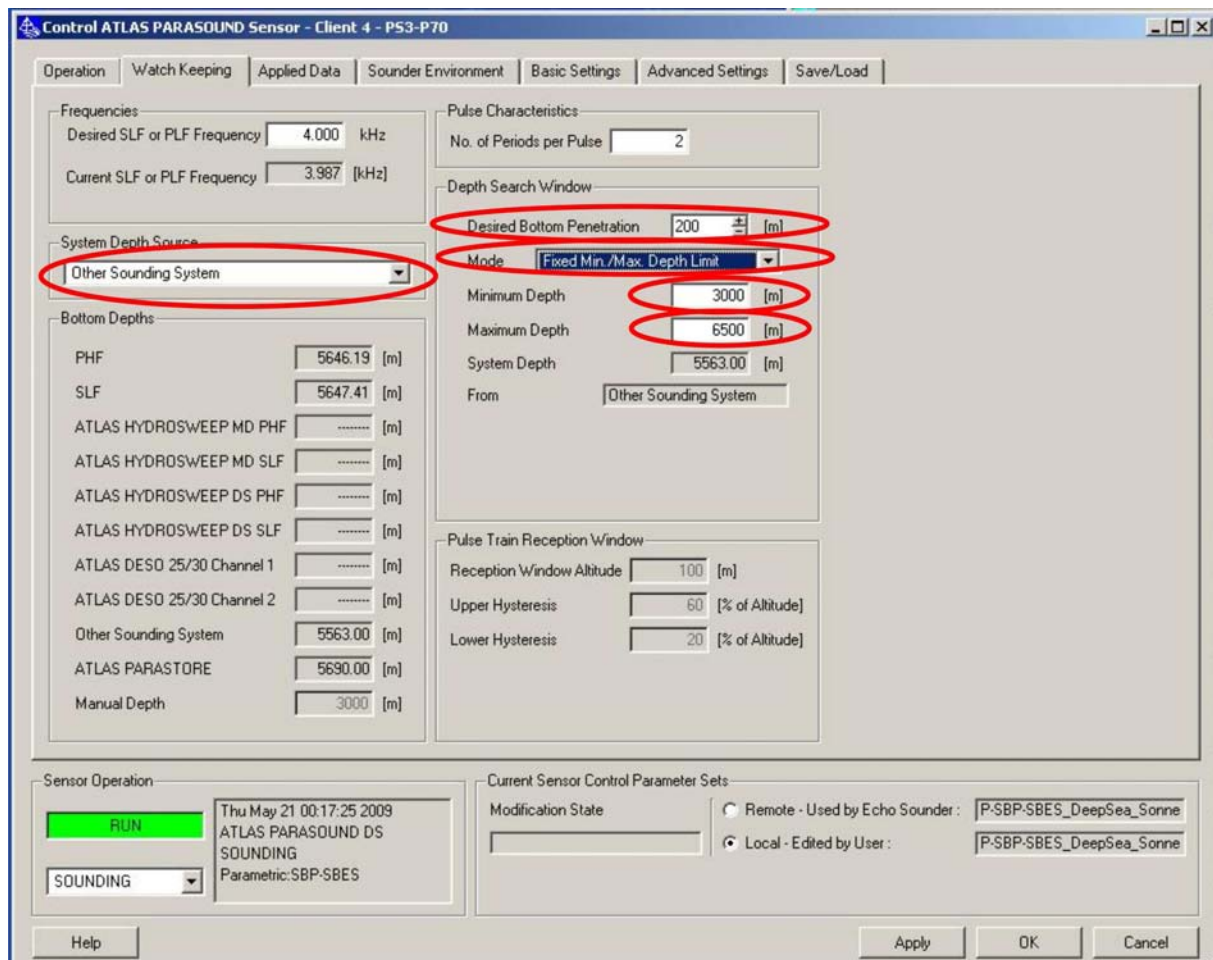


Visualisation software Atlas Parastore, v. 3.2.8

Main settings in HYDROMAP CONTROL



The “Operation” tab in the xxyy window lets you choose which data are recorded. We recorded the full profile including reflections from the water column, the seafloor and subsurface echoes down to approx. 200 m (266 ms) both for the Primary High Frequency beam (PHF, 20 kHz) and for the Secondary Low Frequency beam (SLF, 4 kHz). Make sure to set all options to “Full Profile” and to hit the “Apply” button when you are done.



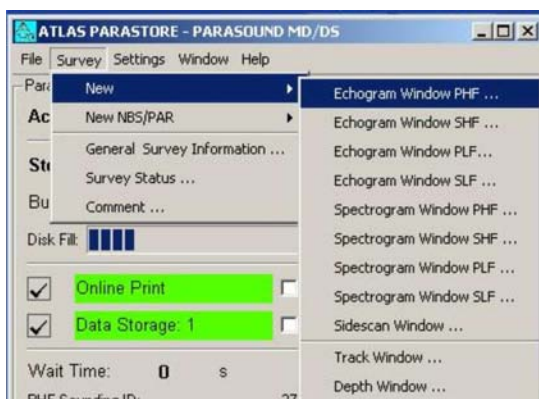
The “Watch Keeping” tab is one of the most important windows. Make sure that the System Depth Source is set to “Other Sounding System”. Parasound will then use the depth from the SIMRAD EM120 system, which is more accurate. “Desired Bottom Penetration” corresponds to the recording time, after the beam intercepts the seafloor bottom. We used 200 m penetration (~ 260 ms recording time). The “Mode” for the Depth Search Window was set to “Fixed Min/Max Depth Limit”, because the automatic setting turned out to be unstable. “Minimum Depth” and “Maximum Depth” must be set manually by the operator/watch keeper. Use an interval of about 3000-4000 m around the anticipated depths.

Main settings in PARASTORE



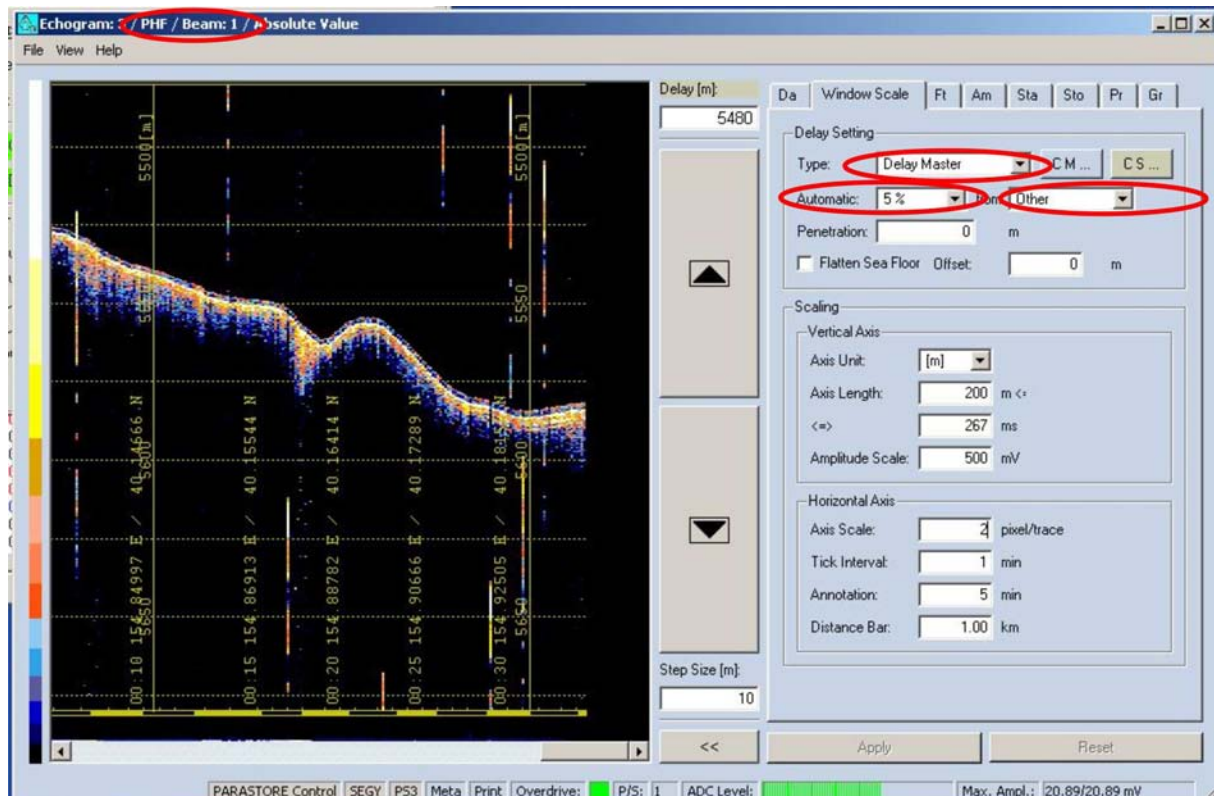
The main Window in PARASTORE gives an overview about the running system. The operator should make sure that “Acquisition” and “Storage” both for PHF and SLF are activated (green). We tried to activate “Online Print” as well, which worked more or less fine for the first 4 days. Later, the printer caused too many errors (timeout), so we switched this function off.

The lower scroll-down window shows errors and warnings and may give some useful hints for trouble shooting.

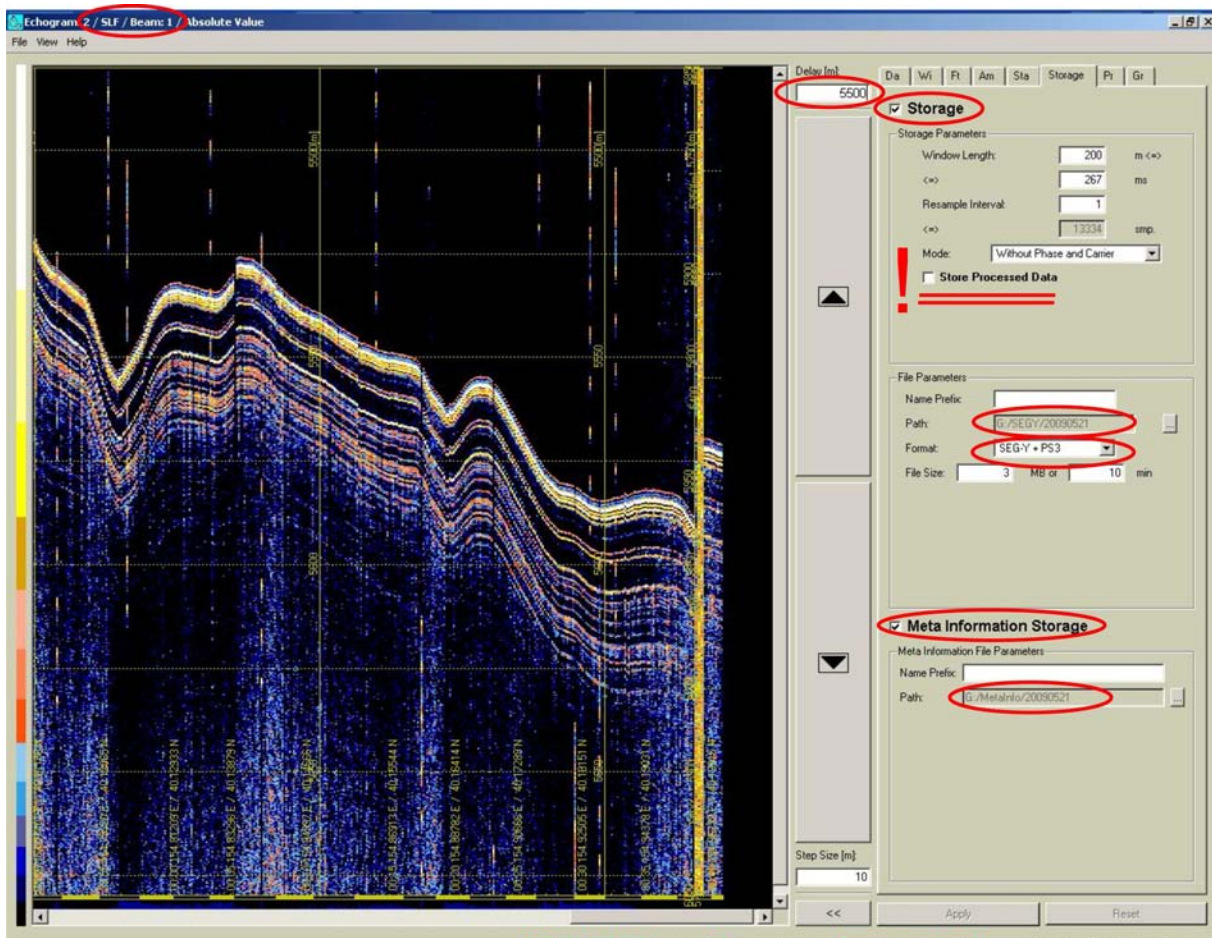


To open a new Acquisition Window choose Survey → New → Echogramm Window

One for PHF and one for SLF...



In the PHF echogram, choose the tab „Wi“ (Window Scale). Set the type of the PHF echograms to “Delay Master”. There is an option called “Automatic” which promises to keep the seafloor at a defined vertical position within the display window. During our tests, the automatic mode did not work! It is necessary to position the seafloor reflection in the display window by manually moving the depth frame up and down using the large arrow buttons.



To open a new echogram window choose “Suryev → New → Echogramm Window” and then SLF-echogramm. Choose the tab “Wi” and set the Delay Setting Type to “Follow Delay Master”. All changes in the master window (PHF) will then automatically be applied to the window for the SLF as well.

In the SLF window, choose the “St” (Storage) – tab. Make sure that “Storage” and “Meta Information Storage” are checked. Verify the paths for data storage. We stored data in SEG-Y and PS3 format for maximum flexibility. **IMPORTANT:** Do NOT check “Store processed data”. If this option is checked, only the data from the display window are stored, including filtering, amplification, etc. You might prefer, as we did, to store the original data and to do all filtering procedures later, after acquisition and shipboard display.

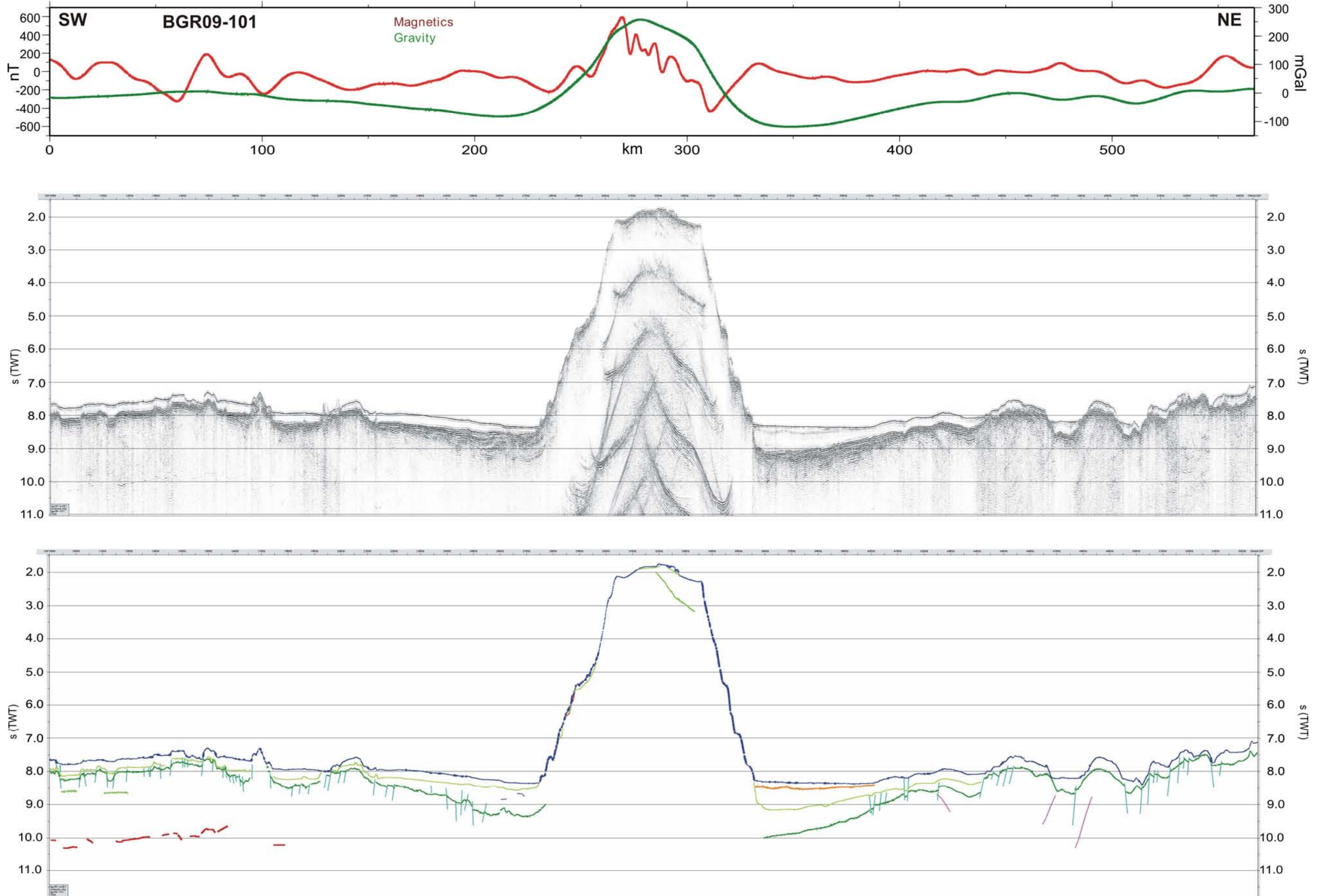


Fig. 1.18.1: Magnetic and gravimetric data, top. MSC profile BGR09-101, CDP spacing 12.5 m, time section, middle. Interpretation of seismic data, bottom.

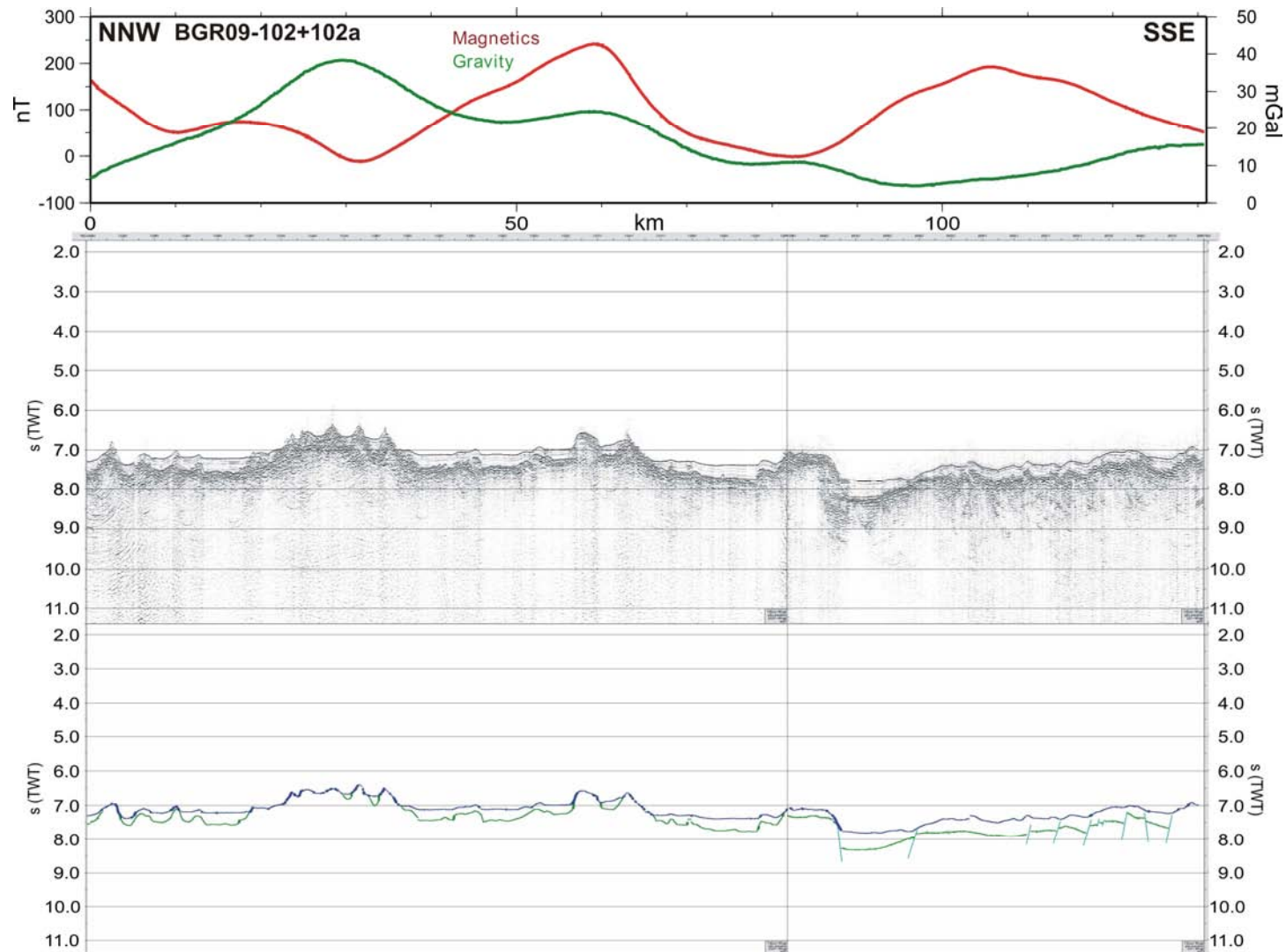


Fig. 1.18.2: Magnetic and gravimetric data, top. MSC profile BGR09-102, CDP spacing 12.5 m, time section, middle. Interpretation of seismic data, bottom.

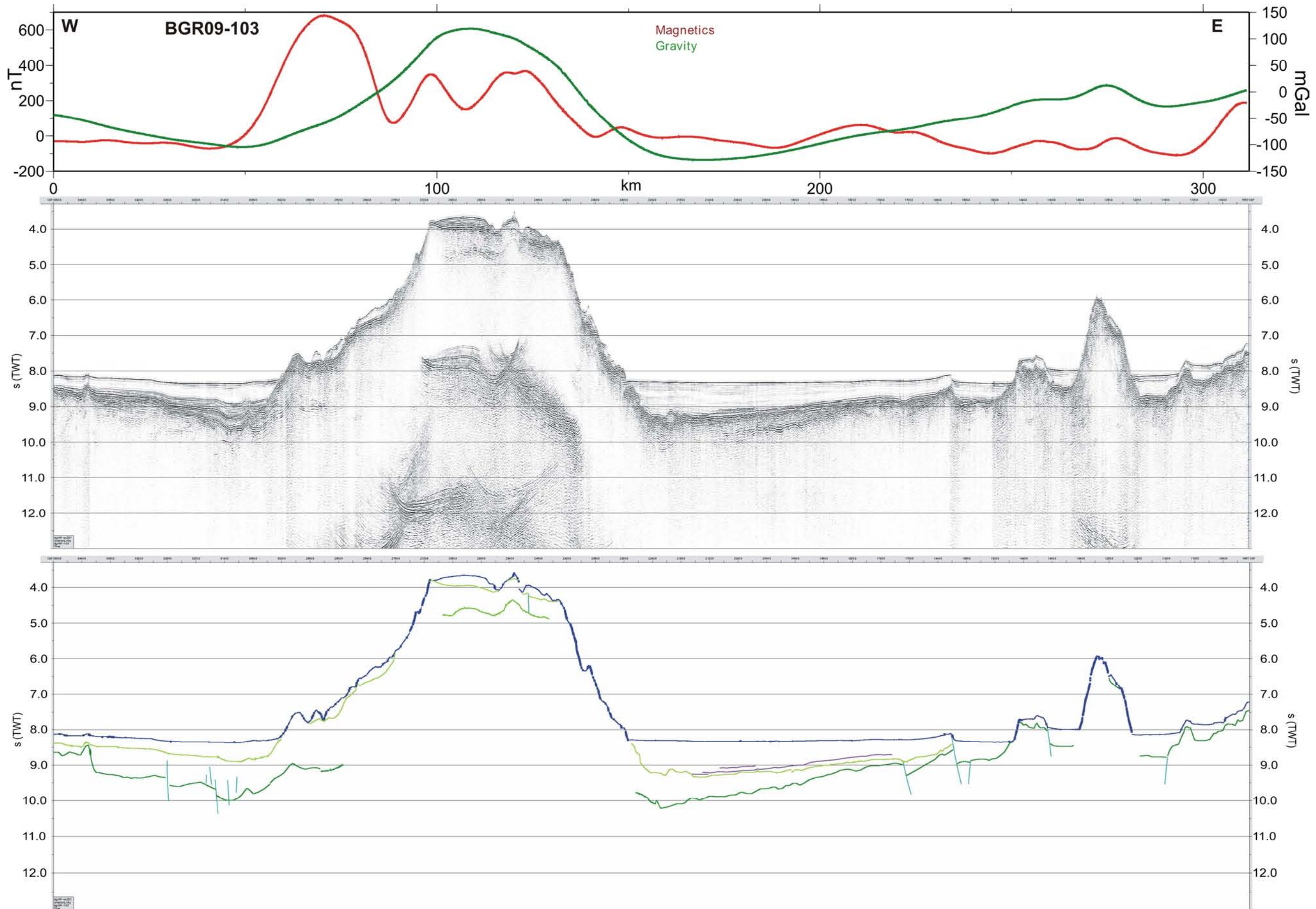


Fig. 1.18.3: Magnetic and gravimetric data, top. MSC profile BGR09-103, CDP spacing 12.5 m, time section, middle. Interpretation of seismic data, bottom.

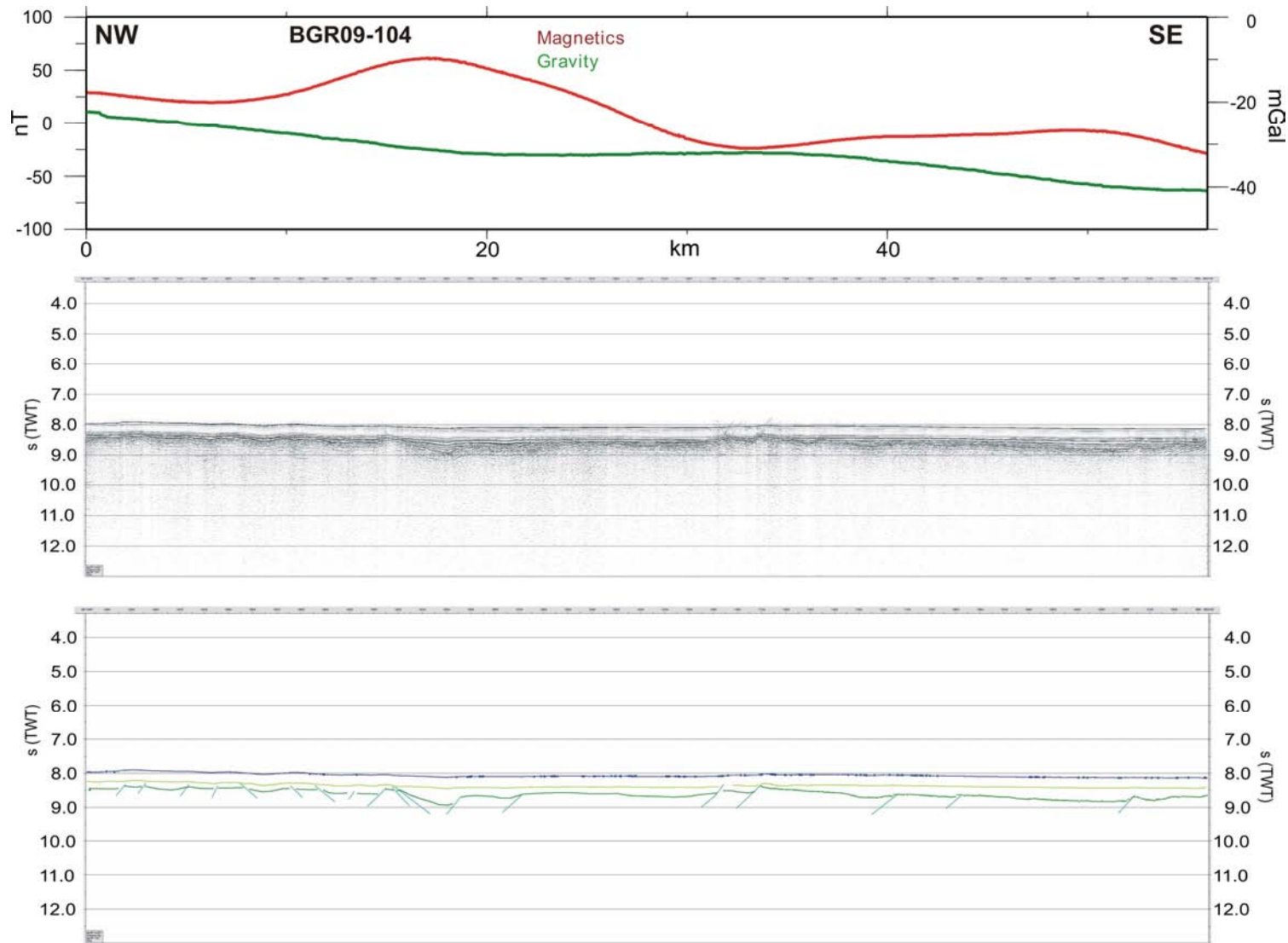


Fig. 1.18.4: Magnetic and gravimetric data, top. MSC profile BGR09-104, CDP spacing 12.5 m, time section, middle. Interpretation of seismic data, bottom.

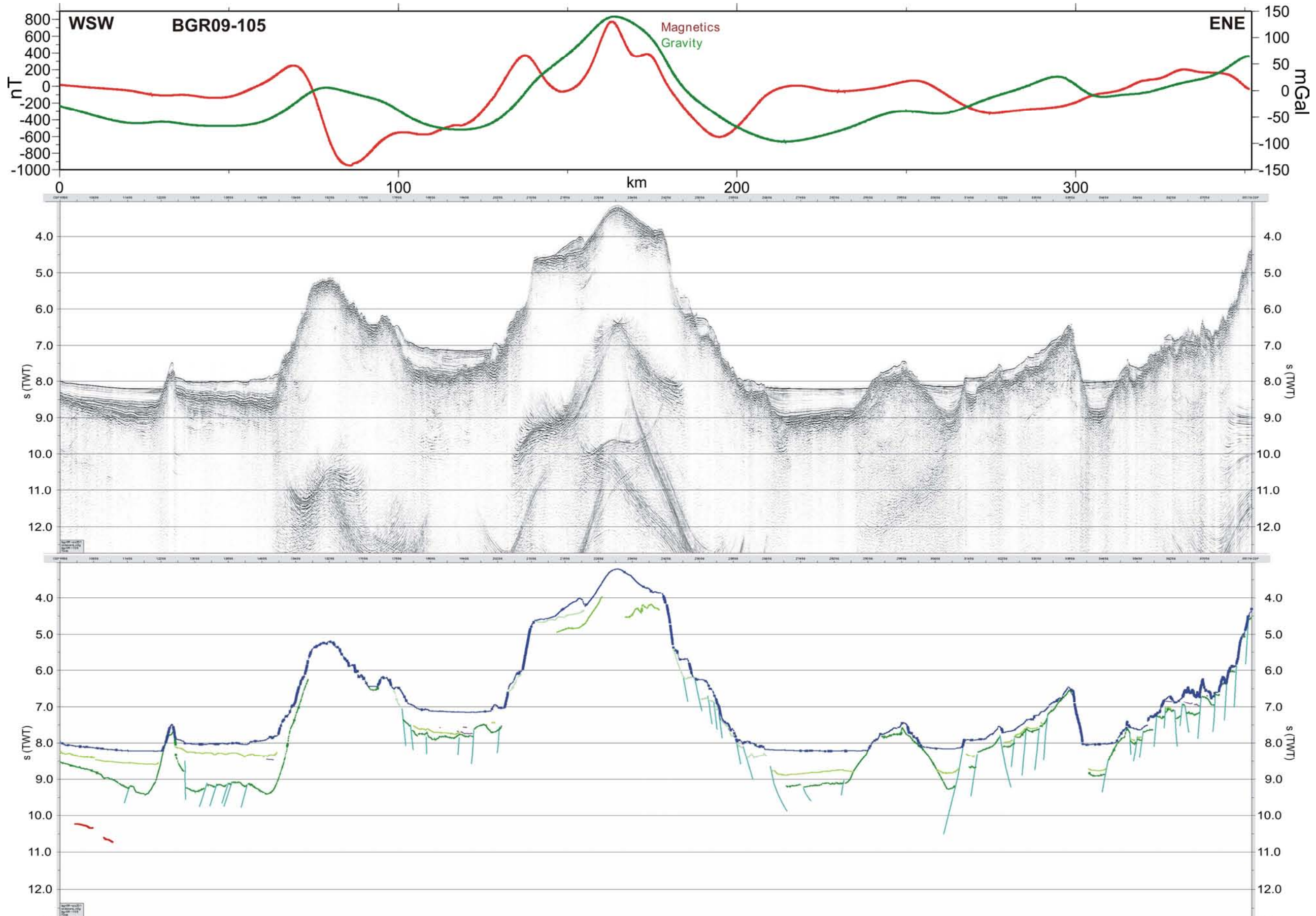


Fig. 1.18.5: Magnetic and gravimetric data, top. MSC profile BGR09-105, CDP spacing 12.5 m, time section, middle. Interpretation of seismic data, bottom.

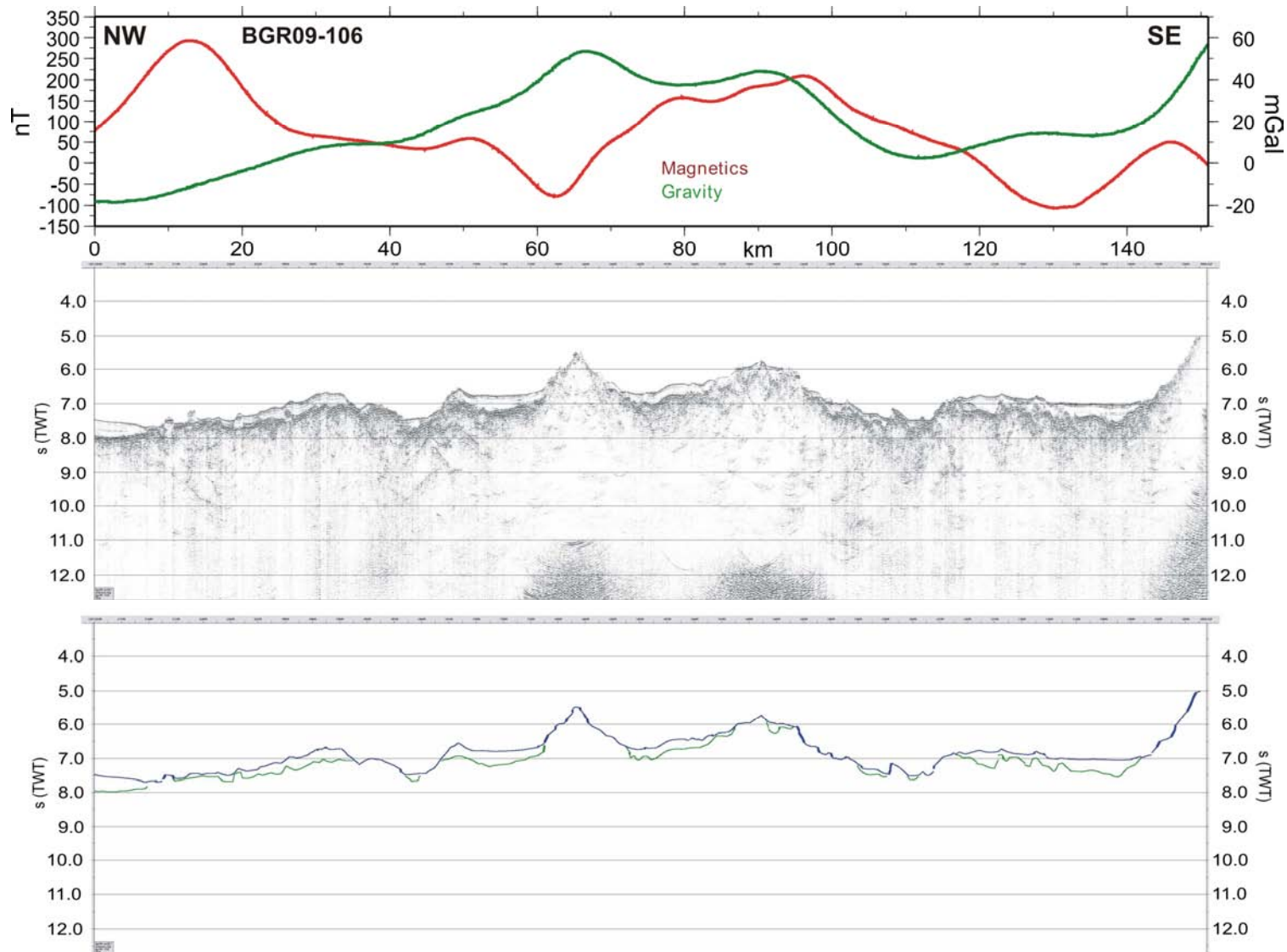


Fig. 1.18.6: Magnetic and gravimetric data, top. MSC profile BGR09-106, CDP spacing 12.5 m, time section, middle. Interpretation of seismic data, bottom.

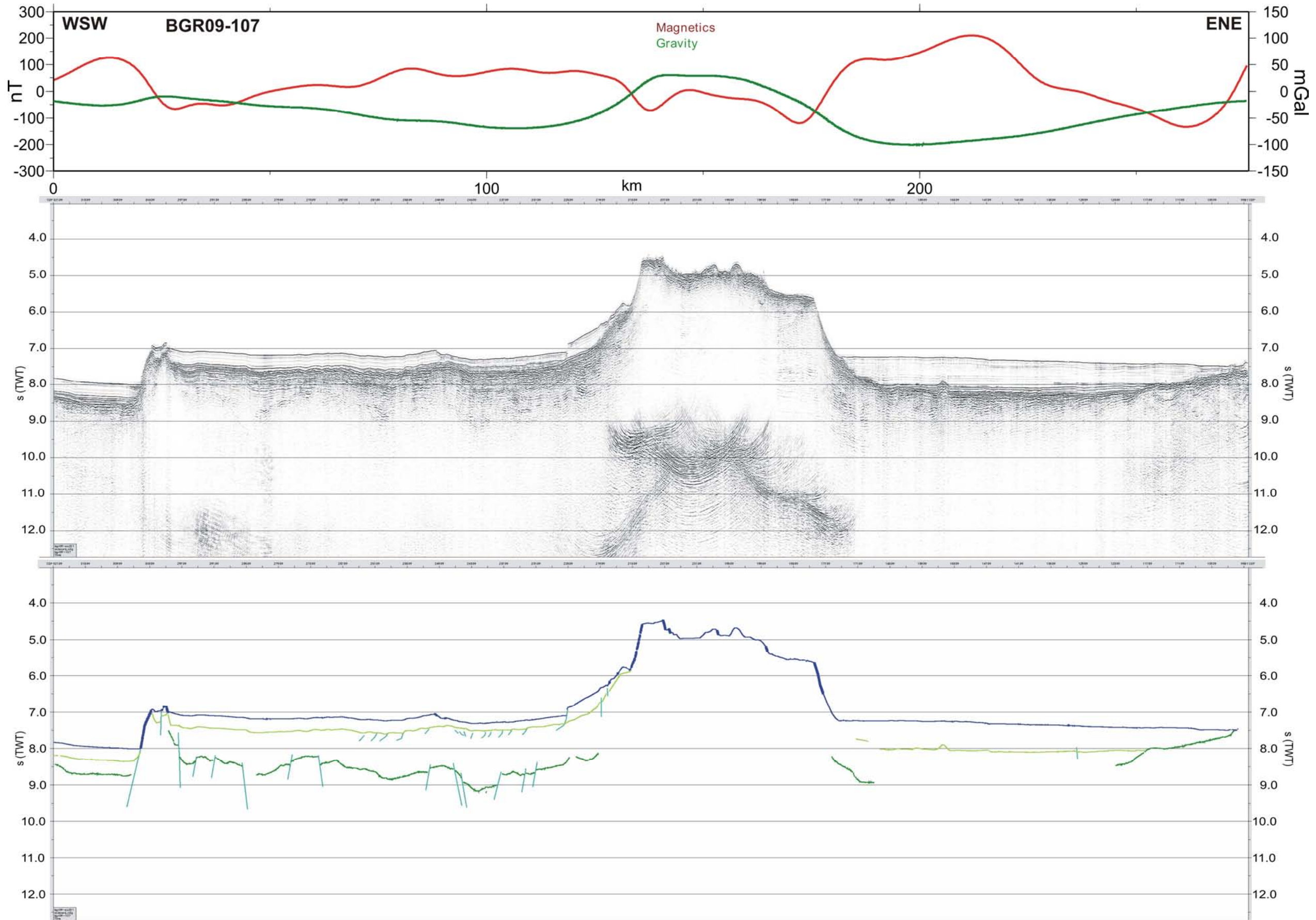


Fig. 1.18.7: Magnetic and gravimetric data, top. MSC profile BGR09-107, CDP spacing 12.5 m, time section, middle. Interpretation of seismic data, bottom.

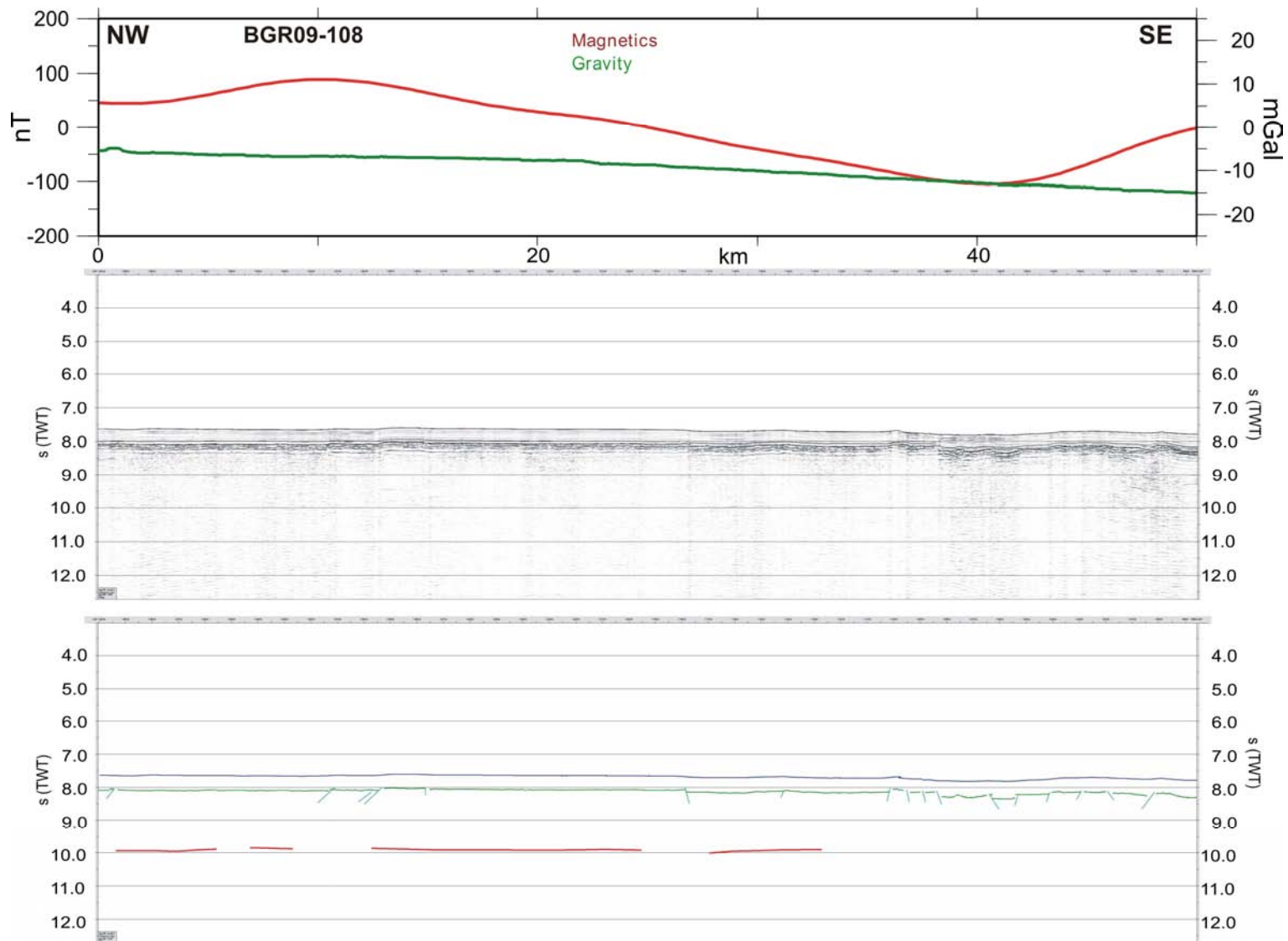


Fig. 1.18.8: Magnetic and gravimetric data, top. MSC profile BGR09-108, CDP spacing 12.5 m, time section, middle. Interpretation of seismic data, bottom.

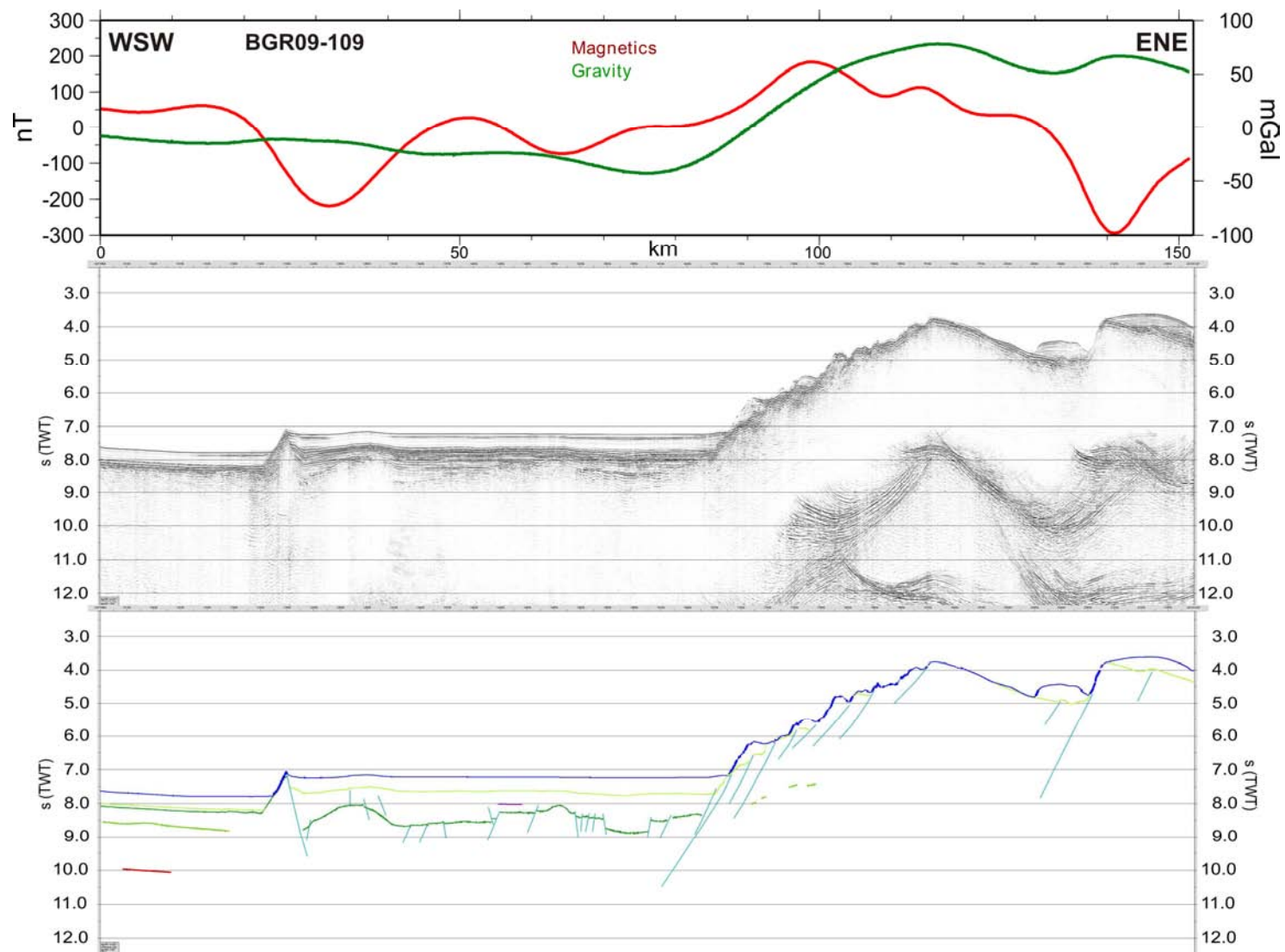


Fig. 1.18.9: Magnetic and gravimetric data, top. MSC profile BGR09-109, CDP spacing 12.5 m, time section, middle. Interpretation of seismic data, bottom.

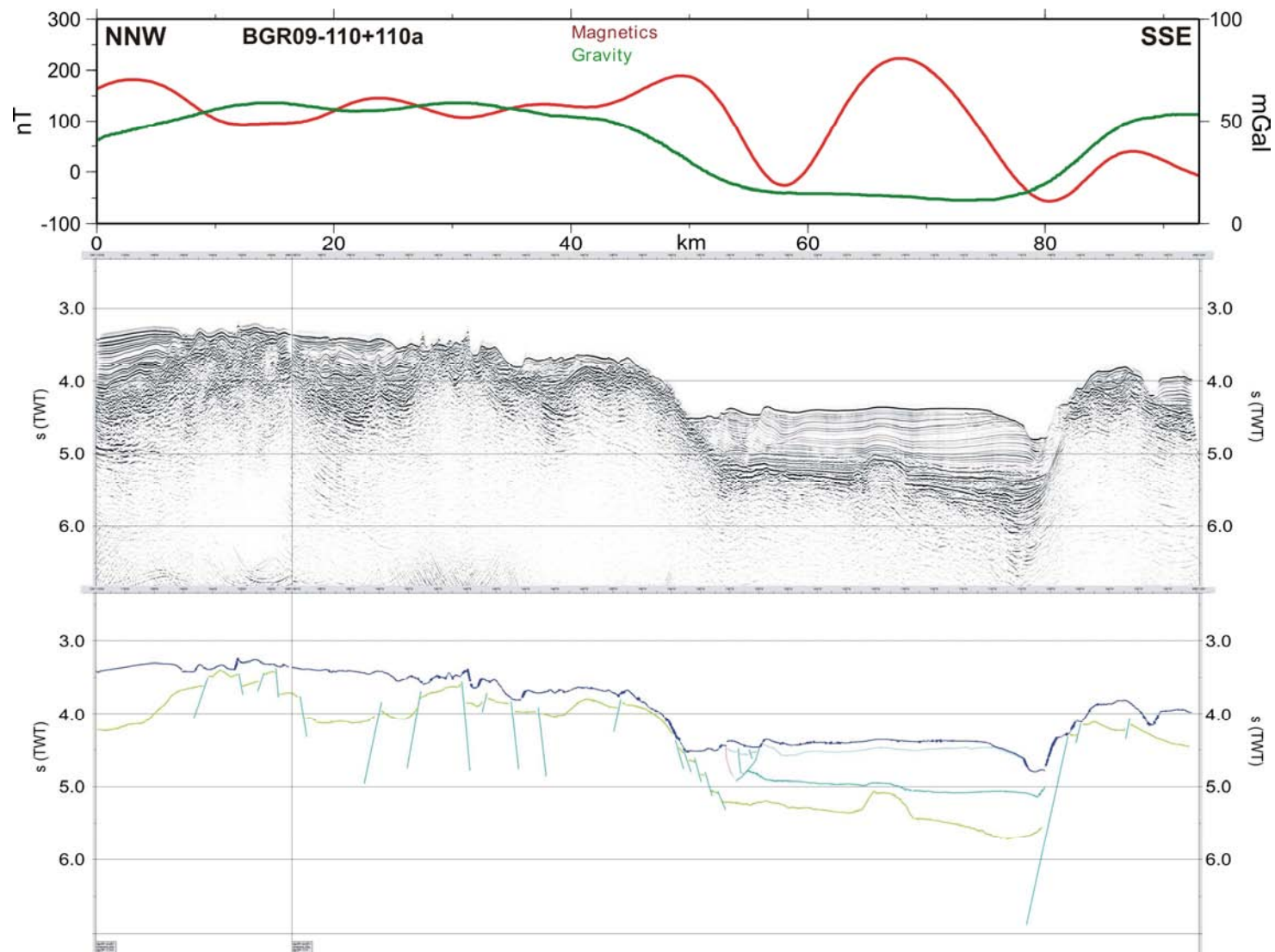


Fig. 1.18.10: Magnetic and gravimetric data, top. MSC profile BGR09-110 + 110a, CDP spacing 12.5 m, time section, middle. Interpretation of seismic data, bottom.

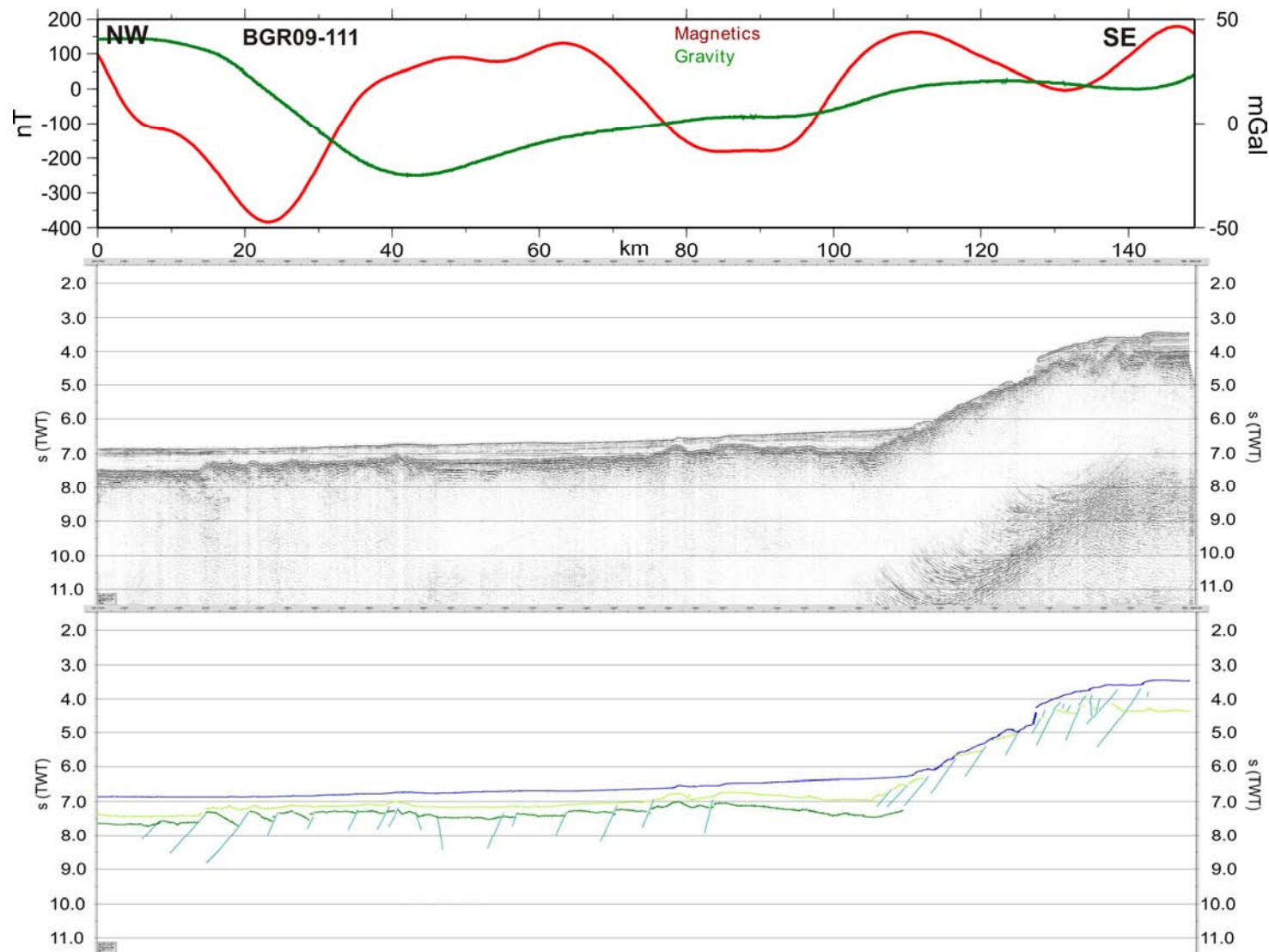


Fig. 1.18.11: Magnetic and gravimetric data, top. MSC profile BGR09-111, CDP spacing 12.5 m, time section, middle. Interpretation of seismic data, bottom.

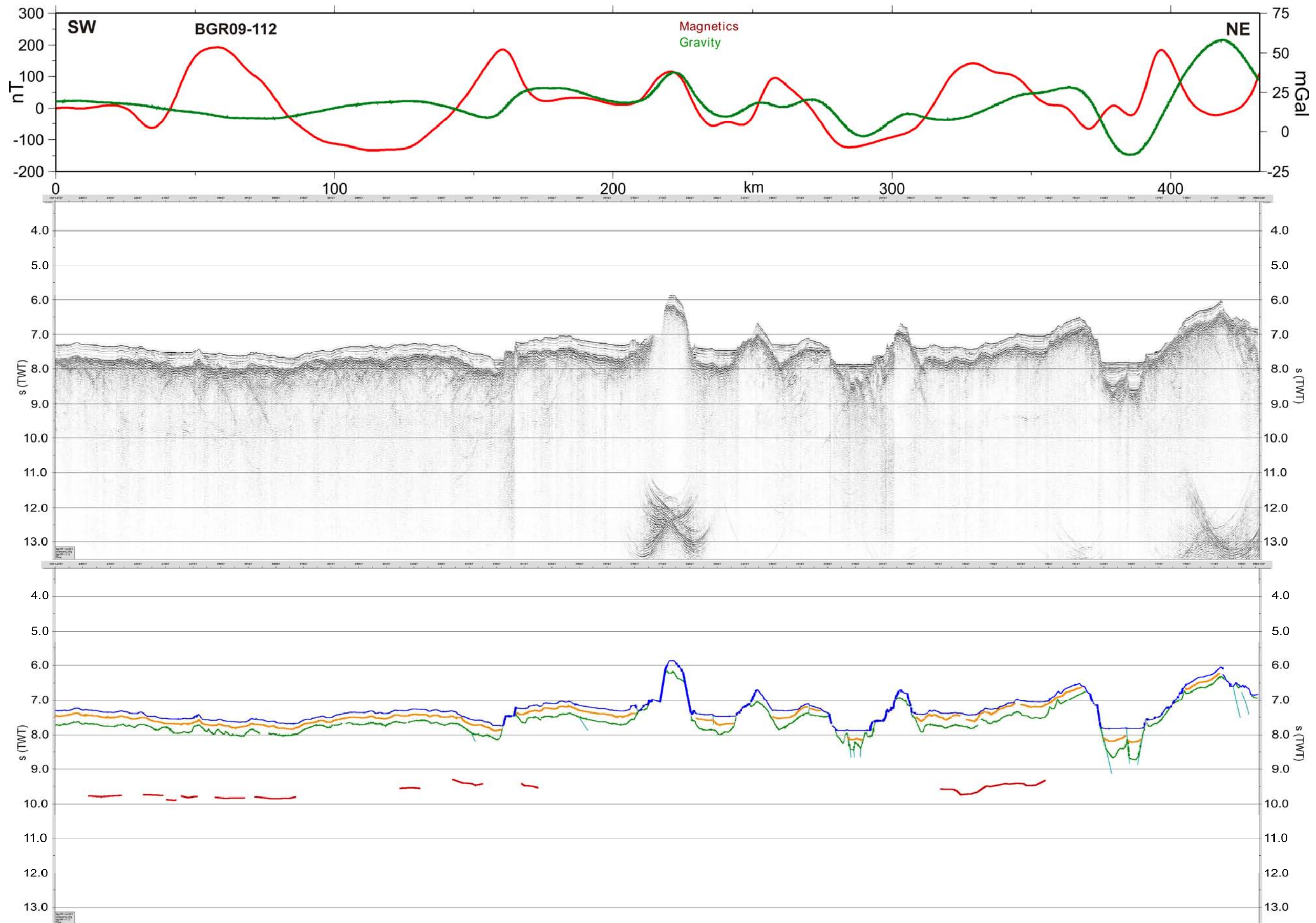
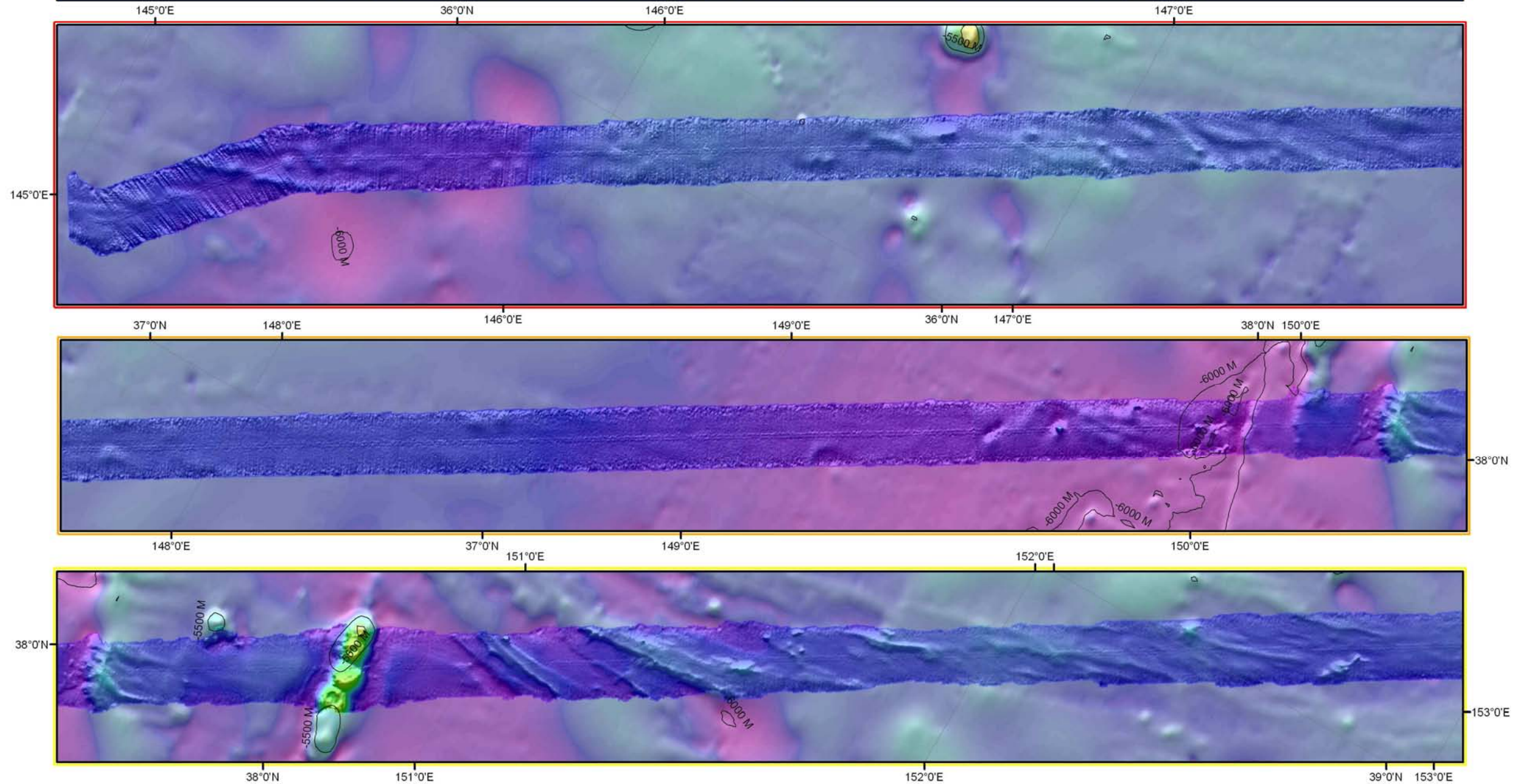
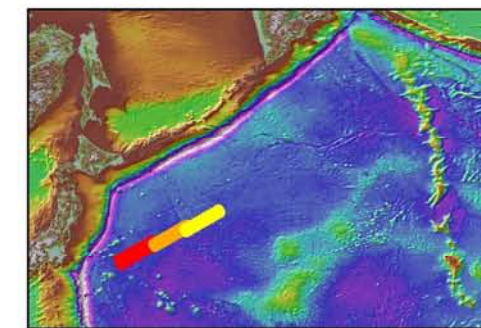
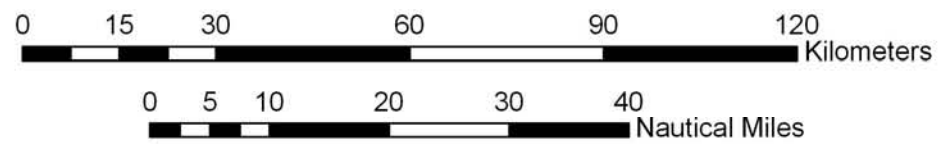
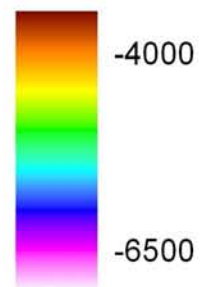


Fig. 1.18.12: Magnetic and gravimetric data, top. MSC profile BGR09-112, CDP spacing 12.5 m, time section, middle. Interpretation of seismic data, bottom.

Transit Yokohama - Emperor Seamount Chain Map Set 1



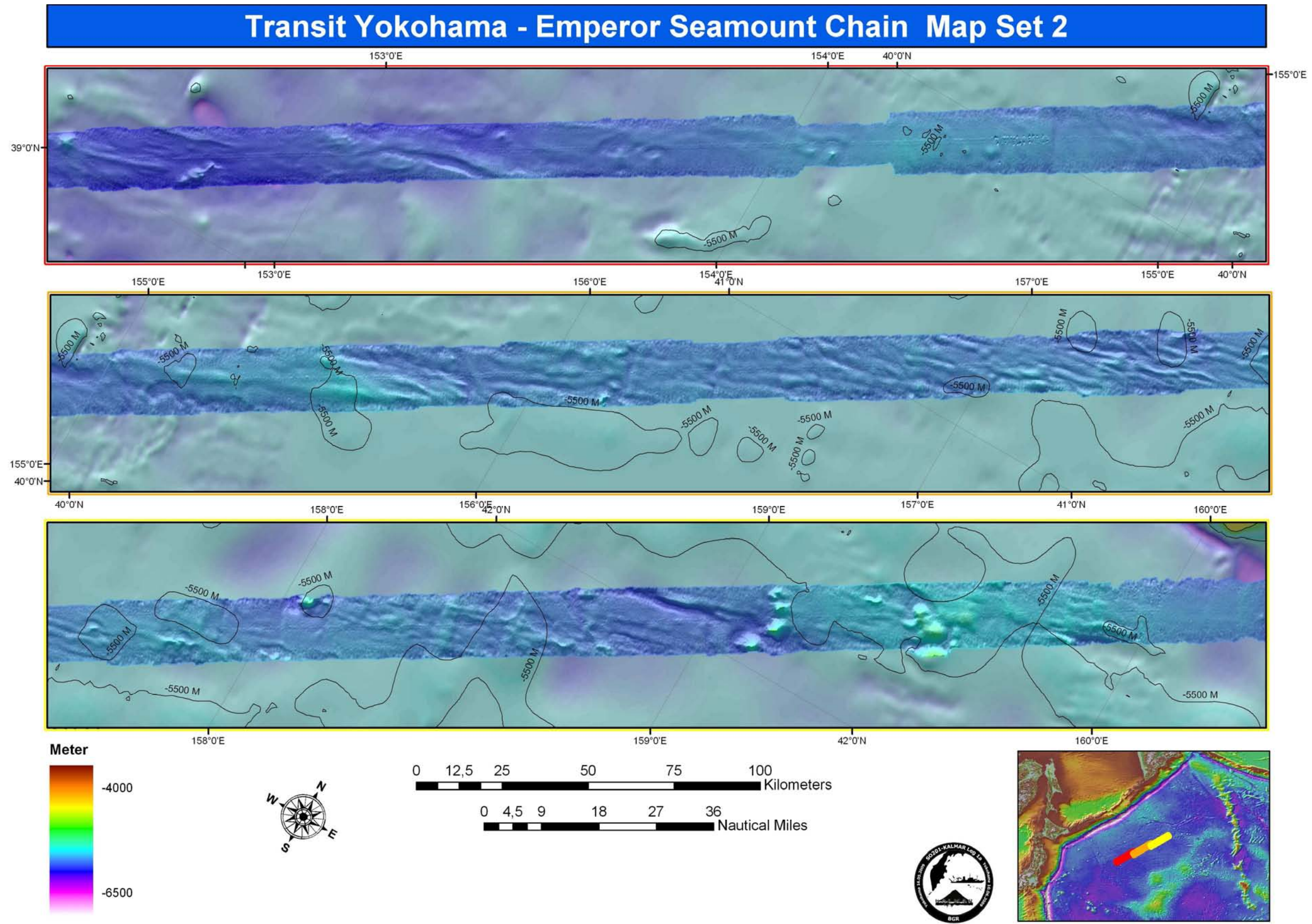
Meter



Background Bathymetry: SRTM30PLUS V5

BGR - STEFAN LADAGE - June 2009

Fig. 1.18.13: Transit Yokohama – Emperor Seamount Chain Map Set 1

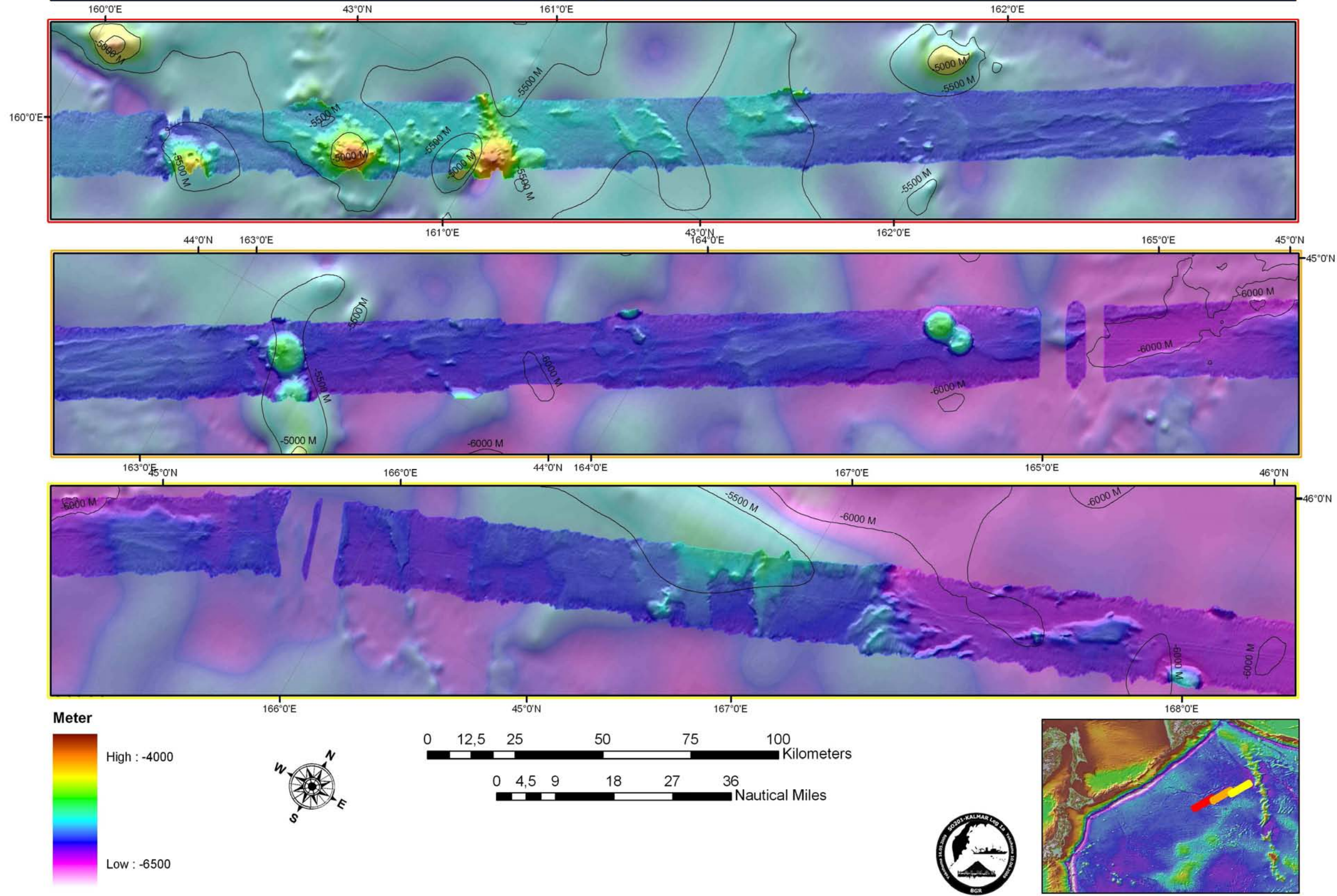


BGR - STEFAN LADAGE - June 2009

Background Bathymetry: SRTM30PLUS V5

Fig. 1.18.14: Transit Yokohama – Emperor Seamount Chain Map Set 2

Transit Yokohama - Emperor Seamount Chain Map Set 3



BGR - STEFAN LADAGE - June 2009

Fig. 1.18.15: Transit Yokohama – Emperor Seamount Chain Map Set 3

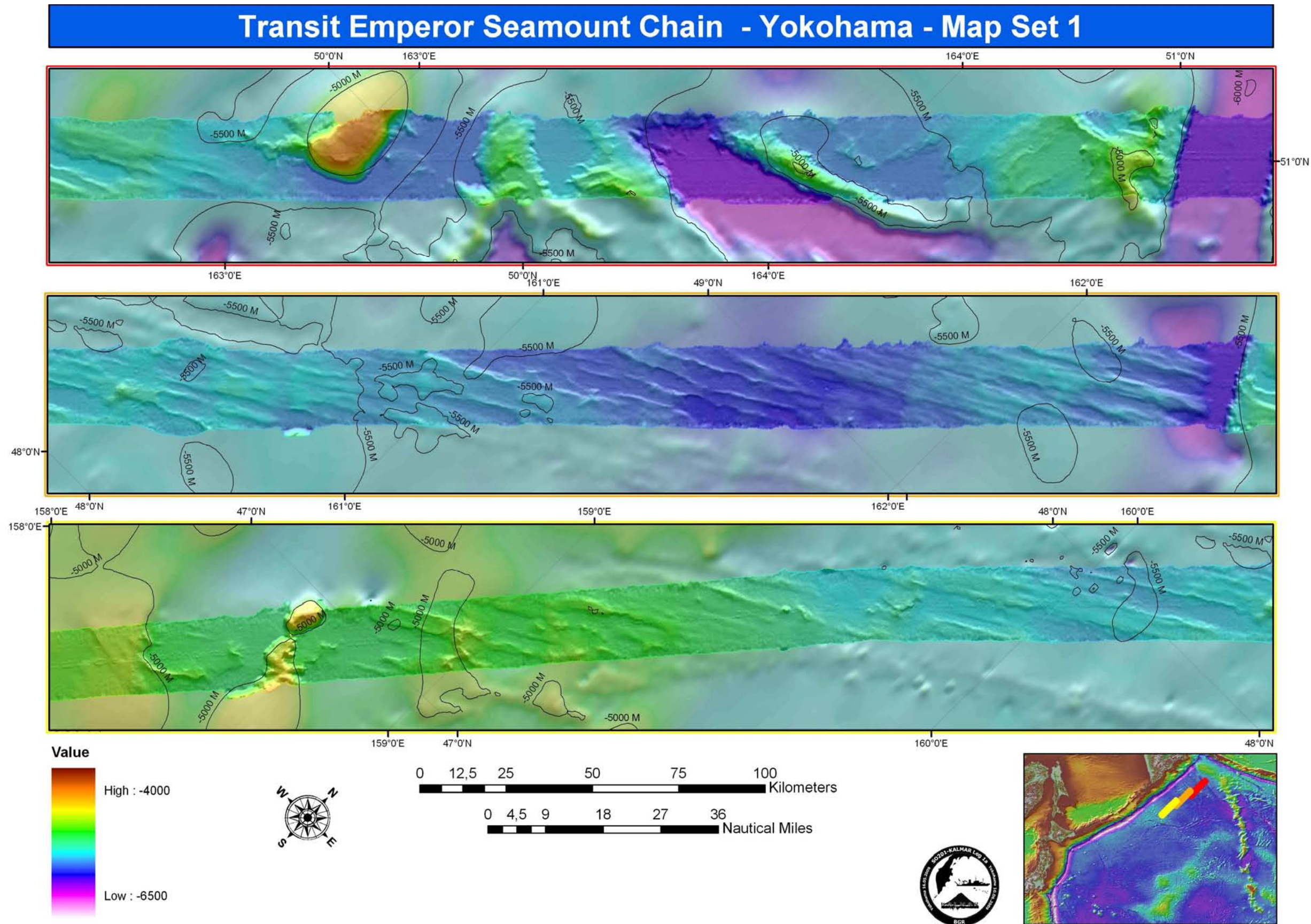
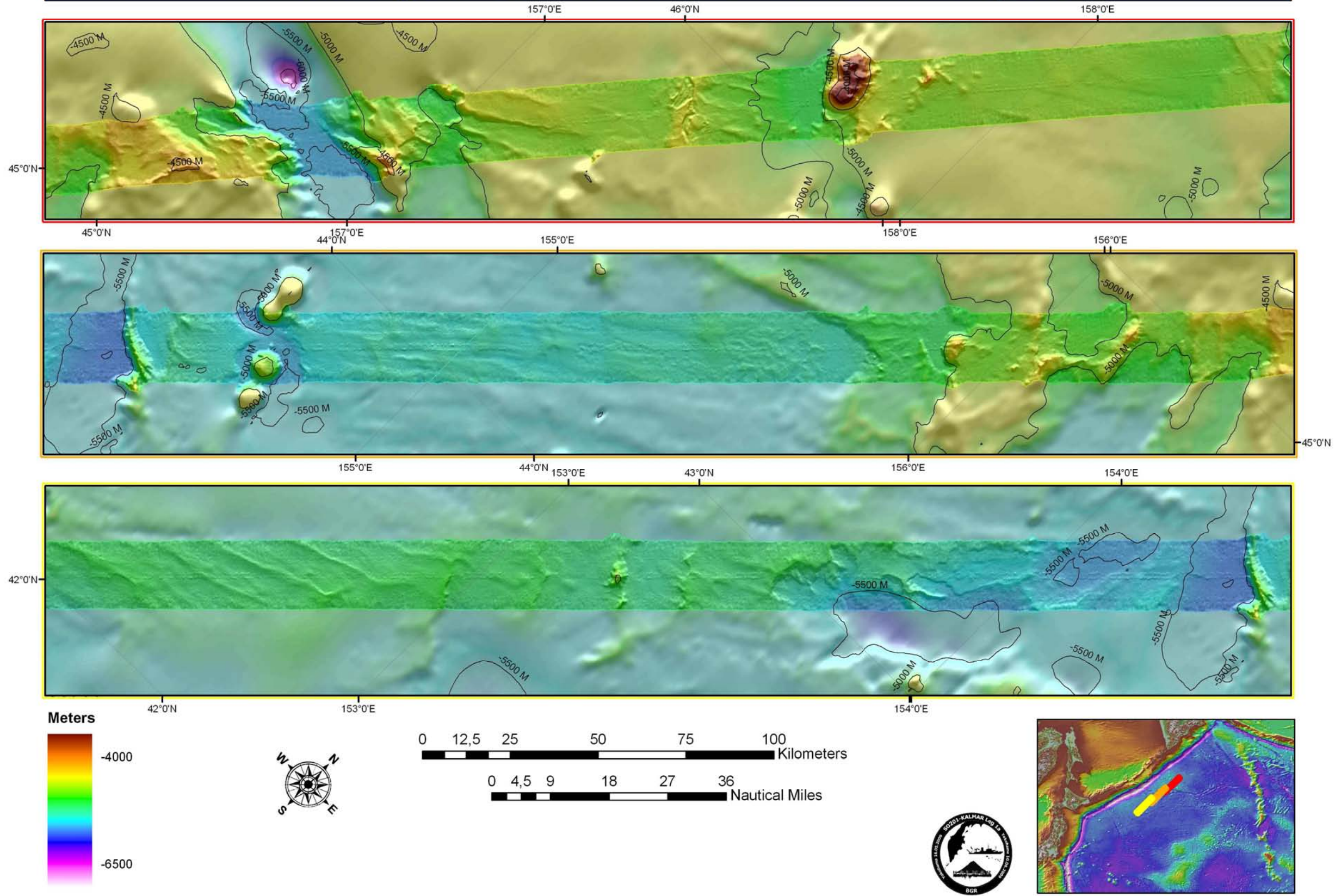


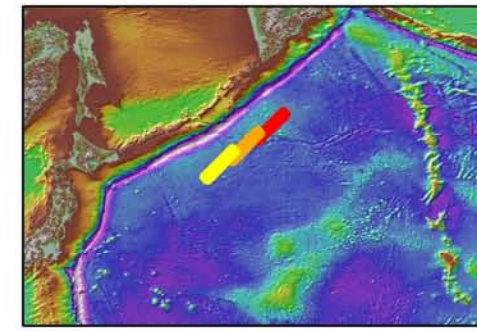
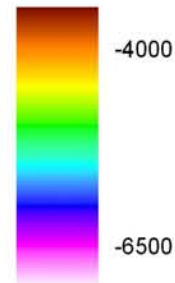
Fig. 1.18.16: Transit Emperor Seamount Chain – Yokohama Map Set 1

BGR - STEFAN LADAGE - June 2009

Transit Emperor Seamount Chain - Yokohama - Map Set 2



Meters



Background Bathymetry: SRTM30PLUS V5

BGR - STEFAN LADAGE - June 2009

Fig. 1.18.17: Transit Emperor Seamount Chain – Yokohama Map Set 2

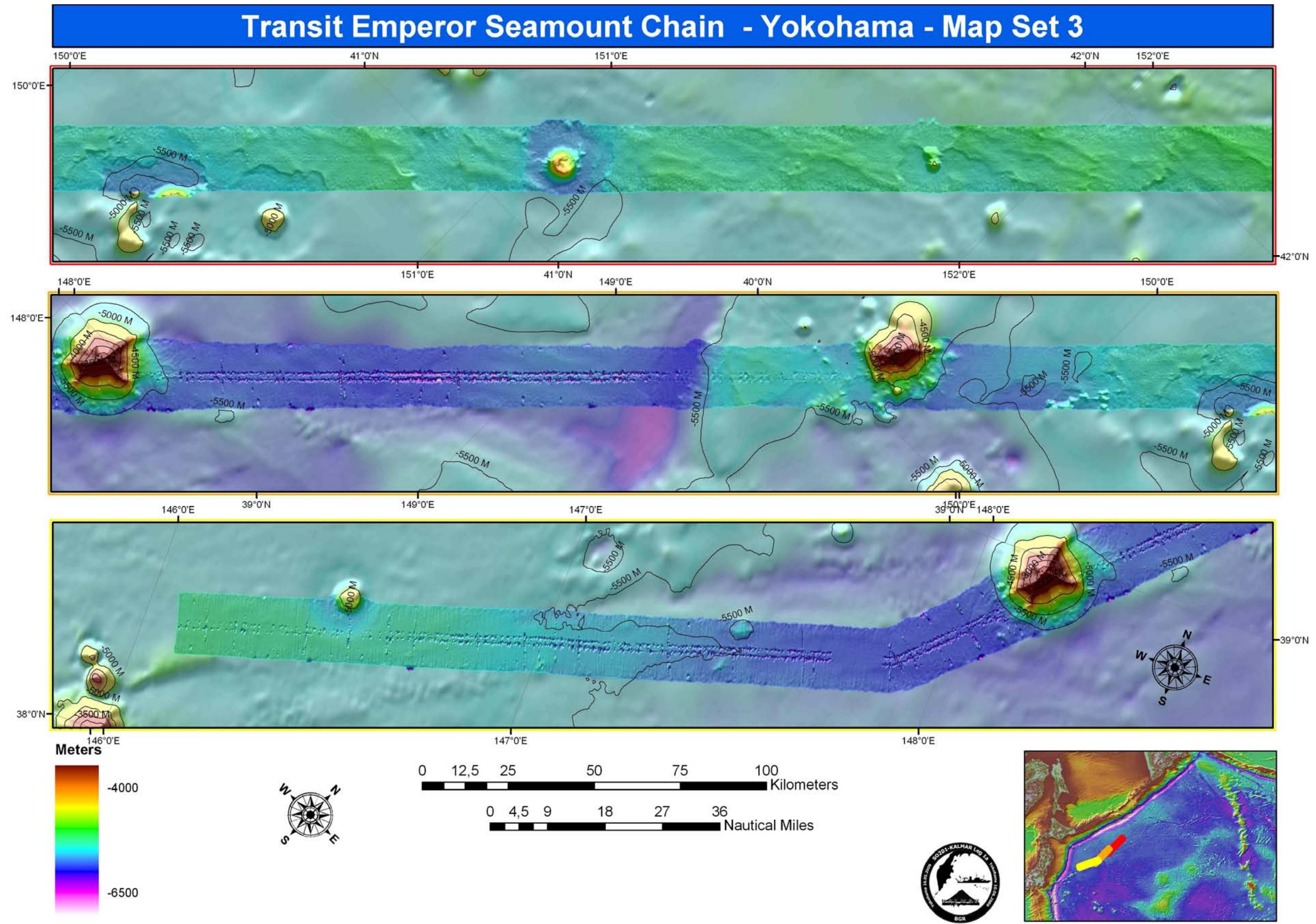


Fig. 1.18.18: Transit Emperor Seamount Chain – Yokohama Map Set 3